2016-03-01

Analysis of High Fidelity Turbomachinery CFD Using Proper Orthogonal Decomposition

Ronald Alex Spencer
Brigham Young University - Provo

BYU ScholarsArchive Citation

Spencer, Ronald Alex, "Analysis of High Fidelity Turbomachinery CFD Using Proper Orthogonal Decomposition" (2016). *All Theses and Dissertations*. 5846.
https://scholarsarchive.byu.edu/etd/5846

Analysis of High Fidelity Turbomachinery CFD Using Proper Orthogonal Decomposition

Ronald Alex Spencer

A thesis submitted to the faculty of
Brigham Young University
in partial fulfillment of the requirements for the degree of

Master of Science

Steven E. Gorrell, Chair
Matthew R. Jones
S. Andrew Ning

Department of Mechanical Engineering

Brigham Young University

March 2016

ABSTRACT

Analysis of High Fidelity Turbomachinery CFD Using Proper Orthogonal Decomposition

Ronald Alex Spencer
Department of Mechanical Engineering, BYU
Master of Science

Assessing the impact of inlet flow distortion in turbomachinery is desired early in the design cycle. This thesis introduces and validates the use of methods based on the Proper Orthogonal Decomposition (POD) to analyze clean and 1/rev static pressure distortion simulation results at design and near stall operating condition. The value of POD comes in its ability to efficiently extract both quantitative and qualitative information about dominant spatial flow structures as well as information about temporal fluctuations in flow properties. Observation of the modes allowed qualitative identification of shockwaves as well as quantification of their location and range of motion. Modal coefficients revealed the location of the passage shock at a given angular location. Distortion amplification and attenuation between rotors was also identified. A relationship was identified between how distortion manifests itself based on downstream conditions.

POD provides an efficient means for extracting the most meaningful information from large CFD simulation data. Static pressure and axial velocity were analyzed to explore the flow physics of 3 rotors of a compressor with a distorted inlet. Based on the results of the analysis of static pressure using the POD modes, it was concluded that there was a decreased range of motion in passage shock oscillation. Analysis of axial velocity POD modes revealed the presence of a separated region on the low pressure surface of the blade which was most dynamic in rotor 1. The thickness of this structure decreased in the near stall operating condition. The general conclusion is made that as the fan approaches stall the apparent effects of distortion are lessened which leads to less variation in the operating condition. This is due to the change in operating condition placing the fan at a different position on the speedline such that distortion effects are less pronounced. POD modes of entropy flux were used to identify three distinct levels of entropy flux in the blade row passage. The separated region was the region with the highest entropy due to the irreversibilities associated with separation.

Keywords: proper orthogonal decomposition, POD, inlet distortion, turbomachinery, reduced order analysis, computational fluid dynamics, post-processing

ACKNOWLEDGMENTS

I express my utmost appreciation to my advisor Dr. Steven E. Gorrell, for assisting and guiding me through this exciting research process. I am grateful for his guidance and insight in moving the research in the most productive direction, giving me the freedom to explore the unknown with my own ideas, and helping me not to flounder when I wasn't sure what to do next. I thank those on my committee, Dr. Matthew R. Jones, and Dr. S. Andrew Ning for their guidance and input through this research and writing process. I would like to recognize the research assistants in the BYU Turbomachinery Research Laboratory for their collaboration. I express gratitude to my wife for supporting my efforts throughout this process and offering valuable insight of her own into the research process.

I gratefully acknowledge the funding provided by the United States Air Force under Contract No. FA8650-12-M-2284 which made much of this research possible. I also thank Earl Duque from Intelligent Light for his partnership and feedback on this project.

TABLE OF CONTENTS

LIST OF TABLES

LIST OF FIGURES

NOMENCLATURE

$\mathbf{A}$	Linear transformation matrix of $\mathbf{D}$
$\mathbf{a}$	POD coefficient vector
CFD	Computational Fluid Dynamics
C_p	Specific heat
$\mathbf{D}$	Data matrix
DMD	Dynamic Mode Decomposition
LOR	Low Order Reconstruction
POD	Proper orthogonal decomposition
ROA	Reduced Order Analysis
ROC	Reduced Order Compression
ROM	Reduced Order Model
ROR	Reduced Order Reconstruction
$\mathbf{S}$	Similar matrix to $\mathbf{A}$
s_{flux}	Entropy flux
Δs	Change in absolute entropy
$\mathbf{U}$	$m \times m$ orthonormal matrix containing the spatial basis modes as columns
u	Axial velocity
$\mathbf{V}$	$n \times n$ orthonormal matrix of eigenvectors
$\mathbf{v}$	A given eigenvector of $\mathbf{D}$
λ	A given eigenvalue
μ	A given eigenvalue of $\mathbf{S}$
ϕ	POD mode
ρ	Density
Σ	Diagonal matrix containing singular values
θ	Angular position of a given blade row passage

CHAPTER 1. INTRODUCTION

Turbomachinery plays a key role in propulsion and power generation, and is playing an increasingly significant role in a diverse range of engineering applications. The expanding need for turbomachinery in diverse applications as well as the widening range of operating conditions required for turbomachinery in traditional applications have necessitated the ability to use high performance computing and advanced engineering software to evaluate the impact of possible design modifications and to assess whether a proposed system will meet design requirements. Such virtual prototyping allows analysts and designers to avoid time consuming and costly construction and testing of physical prototypes.

Traditionally, gas turbine turbomachinery design has relied on the approximation of clean inlet flow, which assumes that the properties of inlet flows are uniform over the area of the engine inlet, or Aerodynamic Interface Plane (AIP). Including non-uniformity in flow properties at the inlet of turbomachinery—referred to as inlet flow distortion—is an important and challenging problem. Since operating under such conditions is requisite for the engineered system to meet design requirements or desired performance goals, the use of high performance computing and advanced engineering software to perform high-fidelity simulations is critical to assess the impact of inlet flow distortion on compressor performance.

A significant challenge for analysis using the results of these simulations is the size of the datasets. The increase in computing power and development of high frequency experimental measurements generate massive data sets that strain the capacity of current systems to store, visualize, and analyze. Working with these data sets can be cumbersome for researchers because any extensive inquiry into flow characteristics may drastically increase the time required for thorough analysis. This applies to turbomachinery development where understanding and accounting for unsteady flows is critical to achieving gains in turbomachine efficiency and operating range. As an example of this size issue, the analysis for this research was performed on 660 million cell time-accurate Reynold's-Averaged Navier-Stokes simulations to observe the effect of inlet pressure distortion on the performance of a three-stage fan [1]. The distorted near-stall portion of the simulation required 33 hours of simulation time running on 1216 processors at the Navy Department of Defense Supercomputing Resource Center (DSRC). The resulting output required 89.91 GB of disk space to store just a single instantaneous time-step. Sifting through the data from these high-fidelity simulations is daunting and time-consuming. Indeed, time-accurate 3D simulations of this magnitude produce enormous amounts of data that may conceal rather than reveal the physics of interest. The size of these simulations makes the resulting datasets difficult to store and even more challenging to navigate within. Additionally, simply having high resolution solutions of complex flows does not necessarily make it straightforward to understand the governing physics or easily characterize flow features. Therefore, the primary post-processing goal of this research is to extract the most relevant and revealing flow information as quickly as possible and represent that information as consisely as possible.

Proper Orthogonal Decomposition (POD) provides such a solution by producing a reduced order description of the data, therefore enabling more efficient handling and examination of CFD output. POD extracted components contain quantitative and qualitative information about dominant flow features as well as general information such as regional pressure and temperature fluctuations. Data post-processing methods such as POD are becoming a necessary practice as numerical simulations become increasingly complex. For unsteady CFD data, the POD yields information on the variation of time and space. For this specific application where the result of 1/rev total pressure distortion is circumferentially varying stage performance, POD is a useful tool to visualize and quantify such variation.

The primary benefit of using POD is the time saved in analysis and post-processing. This is due to the reduction in storage requirement for the POD extracted components compared to the original dataset [2]. The savings in time and computational expense comes at the cost of some accuracy in the results, but the author believes the benefits outweigh this minimal cost in many situations. In the case of the analysis conducted in this research, the results were obtained from a small subset of POD extracted components, whereas traditional analysis could require processing a much larger portion of the data. A small portion of POD extracted components contains the majority of the information in the data, and thus analysis requires post-processing data a fraction of the size of the original. This is beneficial to the engineer navigating and considering a more compact description of the data. It is also a more efficient use of computer processor resources. The result is accurate information about the data with less time and computational expense.

Data post-processing tools such as POD help to maximize the potential understanding gained from each simulation by extracting patterns usually buried within the flow, not immediately visible to the naked eye. Working with these extracted components provides an alternative to working with the data directly. The two fold benefits of this are a much more compact representation of the same information, and a separation of flow structures and drivers of unsteadiness in an organized way.

This thesis presents and describes analytical methods based on POD and how they may be used to analyze a turbomachinery flow field operating with inlet flow distortion. POD is a relatively new tool in the analysis of turbomachinery, and this work represents the first published results applying POD to the analysis of distortion through a multistage fan. In this analysis, methods for identifying specific flow features and their dynamics are demonstrated. This is significant because in many turbomachinery flows some flow features are difficult to identify because of the presence of so many other phenomona. For example, shock wave behavior can be difficult to identify in the presence of blade row interactions. It is also shown that POD components are able to extract both quantitative and qualitative attributes of these flow features. This is significant because POD makes both the qualitative and quantitative information available very efficiently without the complex analysis which can be required with traditional techniques. POD is used to explore a range of different flow properties at two operating conditions. Additional insight is obtained by comparing POD results from simulation data based on distorted and clean inlet conditions. In addition to this information, insight is gained into the flow physics of this fan based on the behaviors identified with POD. This information is used to draw new conclusions about the effect of distorted flows on the operating condition of the fan as well as the converse, the effect operating condition has on the distorted inlet condition as it travels through the fan.

The outline of this thesis is as follows. Chapter 2 contains background information on POD and inlet distortion. A literature review then follows illustrating how POD has been used up to this point in the analysis of fluid flow datasets. A literature review on the study of inlet distortion is also presented. Chapter 3 presents the POD methodology for analysis. This chapter includes the details of data extraction, POD calculations done on this data specifically, and the techniques used for analysis. Chapter 4 contains the resulting analysis on the data described for a variety of flow parameters, two operating conditions, with comparisons to the clean operating condition. Distortion transfer through the fan is analyzed as well as generation within the fan. Chapter 5 presents the conclusions of the research.

CHAPTER 2. BACKGROUND AND LITERATURE REVIEW

2.1 Proper Orthogonal Decomposition Basics

From a mathematical perspective, POD produces a set of basis modes which can be used to represent the dataset as a linear combination these modes. The term *basis* is used in linear algebra to describe the set of vectors used to span a given subspace. Proper orthogonal basis modes form a basis for the subspace spanned by the data for which the POD is calculated. These basis modes are constrained to be orthonormal (meaning they are orthogonal to each other and their magnitude is unity) and are ranked based on the magnitude of the projection of the dataset onto them. Basis modes characterize the most fundamental aspects of the data while their associated coefficients determine the contribution of each basis function to the data at a given instant. Analysis of these more basic components can give useful insight into how the data varies in a given dimension. For unsteady CFD data, POD is capable of yielding information on how the data varies with time and space.

The discrete POD, which is used in all of the examples in this study, operates on a data matrix **D** to generate the basis functions, called basis vectors in the discrete case, and their associated coefficients. Basis vectors are traditionally called (and will be referred to hereafter as) modes. This representation of **D** is given in Eqn. (2.1). It should be made clear that x and y in this equation are general variables and not spatial variables. The basic equations are shown in this overview. More details regarding the mathematics, as well as helpful examples can be found in [3,4]. When the POD is computed, singular values corresponding to each of the modes are also output. The singular values indicate the relative significance of each mode in its representation of the dataset.

$$\mathbf{D}(\mathbf{x},\mathbf{y}) = \sum_i a_i(y)\phi_i(x) \tag{2.1}$$

The bulk of the computational effort required when implementing POD is associated with the calculation of the modes. Once the modes are obtained the acquisition of the associated coefficients is a straightforward calculation of the projection of the data onto each mode. For discrete data the modes are represented as vectors so the projection is simply the scalar product of a vector of data and the mode. Since the modes are orthonormal, they are linearly independent and each projection represents a unique contribution to the overall solution. A useful property of the orthonormal basis is that its inverse is just its transpose. Thus the equation for the calculation of the coefficients is shown in Eqn. (2.2).

$$\mathbf{A} = \phi^T \mathbf{D} \tag{2.2}$$

In the calculation of the POD, it is possible to remove mean flow information prior to analysis using POD. In this situation the mean must either be subtracted from the columnspace of **D** or the rowspace of **D**. An additional form of mean subtraction may be performed by subtracting the mean of the entirety of the matrix **D** from itself. All of these methods change the POD output in the sense that when the mean of a given dimension is removed, the POD output that previously contained that information is removed and other information is shifted to that particular output. A variety of mean subtraction methods were tried for this thesis research. However, it was found that subtracting the mean for a given dimension (like the rowspace for example) introduced unrealistic spread into the other dimension (in this case the column space). This made it difficult to correctly interpret the results. For this reason, mean subtraction was not performed on the data prior to POD. It was then understood that mode 1 would contain the mean information for the data, and the results were interpreted in this context.

2.2 Applications of POD

Data post-processing applications using POD can be categorized into three distinct areas: reduced order compression and reconstruction (ROC/ROR), reduced order analysis (ROA), and reduced order modeling (ROM). Examples of ROC/ROR, ROA, and ROM can be found in [2,4,5] and are briefly explained below. The purpose of this description of various methods for post-processing is to illustrate the variety of applications for which POD is well suited and show that

ROA is just a small subset of the capabilities of POD. It should be made clear that the primary focus of this research is developing methods to use POD as a tool for analysis (ROA).

Blanc [4] covers thoroughly the process of data compression using POD as well as a variety of aspects of reduced order modeling. In a ROC a selection of the highest order basis modes, as well as their associated coefficients, is saved to represent the data, with the remaining modes, as well as the original data being discarded. The preserved modes are those associated with the highest singular values. Since the contribution of each mode to the data is unique, and the modes are optimized to capture the most variation possible with the orthogonal constraint mentioned above, using the first modes represents the best possible solution in terms of accuracy for a given order representation. Chattergee [3] describes this as being an optimal rank approximation, meaning that no other matrix of the same rank can be closer to $\mathbf{D}$ in the Frobenius norm. In other words, using only the first mode yields the best possible first order approximation to the data. Using the first and second yields the best possible second order approximation, etc. With this in mind, storing a limited number of modes and coefficients requires significantly less disk space. Blanc explores several ways of most efficiently doing this and reports compression ratios on the order of roughly 10 using POD alone and up to 574 by combining POD with the JPEG compression algorithm [4]. These compression ratios were reported on turbomachinery data investigating the effect of blade row interactions. This example shows the usefulness of POD in preserving the accuracy of large datasets in the most efficient way possible.

The data saved in a ROC is used in the reduced order reconstruction where an approximation to the original data is reproduced using a selection of low order modes. In a ROR, the most obvious variation is included in the reconstruction because that is the information retained by lower order modes. The more subtle perturbations in the data captured by less significant modes are discarded. The amount of variation in the data included in the reconstruction can be quantified using “percent energy”. Percent energy is calculated using the singular values. High values of percent energy implies a high order reconstruction of the data. The details of the computation of percent energy may be found in chapter 3.

ROMs can also be created using sets of simulations where the grid stays the same but the input parameters are varied. In this situation, the POD modes and expansion coefficients are coupled with interpolating functions to produce the ROM. The ROM then enables the prediction of

CFD solutions for input parameters within the range of those used to produce the solution database. A ROM then, still requires the same input parameters as a traditional CFD simulation but uses a reduced mathematical formulation to generate the solution. Examples of this technique are found in [4, 5] where ROMs are used to model conjugate heat transfer over a circular cylinder and a turbine blade, and the flow over an airfoil. In the case of the heat transfer over a cylinder, the ROM was able to predict temperature to within 0.11 deg K. For the case of the turbine blade the maximum error was roughly 20 deg K. Though the error was larger, the ROM provided meaningful information. For the case of the airfoil, various ROMs were selected based on the number of POD modes used to create the model. Percent energy values ranged from 80% to 99.9%. The ROMs were compared and an ideal number of POD modes was presented to best model the data. It was shown that after a certain point, adding modes did nothing to increase the accuracy of the ROM. These studies point out the strengths and weaknesses of ROMs and the ideal conditions for the best results. The main conclusion is that ROMs are extremely useful when a variety of conditions are investigated with the intent of identifying the best set of parameters for a desired result. In this case, ROMs can reduce the computational expense by eliminating the need for many CFD simulations.

2.3 POD as a Method For Reduced Order Analysis

ROA utilizes POD modes and coefficients as a tool to gain insight and understanding about the dataset. In this sense a POD dataset can be defined as the output of POD modes and coefficients from a given dataset. In the context of CFD data, POD ROA can be utilized to extract quantitative and qualitative information about dominant flow features such as shockwaves, boundary layers, and wakes. ROA can also be used to extract general information such as regional pressure and temperature fluctuations.

POD decomposes a data matrix into a set of modes and expansion coefficients with specific information being carried by each one. POD allows control over which flow variables are carried by the coefficients and which variables are carried by the modes. This is extremely valuable because it allows for isolation of phenomenon based solely on a particular dimension such as time. The POD analyses presented in this thesis were calculated such that the modes carried information on the spatial variation, and the coefficients carried the information on variation of the data with time. This is most often the case for ROA, however, it is not a requirement to segregate the flow dimensions in this way. It is possible to have coefficients carry information on an additional spatial dimension instead of time.

Pobitzer et al. describe ROA techniques, especially POD, as energy-scale aware feature extraction techniques [6]. These techniques work through the "removal of unimportant details enhancing the complexity of visualizations". The authors advocate this method as ideal for studying turbulence because POD naturally sorts structures based on their energy content. Turbulent flows are formed by different scales of motion and POD provides the ability to identify and describe the scales carrying significant amounts of energy. This ability is important since it is desirable to understand, predict, and control turbulence. They describe their approach as "an energy scale aware extraction of features, by first breaking the field into its energy-components and then applying conventional feature extraction methods." This then allows the researcher to preserve important structures within the flow field, and remove unnecessary details. Thus the simplified flow field produced by a low order reconstruction of the data focuses the output of the feature detection software. The features extracted are then associated with the dynamically most important scales of motion. They warn however, that POD operates in L^2 which is the inner product space of the modes and the dataset, so there is no guaranteed bound for the local error. This means that POD modes will be the most accurate for the dataset as a whole, not necessarily for a local region. In other words, a given mode might contain regions where the reconstruction error is high, even though for the mode as a whole the error is low. There is no way to control the local error.

Roussinova et al. [7] use PIV data from a smooth open-channel flow and investigate the fluid structures using POD. The POD modes were used to identify vortical structures. Their analysis then proceeded to use several reduced order reconstructions to analyze the data. They reconstructed the flow using only the first 12 modes to expose the most energetic structures. The first 12 modes were reported to have captured 50% of the turbulent kinetic energy of the flow. They then reconstructed the flow using the higher order modes to identify the low energy structures. Modes 13-100 captured 33% of the turbulent kinetic energy. The reconstruction using the higher order modes (13-100) is shown in Fig. 2.1. Five vortical structures are identified in this figure. The authors believe that these structures are cross sections of hairpin vortices of various sizes and strengths. The authors also used the modes to identify eddy behavior such as elongation and in-

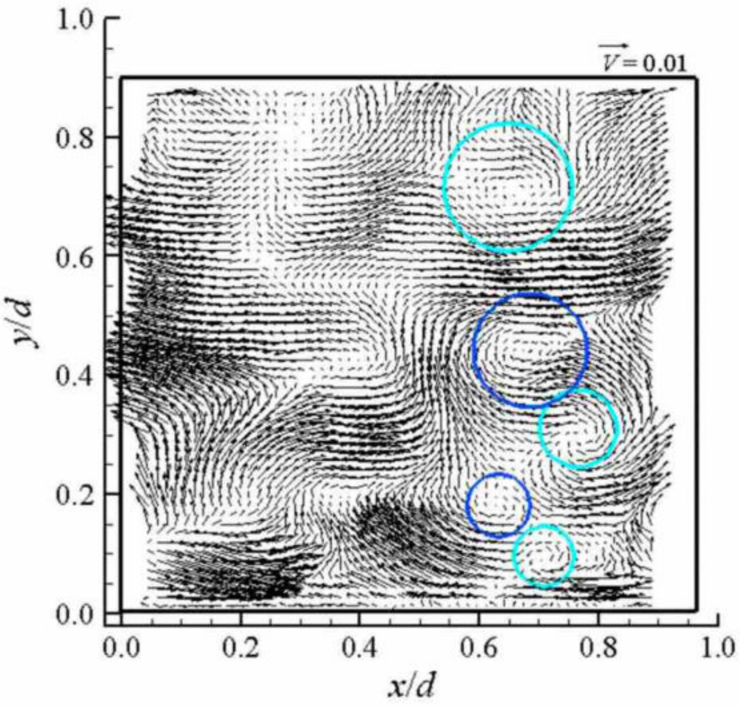

Figure 2.1: Examples of hairpin vortex cross-sections identified using POD modes taken from [7]. Velocity reported in (m/s).

clination. These are good examples of general feature identification using POD modes as well as which features contain or contribute to the most turbulent kinetic energy.

Shim et al. [8] study the development of the structural characteristics of a plane jet. The POD was applied to the 2-D PIV data for this flow. As in [7] the lower order modes were used to identify large scale vortical structures. In the analysis, the basic mean and turbulent flow field were analyzed to get a general characterization of the flow. POD analysis was then directed at the structures identified to characterize their evolution and development. It was found that the counter rotating vortices contained in the flow could be reconstructed using only two modes. Examples of these reconstructions at various time steps are included in Fig. 2.2. They can be used to identify counter-rotating vortices. Conclusions were also made about the displacement of the vortical structures.

Feng et al. [9] look at vortex shedding off of a circular cylinder. The vortex shedding is controlled by a jet at the back stagnation point. This study performs the POD on experimental PIV data. The authors identify dominant structures present in the first two POD modes at different

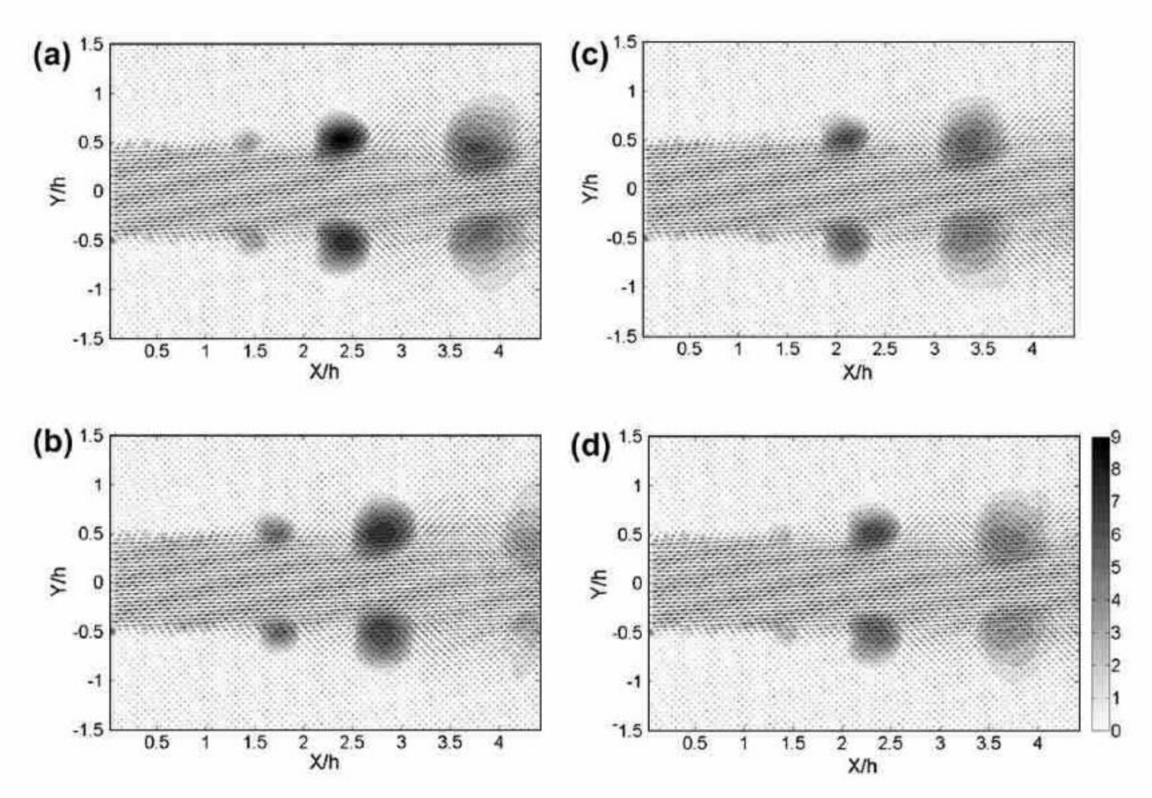

Figure 2.2: Reconstructed velocity vector fields using the 2nd and 3rd modes at various time steps taken from [8]. These reconstructions identify counter-rotating vortices.

experimental conditions. They identify an arrow-head like structure symmetric about the centerline in one mode and antisymmetric in another mode. They attribute this feature to characterize the vortex shedding of the flow. This is an example of the ability of POD to correlate a given mode to a certain flow phenomenon.

Grieg et al. [10] investigated the physics of flow over a corrugated waveform. They used POD as one tool to identify dominant flow structures such as turbulence production and transport. They compared the POD modes for heated and unheated flows over the corrugated waveform and identified where flow features were shifted to higher and lower energy modes due to the heating. They concluded that at high flow rates the differences in the modes due to heating was smaller than at low flow rates. Thus the effects of heating were shifted to higher order modes in high flow rates. This illustrates the ability of POD to identify causal relationships between various flow features.

In a more recent study, Charalampous and Hardalupas [11] used POD to analyze the development of a round liquid jet immersed in a coaxial flow. The two fluids were immiscible and

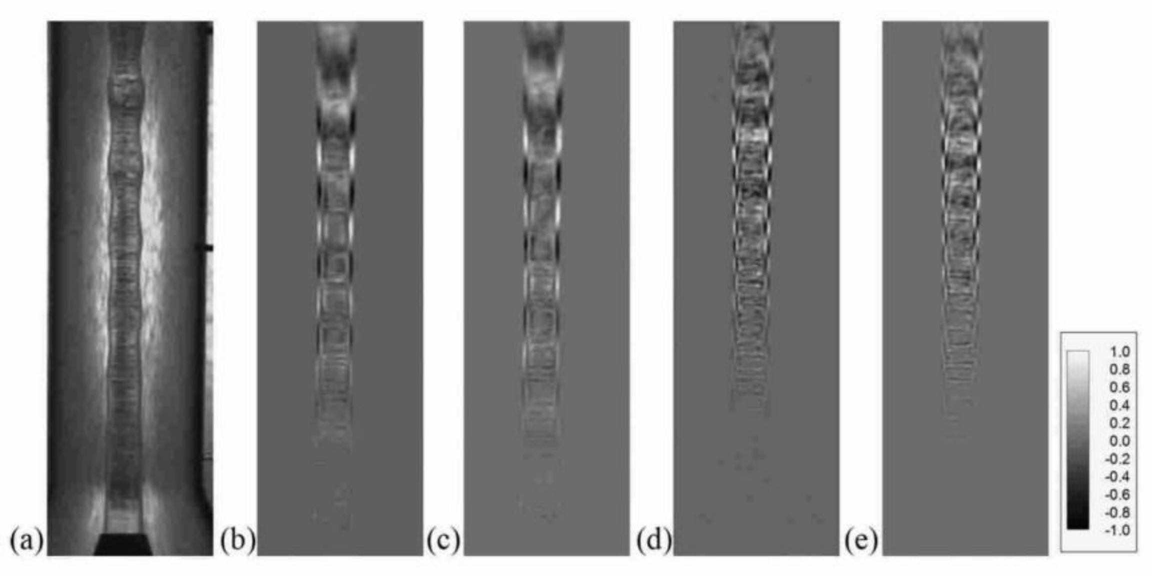

Figure 2.3: Image sample of central jet (a) and first four modes (d-e) taken from [8]. These modes identify varicose dilation which propagates along the jet length.

of similar densities. The authors investigated the vicinity of the nozzle exit for two flow regimes. They used POD modes to analyze and characterize the development of the jet. They were able to reduce the description of jet morphology to a small number of spatial modes. These modes isolated the most significant aspects of the jet development. The modes analyzed are shown in Fig. 2.3. They also utilized a fourier transform of the temporal coefficients in order to isolate the frequencies present in the captured flow feature. They used this technique to isolate a traveling sine wave in the flow and identified a frequency of 235 Hz. The authors contended that the basic morphological structures identified would be unobtainable using conventional image analysis. They explored the amplification and attenuation of this sine wave and also contended that in some situations the amplitude of the traveling sine wave was attenuated to the point that it was only observable using POD. Thus another benefit of POD is the ability to track features that grow and shrink in size and may be difficult to discern at small scales

Another recent study is the work of Zhaung and Hung [12]. They explored and presented methods for reduced order analysis using the quadruple proper orthogonal decomposition. The setting for their analysis was the swirl field induced at the cylinder intake for an internal combustion engine. They used the quadruple POD to analyze the dominant flow structures in the velocity field. The quadruple POD separates flow features into dominant and fluctuating structures by dividing them into four categories: dominant structure, coherent structure, turbulent structure, and noise structure. After the traditional POD is calculated the modes are classified into these categories based on a calculated relevance index. The authors contended the usefulness of this technique due to the fact that two adjacent modes might be quite similar. The authors concluded that varying the intake swirl ratio primarily effected the dominant flow structure and not the turbulent structure. This technique illustrates how POD may be used to analyze and quickly determine the primary effect of changing parameters in CFD or experimental data. This technique is fairly new (2016) and shows a promising direction for future research.

Ruscher et al. [13] show a method for how the snapshot POD from a series of timesteps can be used on a varying grid. Traditionally POD is usually used on snapshots of grids that stay consistent, meaning that the spatial location of each gridpoint and the number of gridpoints is the same for each snapshot. The repeating geometry method discussed later is one method for varying the grid but the local geometry stays the same. Ruscher et al. discuss more variation in the grid than the repeating geometry method.

Another valid point for consideration when performing ROA is made by Mulleners and Raffel in their study of the onset of dynamic stall [14] on a helicopter blade. In this study they establish a strong association of the third POD mode with the dynamic stall vortex and make a claim that the evolution of the coefficients for this mode determine the onset of stall. However, they make the point that POD modes are nothing more or less than mathematical constructions, and as such they need to be interpreted appropriately. They say:“associating them with coherent flow structures should not be done without proper consideration”. They used POD in their research as only one component of a more comprehensive analysis. In their case conclusions were made when the behavior indicated by POD was congruent with other analysis performed. This study is a good example of the need for cross-validation of the behaviors suggested by the POD modes.

POD is also sometimes referred to as principle component analysis because a set of correlated data is converted to a set of linearly uncorrelated (orthogonal) variables called principle components [15]. These principle components account for the variation in the data, and are ranked according to the amount of variation they capture. POD then works by extracting the most relevant flow information, or principle components, which represent the data in the most concise way possible.

POD has been used for a variety of fluid flow application as shown above, however the use of POD as a tool for analysis in turbomachinery applications has been comparatively minimal. POD as a tool for reduced order modelling of turbomachinery has a good foundation in the literature. Brenner et al. [16] use POD as a tool for creating a reduced order model to predict turbomachinery flows for a range of input parameters. However, this is a different application than using POD as a tool for analysis. Additional research has also been performed using POD as a tool to develop reduced order model for turbomachinery found in [17, 18]. Blanc, performs an insightful examination of the qualitative aspects of POD analysis of distorted flow [2, 4]. He analyzed the effect of a distorted total pressure inlet condition on static pressure in the third rotor row of a fan. Blanc also validated the method of repeating geometry as a method for analyzing the time variation of turbomachinery data by instead analyzing data around the circumference. It was found that the circumferential variation at a single time step varied in the same way a single blade passage did with time. This makes a temporal analysis much more straightforward. Blanc also explored curvefitting the POD modal coefficients with low frequency sine curves in order to filter out high frequency noise. The simulation data used by Blanc is the same as used in this research. One aim of this research is to expand the work of Blanc by focusing on the quantitative information in a distorted flow which can be extracted using POD. The research performed in this thesis is unique in the sense that it is some of the first applying POD analysis techniques to turbomachinery flows.

POD has some similarity to the harmonic balance method for solving unsteady flows [19, 20], but it is in fact very different in application. In turbomachinery flows, the harmonic balance utilizes fundamental frequencies like blade passing or flutter vibration frequencies to fit the unsteady flow to a Fourier series instead of marching through time. This has been shown to be very effective for a variety of applications dominated by periodic fluctuations [21]. POD, however, is not necessarily biased toward any frequency from the start because the modes are derived from optimizing the projection onto the original data set. If there are highly periodic elements of the unsteady simulation, POD will extract those features as well. The benefit here is that we are not limited by a single fundamental frequency and its harmonics. Because of the complexity of this simulation (seven blade rows, pressure distortion, etc.), there are a variety of dominant frequencies, depending on the POD mode being observed. Just as the pressure distortion effect is isolated from this time-marching simulation, it can also be neglected to focus on the remaining dominant frequencies of variation. The harmonic balance method is also primarily a technique for solving turbomachinery flows. In the applications shown in this thesis, POD is used only as a technique for analyzing existing data.

2.4 Alternative Methods for Reduced Order Analysis: Dynamic Mode Decomposition

Dynamic Mode Decomposition (DMD) is similar to POD in that it is a matrix decomposition technique which extracts modes describing the dynamic behavior of the flow and the drivers of unsteadiness. The primary difference between the two methods lies in the matrix which is decomposed. In the case of POD, the data matrix itself is decomposed, where with DMD a linear transformation matrix describing the dynamics of the data is decomposed. The resulting modes then extract similar dominant features but each with a different focus. POD are modes spatially orthogonal whereas each DMD mode isolates a distinct and single oscillation frequency. Thus the features contained in the respective modes will be sorted based on each methods associated criteria.

Schmid is a prominent author on DMD and has written several papers on the mathematics of the technique [22] as well as on practical methods for how to use DMD in ROA [23]. He describes a primary difference between the two methods: “When compared with proper orthogonal decomposition, we can state that POD modes enforce spatial orthogonality (decorrelated structures) while keeping multiple frequencies in the evolution of each individual POD mode, whereas DMD modes are temporally orthogonal (pure frequencies) but show, in general, spatial non-orthogonality”. He leaves it up to the reader to decide what aspect is of more value in an analysis: separating features by frequency or energy ranking. He does give his opinion on the matter: “For experimental data from a saturated nonlinear process, the extraction of pertinent frequency information and its associated structures may be more critical than an energy ranking of spatially decorrelated structures.” He also makes the point that contrary to proper orthogonal decomposition, the DMD not only contains information about coherent structures but also about their temporal evolution.

Tu et al. also have written a paper on the theory and applications of DMD [24]. He comments that “DMD has quickly gained popularity in the fluids community, primarily because it provides information about the dynamics of a flow, and is applicable even when those dynamics are nonlinear". POD can also be applied to non-linear problems. He comments that the modes extracted by DMD are similar to POD but the corresponding eigenvalues for DMD define growth/decay rates and oscillation frequencies for each mode, rather than an energy ranking provided by POD. He states the primary difference between the two methods as being that POD optimally reconstructs a dataset with the modes ranked in terms of energy content while the DMD sorts the modes by frequency.

Two good examples of DMD used as a method for ROA can be found in [25, 26]. Reference [25] is concerned with the study of unsteady behavior in shockwave turbulent boundary layer interaction. Reference [26] studies dynamic stall in the flowfield around a pitching airfoil. These sources leverage the analysis technique of looking at the dominance of a mode at a particular spatial location. Grilli et al. conclude that for sufficiently long sequences DMD is linked to a single temporal frequency. This is useful because POD does not yield direct information concerning the frequency of detected modes. They also show that DMD is well suited for analysis of low-frequency unsteadiness.

The authors of the following sources [22, 27, 28] make several claims regarding the advantages of DMD, and that in some situations may provide superior insight to that obtainable through traditional methods using POD. These claims fall into three categories. First, DMD provides additional information not provided by POD. Second, DMD describes the same information as POD in a different or more useful way. In this situation, the information provided by POD may not be misleading or incorrect, only that a different description may be more useful or shed new light on the data. Finally, the literature makes the point that POD information can in some cases be misleading. These claims are elaborated in more detail in the following paragraphs. These claims were investigated in chapter 4 of this thesis where applicable conclusions are presented.

The information provided by DMD that POD does not provide is primarily stability and phase information. Sampath and Chakravarthy claim that "although POD highlights the energy contribution of the flow structures, information related to their dynamics, specifically the stability of the flow structures is absent" [27]. Schmid also makes this claim saying that "despite this breakdown of the flow into energetic coherent structures, no information can be gained about the dynamics of these structures" [22]. In the same token, he does acknowledge that "techniques exist, however, to recover phase information from the dataset" citing Lumley in 1970 [29]. It is important to recognize that the techniques to recover phase information are easy to perform, but not inherent to the algorithm itself. DMD recovers phase information as an inherent part of its computational algorithm.

Schmid [22] makes the claim for the second argument by stating that “the energy may not in all circumstances be the correct measure to rank the flow structures.” Both Schmid and Zhang claim that sometimes segregation of features based on a distinct frequency, rather than spatial orthogonality is more desirable for better information.

Finally Schmid [22] makes the case that the POD modes can be misleading in the sense that the high energy modes may not contain all of the information that is relevant to the flow. He describes these as “dynamically highly relevant but zero energy modes.” Zhang also contends that in flows where prominent features are highly frequency dependent the orthogonality constraint issued by POD may do more to hinder rather than enhance the correct extraction of the feature. He says, “The results showed that each POD mode exhibits non-negligible contamination by the other uncorrelated structures while the temporal DMD analysis separately extracts the desired structure without discernible contamination” [28]. In other words POD modes contain structures with multiple frequencies.

2.5 Inlet Distortion

Inlet flow distortion may consist of non-uniformity in a single flow property, or there may be distortions in multiple flow properties. The distortion may be distributed in a predictable manner in the radial or circumferential directions, or it may be randomly distributed. Inflow conditions are usually categorized into two classes, one is the steady-state, circumferential and/or radial variation of flow, and the other is the so-called dynamic distortion where the flow is time-variant. The three major distortion sources (total pressure, total temperature, swirl) are related with each other in a highly nonlinear fashion. For example, the time variance of static pressure causes total temperature to change, which could produce a commensurate change in total pressure. The source of inlet flow distortion may also be transient. Temporary inlet flow distortions may be caused by a high angle of attack flight maneuver or by the ingestion of exhaust. Continuous inlet flow distortions may be caused by the geometry of the inlet itself or by the geometry of other nearby surfaces [30]. Figure 2.4 contains some illustration of the inlet distortion types described above. Figure 2.4a

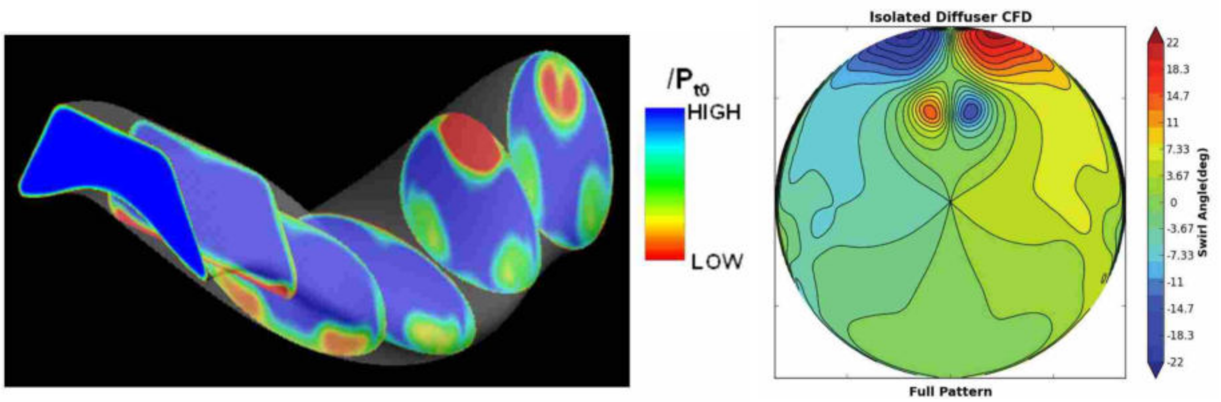

(a) Total pressure distortion formed in a curved duct.

(b) CFD contours of swirl angle of a simulation with an isolated diffuser.

Figure 2.4: Examples of distorted inlet patterns taken from [45,46]

shows an example of total pressure distortion pattern that is the result of irregular geometry at the inlet. This distortion pattern is circumferential primarily, but also has some radial components. Figure 2.4b is an illustration of swirl angle contours at the inlet. Swirl changes can affect both total pressure and temperature.

Since the early days of aircraft engine installations, the effects of distorted inflow and incoming turbulence to gas turbine engines have been a concern. This concern is more pronounced as increasingly advanced aircraft are designed for a wide range of operations and high fuel efficiency. For circumferential distortion, the total pressure distortion, especially the per-rev type, has been studied and modeled the most [31–38]. The effect of total temperature distortion was later recognized as a consequence of weapon gas ingestion, vertical take-off and landing, steam ingestion during aircraft carrier operations, and mid-air refueling (gas leakage consumed by the fan). In recent years, swirl distortion has been identified as the third major flow distortion initiator in addition to total pressure and total temperature distortions [39–44]. Inlet swirl distortion can be generated by flight maneuvers and flow condition near the aircraft. For commercial airplanes, congested air traffic at busy airports causes swirl (i.e. taking off after inlet distortion of total temperature and total pressure. The nacelle droop can sometimes cause inlet swirl distortion as well. For high-performance applications, complex inlets generate swirl at the fan face even if the inlet flow is uniform [45, 46]. Different patterns and scales of swirl distortion, such as bulk swirl, peak swirl, and vortex swirl, have different effects on the rotating compression system [30]. In addition to stability concerns, vortex flow can set up harmonic content in the flow field that cause high-cycle fatigue.

An important aspect of distorted inlet flows is distortion transfer and generation. Distortion transfer studies how the distorted inlet conditions influence the flow downstream. For example, a total pressure distortion at the inlet will cause the total pressure profile to continue through the fan. This will also cause a static pressure distortion pattern to propagate through the fan. The static pressure will cause a force imbalance causing a mass redistribution throughout the circumference of the fan. This, in turn, causes a phase shift in the pressure distortion. This phenomonon is explored in detail in [1]. Distortion generation is the appearance of distorted profiles that did not exist before. For example, with a total pressure distortion pattern with uniform total temperature at the inlet, a total temperature distortion pattern appears inside the machine. This phenomonon is identified in [1,36,47].

2.6 3-Stage Fan Simulations

The fan geometry for the simualtion data used in this analysis has been studied before with a 1/rev total pressure distortion inlet condition. Yao, Gorrell, and Wadia study this data in [47] and [36]. These papers do not use POD as a tool for analysis but draw conclusions about distortion and transfer generation using traditional methods. The conclusions made in these papers serve as a useful benchmark for comparison to establish the validity of POD in its ability to draw the same conclusions. These papers also serve as a meaningful foundation for the additional insight into the flow physics of distorted inlet conditions provided through the analysis of POD modes and coefficients.

Part 1 [47] primarily focuses on distortion transfer and generation through the three blade rows of two rigs and the response of the fan to these conditions. The paper begins by comparing and validating the numerical simulations to be studied to experimental data. The simulations calculated using PTURBO were shown to agree very well with the experimental measurements of total pressure and total temperature. The simulations were considered to be valid in their ability to characterize both the magnitude and general behavior of the distortion patterns. The primary analysis in part one is related to distortion transfer of total pressure and distortion generation of total temperature.

The main conclusions were the validation of the CFD by its match to experimental data and a phase lag in the temperature distortion pattern. The phase lag predicted was 90 degrees between the temperature and pressure. This phase lag was present throughout the fan.

Part 2 [36] of this paper series expands the analysis to the entire component instead of just selected blade rows. This paper explores further the mechanism for distortion transfer and generation, including the phase difference between temperature and pressure. They attribute the mechanism for distortion transfer and generation to be dictated by the static parameters. The static parameters change phase after each blade row. The total parameters do not exhibit this behavior. The authors came to the conclusion that static parameters were more revealing than the stagnation parameters. This attitude was also adopted for the POD analysis. The analysis also finds that the distortion is amplified through the first stage, is carried through the second stage and is attenuated at the exit. The authors conclude that the distortion throttles the last stage even though the exit conditions are unchanged. It was concluded that this throttling is what makes the last stage the limiting stage for the whole fan. A similar analysis is performed in the results section of this thesis, illustrating the same behavior.

Weston and Marshall analyze some of the same geometry as Yao and Gorrell, this time using the unsteady CFD solver OVERFLOW 2.2 [1,48,49]. The primary objective of this research was in the validation of the unsteady CFD solver OVERFLOW 2.2. There was also some nice analysis of the physics of distorted flow. Weston studied the flow physics of inlet distortion transfer and generation at various operating conditions. His simulations at the design and near stall operating condition provide the data which will be examined further using POD analysis techniques. The main aspects of the analysis include quantifying the phase and amplitude of pressure and temperature distortion. He also looked at the effect of distortion on operating point and the effect of distortion on stability margin.

Blanc also explored the OVERFLOW data generated by Weston to study inlet distortion using POD as the primary tool for analysis [2,4]. He proposed and validated the method of repeating geometry as being equivalently accurate to the method of snapshots for characterizing the circumferential variation of the flow due to the distorted inlet. This conclusion will prove to be a boon to the research currently being done because it necessitates far less data to be analyzed in order to harvest the same information. The method of repeating geometry was the method of choice for all of the POD analysis performed for the research in this thesis. Blanc performs an insightful analysis of the static pressure variation for rotor 3. The research performed in this thesis builds on the foundation laid by Blanc by adding extending the analysis to all three rotors as well as to additional variables such as axial velocity, temperature and entropy.

CHAPTER 3. METHOD

3.1 Analysis Techniques

The POD basis modes are ranked based on the significance of their contribution to representing the original data and are reported in descending order of relevance. The most pertinent modes are reported first, because the magnitude of the projection of the data onto them is larger than that of the modes following them. In this way the first mode captures the largest portion of information possible about the data. The following modes capture the next largest portion of information possible with the constraint that they must be orthogonal to the modes preceding them. There are no units associated with a POD mode. The units are carried by the coefficients, and the modes are normalized such that the magnitude is unity.

In general, mode 1 contains a representation of the data which is very close to the mean behavior although the absolute magnitude is not present. Mode 1 is useful for obtaining information on the most basic aspects of the flow. Mode 1 will reveal the magnitudes of structures relative to other structures which are present, as well as highlight the regions of features which are stationary. The higher order modes reveal flow structures that vary with the dimension selected as the column space. The structures contained in the higher order modes may not look like traditional flow structures, and so it is important to interpret them in the context of what is revealed in mode 1. Mode 1 identifies the structure, and mode 2 and above describe its variation. An example of this behavior is presented in Fig. 3.1. This example is taken from the cylinder in crossflow analysis presented in chapter 4 where full details are explained. Mode 1 of the vorticity shows the general wake structure behind the cylinder and shows the formation of vortices about to be shed. It is symmetric because mode 1 is a representation of the average behavior. Mode 2 contains the vortex shedding structure. Although the structure in mode 2 is an abstraction from what the actual vortex shedding looks like, when this information is considered in the context of the known vortex

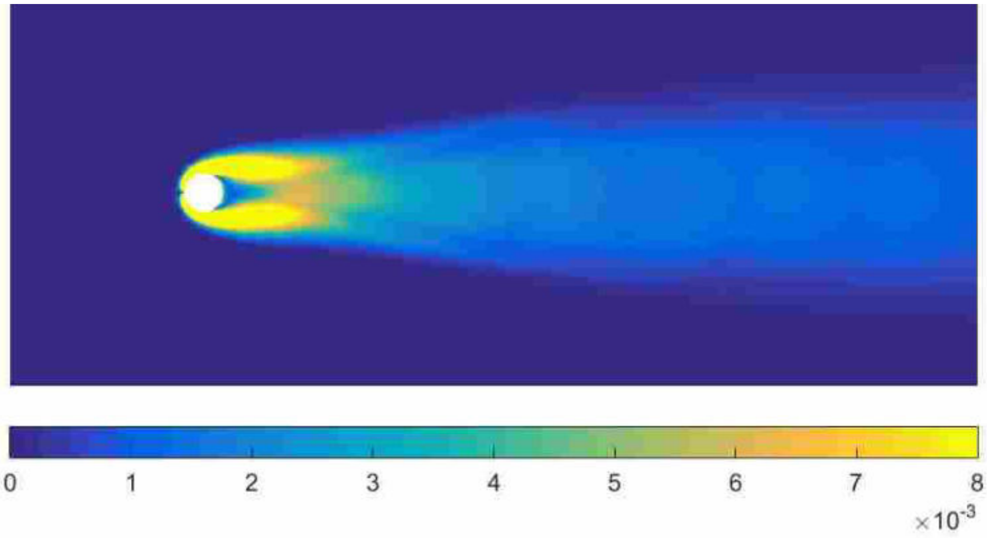

(a) Mode 1.

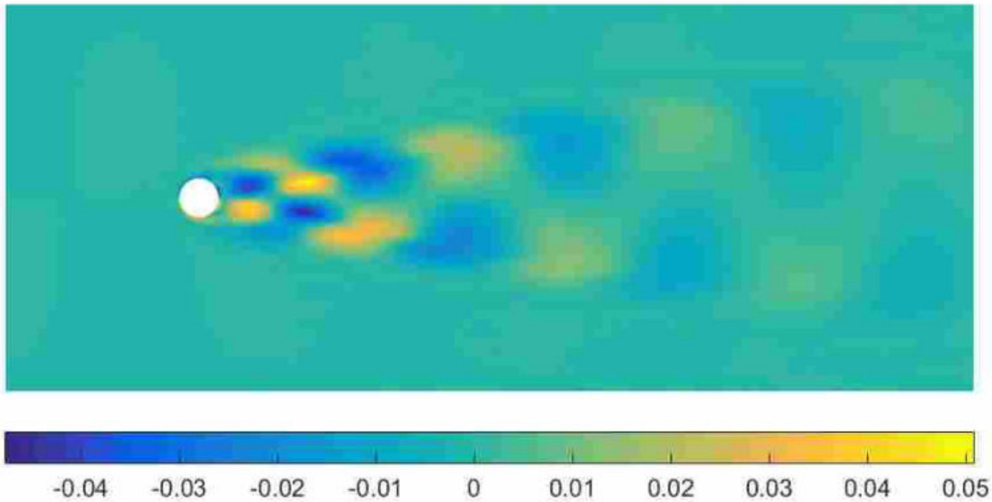

(b) Mode 2.

Figure 3.1: POD modes 1 and 2 of vorticity for a cylinder in crossflow.

shedding pattern, useful information can be gained. Mode 2 is also the variation from the mean behavior and may be interpreted in this context during observation as well.

The coefficient values indicate the variation of each mode with the columnspace. Coefficient values for modes 1 and 2 are shown in Fig. 3.2. The coefficients can be used to extract frequency information using Fourier analysis and identify general trends in the columnspace chosen. This technique may be used on mode 2 shown in the figure to extract the vortex shedding frequency for this situation. They indicate which modes contribute the most to a reconstruction of

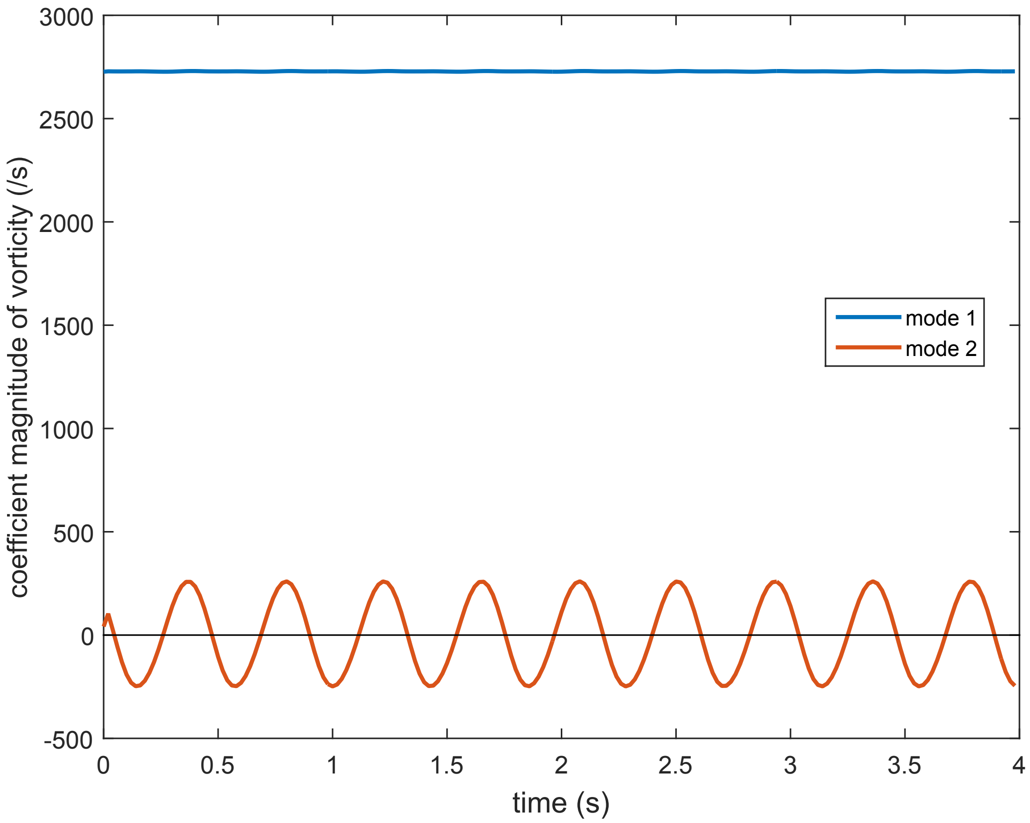

Figure 3.2: POD modal coefficient values for vorticity magnitude associated with modes 1 and 2.

the data at a given instant. Coefficients can also be used to examine the behavior of a particular mode through the dimension of the columnspace.

A useful technique for preliminary analysis of a dataset is a low order reconstruction using POD. In a low order reconstruction a selection of the lowest order basis modes, as well as their associated coefficients, is saved to represent the data, with the remaining modes, as well as the original data being discarded. In a low order reconstruction, the most obvious variation is included in the reconstruction, while the more subtle perturbations in the data captured by less significant modes are discarded.

Following the analysis of the low order reconstruction, further analysis might proceed in the direction of observation of individual modes and coefficients. These can be used to extract information about features of interest identified in the low order reconstruction phase of the analysis.

POD allows control over which flow variables are carried by the coefficients and which variables are carried by the modes by the selection of snapshots that vary with a given dimension such as time or space. This is extremely valuable because it allows for isolation of phenomenon based solely on a particular dimension such as time. The POD analyses presented in this paper were calculated such that the modes carried information on the spatial variation, and the coefficients carried the information on variation of the data corresponding to the angular location of the blade.

In general, POD is well suited to analyze any data set with variation in time or space. In order to optimize the benefits of POD, dimensions with the most variation such as time, space, or other parameters should be chosen to be analyzed. However, any dimension may be analyzed with POD yielding information on the variation in that dimension. In this study we are interested in the blade to blade variability that occurs circumferentially with inlet distortion conditions. Since angular position of the blade is the dimension with the most profound variation due to the circumferential nature of the distortion, it is the optimum dimension for analysis. In comparison with clean inlet simulation data, a commensurate reduction in circumferential variation was observed due to the lack of distorted conditions at the inlet. However, blade to blade variability was observed to arise from other sources as the flow progressed through the fan which POD is also well suited to characterize. Thus POD is useful in providing information about variation in a particular dimension of interest, whether this variation is large or small.

This thesis presents POD results on the blade to blade variability that occurs with inlet distortion. In this case, angular position of the blade is the dimension with the most profound variation due to the circumferential nature of the distortion, and is thus the optimum dimension for analysis. In comparison with the clean case we see a commensurate reduction in circumferential variation due to the lack of distorted conditions at the inlet. However, we see blade to blade variability arise from other sources as the flow progresses through the fan which POD is also well suited to characterize. Thus POD is useful in providing information about variation in a particular dimension of interest, whether this variation is large or small.

3.2 A Helpful Example

The following section contains an example that may be useful for understanding the fundamental principle behind the primary action of POD, and why it is so useful for analysis of data. Figure 3.3 contains a collection of three vectors: **A**, **B**, and **C**, depicted twice on the right and left hand side of the figure. The two identical sets of vectors, with the same point of origin, length, and direction, are represented by two bases. The basis for the left set of vectors are the standard unit vectors $\mathbf{e_1}$ and $\mathbf{e_2}$. This basis is of sufficient rank to span the subspace in which these three vectors lie. In other words, using these unit vectors it is a simple matter to derive linear combinations of them to represent each of the vectors **A**, **B**, and **C** exactly.

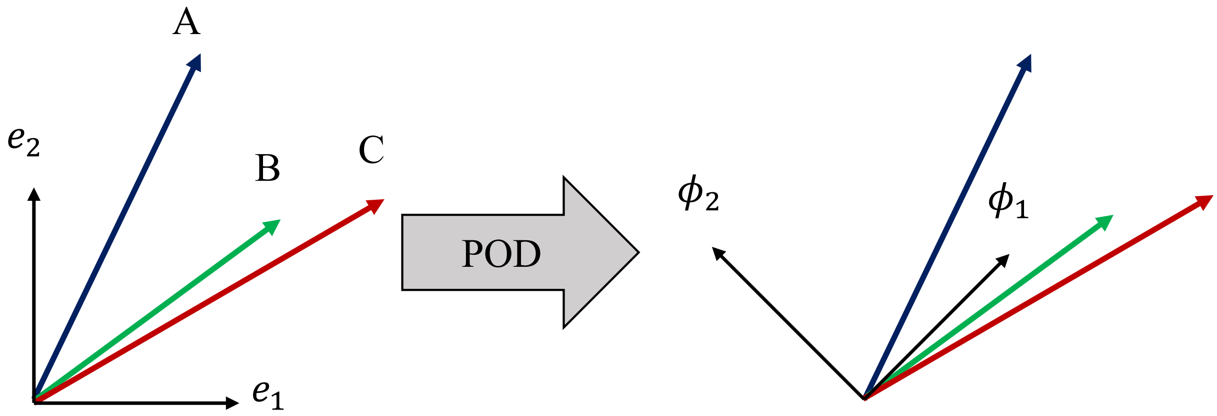

Figure 3.3: POD Example Using 2-Dimensional Vectors.

Although the first basis is more than adequate as a tool for describing the vectors, it is not ideal or optimal in the sense that neither of the two basis vectors are oriented to provide any more information about one vector than another. In fact, if one were compelled to pick just one basis vector and use it to reconstruct the data as best as possible, it would be a difficult decision. The best reconstruction using only one vector would in essence be selecting the vector that points in the general direction of the data the best. For example, picking $\mathbf{e_1}$ points roughly in the direction of **C** and so would be the best choice for that one vector, but $\mathbf{e_2}$ would be the obvious choice if one was interested in preserving vector **A**. With this in mind, the basis on the left seems less than ideal in any situation where the entire basis cannot be used to represent the data. In the same token, if one were to look at just the basis, and not see the vectors **A**, **B**, and **C** at all, it would be impossible to derive any information at all about the data by viewing just the basis vectors.

The basis on the right is the basis produced by POD. It is the ideal choice for representing the data when a limited number of unit vectors may be selected. These basis vectors are ranked according to their information content about the data they represent. In this way $\mathbf{a_1}\phi_1$ will always represent the best possible first order approximation of the data. This is what is meant by the phrase that the basis produced by POD is the optimum basis to represent the data. It is important to note that while POD is not constrained such that ϕ_1 will best represent every vector, it is constrained that ϕ_1 will be the best rank approximation for the dataset as a whole. This means that a selected number of vectors will maximize the projection of the data onto it better than any other set of vectors. In this way if the data were not viewed at all, and just the basis were observed, one could come to many conclusions about the general nature of the data. For example, observation of ϕ_1 would indicate that all of the vectors generally point in that direction. The magnitude of the coefficient vector for ϕ_1 would indicate generally how long each vector was. Observation of ϕ_2 would indicate the direction of the largest variation, and the magnitude of the coefficients would indicate how much. In a reconstruction of the whole dataset, the average error is smallest using the POD modes, but there is no bound on the local error. The reconstruction is also the best using mode 1. Using only mode 2 or a reconstruction would result in a higher error than a reconstruction using only mode 1.

This is a simple two dimensional example to illustrate how POD operates on a set of vectors. In practice, POD operates on vectors of thousands of dimensions. In this application, these vectors contain CFD data where each entry corresponds to a the scalar value at a given node. The action however, is the same. POD works to find the basis vectors which point in the direction of the data. In other words POD finds the basis vectors where the projection of the data onto them is at its maximum with the constraint that they are orthogonal to them. In this way, the basis modes produced prove to be a boon to engineers desiring to know as much information as possible about their data in the most consise way possible, all without having to observe the data directly.

3.3 D Matrix Formulation

In general, the scalar matrix **D** contains data from a rectangular grid that is a function of variables **X** and Y. The rows of **D** contain data spanning the range of **X**, and the columns span the range of Y. Generally the variable **X** represents a discrete spatial location, and Y can represent a range of other entities such as time, position, or some other parameter. In these situations, each column of **D** represents data corresponding to the same geometry at a different time step, or value of the selected *Y* parameter. Each row of the matrix corresponds to the same spatial location at different values of the parameter *Y*. This is illustrated in Fig. 3.4.

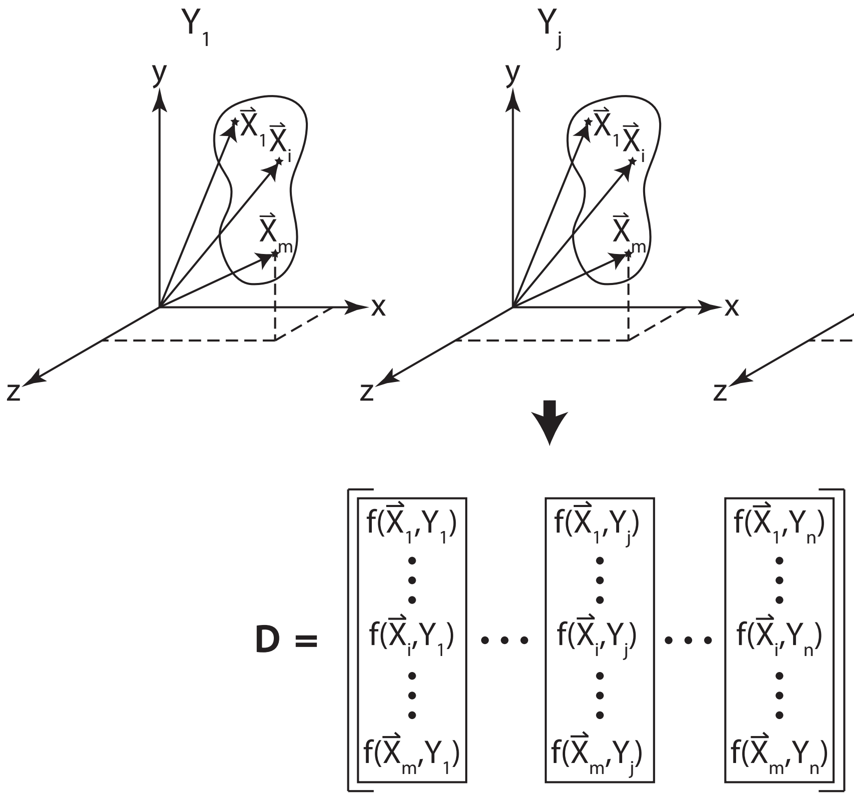

Figure 3.4: Illustration of **D** matrix formulation adapted from [4].

Examples in this study use **X** to represent the relative spatial location of points within a bladerow passage. Each entry in **X** corresponds to an x,y,z location. The variable *Y* is chosen to represent θ which is the circumferential angle of a given blade row passage. In this way *Y* represents the absolute position of the dataset.

The matrix **D** was formulated such that each column corresponded to the portion of extracted data from an individual blade row passage. A column was then created for each blade in the row being analyzed. Only one time step from the simulation results is required to compile the **D** matrix in this way. Although only one time step is used, the data extracted still captures the 1/rev distortion pattern, and the time-dependent structures of the flow. Each column of **D** corresponds to a so-called pseudo-time step because although data is taken from a different blade, if the first blade were allowed to rotate to the point of data collection, it would have approximately the same flow in that particular time step. This method is called the method of repeating geometry and is shown to be accurate for this type of flow in [4].

3.4 Computation Techniques

Once the matrix **D** is formed there are two methods to compute the POD basis modes. These are Singular Value Decomposition (SVD) and Eigenvalue Decomposition. Each yields ultimately the same result but the two use slightly different paths. SVD is the more straightforward of the two approaches where eigenvalue decomposition can be more computationally efficient if only a reduced selection of the modes is desired. Eigenvalue decomposition was the method of choice for this analysis to improve computational efficiency. A brief description of each method containing the basic equations and an overview is discussed below. More detail about each technique can be found in [4].

3.4.1 Singular Value Decomposition

SVD is perhaps the most straightforward operation to obtain the POD because the $m \times n$ matrix **D** may be of arbitrary size and the output requires the least manipulation to obtain the basis modes. It is a matrix factorization technique which transforms an $m \times n$ matrix **D** into the three matrices **U**, Σ, and **V** as shown in Eqn. (3.1). **U** and **V** are $m \times m$ and $n \times n$ orthonormal matrices, respectively, and Σ is an $m \times n$ diagonal matrix containing the singular values σ_i of **D**. As stated above, each singular value quantifies the proportion of variance captured by its corresponding basis mode. The columns of **U** represent the spatial basis modes ϕ_i and the columns of **V** contain the eigenvalues of $\mathbf{D}^T\mathbf{D}$. SVD is also a convenient method because many algorithms already exist for efficient implementation. The percent energy may be calculated from the singular values as shown in Eqn. (3.2) for a given number of modes r, where λ_j are the squared values of the singular values. The sum starts at index 2 because mode 1 is not included in the calculation of percent energy because the mean behavior is left out.

$$\mathbf{D} = \mathbf{U}\Sigma\mathbf{V}^T \tag{3.1}$$

$$P = \frac{\sum_{j=2}^{r} \lambda_j}{\sum_{j=2}^{n} \lambda_j} \times 100\% \tag{3.2}$$

3.4.2 Eigenvalue Decomposition.

Eigenvalue decomposition is also of value in the computation of POD basis modes because it allows the computation of individual basis modes. This can save computational expense if only the first few modes are desired for analysis. In this research often only the first few modes are used for analysis because higher order modes have been found to contain little relevant information. Thus, the eigenvalue decomposition method is the ideal method of choice for computation of the POD modes. The eigenvalue decomposition method generates the POD modes from the symmetric $n \times n$ matrix $\mathbf{D}^T\mathbf{D}$. The eigenvalues λ_i and eigenvectors $\mathbf{v}_i$ are calculated and arranged in the order such that $\lambda_1 > \lambda_2 \ldots > \lambda_n$ with the associated eigenvectors also sorted in the same order. The sorted eigenvalues correspond to the columns of $\mathbf{V}$. The singular values may be obtained from the square root of the eigenvalues. Finally the basis modes may be calculated as shown in Eqn. (3.3). The singular values are the square roots of the eigenvalues λ_i.

$$\phi_i = \frac{\mathbf{D}\mathbf{v_i}}{\sqrt{\lambda_i}} \tag{3.3}$$

3.4.3 Dynamic Mode Decomposition

The calculation of the DMD accepts the same matrix input as POD. An overview of the computational algorithm is provided here. A more indepth discussion of the mathematics is found in [23]. A MATLAB code executing the algorithm is found in appendix B.1. To compute the DMD a matrix $\mathbf{D}$ containing the data is formed as described in 3.3. The matrix $\mathbf{D}$ is operated on in several operations involving only a selection of columns. In order to be clear on these operations the notation $\mathbf{D_1^N} = \{\mathbf{d_1}, \mathbf{d_2}, ..., \mathbf{d_n}\}$ is adopted to indicate columns 1 through N where N is the total number of columns and $\mathbf{d_i}$ is a column vector. The matrix $\mathbf{A}$ is defined to be the linear mapping which connects the flow field $\mathbf{d_i}$ to the subsequent flowfield $\mathbf{d_{i+1}}$ as shown in Eqn. (3.4). The DMD modes produced by this algorithm are descriptions of the linear transformation matrix **A** as opposed to the POD modes which describe the matrix **D** itself. This is the primary difference between POD and DMD.

$$\mathbf{d_{i+1}} = \mathbf{A}\mathbf{d_i} \tag{3.4}$$

In practice, the matrix **A** is inefficient to compute for the case of discrete data according to Schmid [23]. For this reason a substitution is made in favor of simpler matrix to compute. The matrix **S** is calculated and the modes are computed for this matrix instead of **A**. The matrix **S** is similar to **A** by the definition of similar matrices where there is some matrix **P** such that $\mathbf{S} = \mathbf{P}^{-1}\mathbf{A}\mathbf{P}$. Similar matrices have the same eigenvalues and so Schmid makes the argument that the modes produced by this matrix **S** will capture the same dynamics as the modes of the matrix **A**.

Bearing in mind this substitution, the singular value decomposition of the first N-1 columns of **D** is taken yielding the result in Eqn. (3.5). It should be noted that the matrix **U** in this expression is the POD basis of the matrix $\mathbf{D_1^{N-1}}$. The POD basis **U** is the similarity transformation matrix used to transform **A** to **S**, i.e. $\mathbf{S} = \mathbf{U}^T\mathbf{A}\mathbf{U}$. The matrix **S** is calculated using the results of Eqn. (3.5) yielding Eqn. (3.6). Finally the modes are computed from the matrix **S** by computing the eigenvectors $\mathbf{y_i}$ and projecting them onto the POD basis computed in Eqn. (3.5). This step is shown in Eqn. (3.7). The eigenvalues of **S** when properly scaled contain information on the frequency and stability of the corresponding flow features. The correct scaling is shown in Eqn. (3.8).

Calculating the magnitude of the projection of each DMD mode onto the POD modes 2 through 4 calculated from Eqn. (3.5) yields a measure of the coherence of the DMD modes to the POD modes. Coherence is a term introduced by Schmid as a way to sort DMD modes according to their similarity to the POD modes. In this way the modes are able to be sorted based on their energy content. DMD provides no way to sort the modes so there is no way of evaluating which ones contain the most information about the flow. The coherance is calculated through the projection of the DMD modes onto a selected number of POD modes through a scalar product. This yields a vector of coherence values for each POD mode associated with each DMD mode. The magnitude of this vector is the coherence norm for a given DMD mode. It is the magnitude of the coherence norm which is used to sort the DMD modes according to their relevance to the flow. This procedure is illustrated as the last step of the MATLAB code included in Appendix B.1.

$$\mathbf{D_1^{N-1}} = \mathbf{U\Sigma V^T} \tag{3.5}$$

$$\mathbf{S} = \mathbf{U^T D_2^N V \Sigma^{-1}} \tag{3.6}$$

$$\phi_i = \mathbf{U y_i} \tag{3.7}$$

$$\mu_{scaled} = \frac{ln(\mu_i)}{2\pi\Delta t} \tag{3.8}$$

3.5 High Fidelity Fan Simulations

The simulations used in this study were calculated using the NASA CFD code OVERFLOW 2.2 modified to include propulsion capabilities [50]. OVERFLOW utilizes a time marching approach to the three-dimensional Navier-Stokes equations. The simulations are fully unsteady with one revolution of the blade requiring 7000 time steps. Convergence was defined when mass flow at blade leading inlets and exits settled to a stable average value. For a more detailed discussion of these computations, see the work of Marshall et al. [49] and Weston [1]. OVERFLOW uses structured overset grids.

The fan geometry is shown in Fig. 3.5, which includes 7 blade rows, namely an Inlet Guide Vane (IGV) and 3 rotor/stator stages. The fan computational domain consisted of 660 million nodes. Since OVERFLOW2.2 does not include non-reflecting boundary conditions, extended inlet and exit sections were included in the domain to provide better numeric stability for the simulation. The inlet boundary condition for the distorted case was a 1/rev sinusoidal total pressure distribution with a 20 percent amplitude of variation. This distribution is illustrated in Fig. 3.6. The exit boundary condition was defined using the method of Vahdati [51] where a variable area converging nozzle exit domain was used. The nozzle was placed just before the exit plane. This approach uses the unique characteristics of a choked flow to vary the operating condition of a fan. When

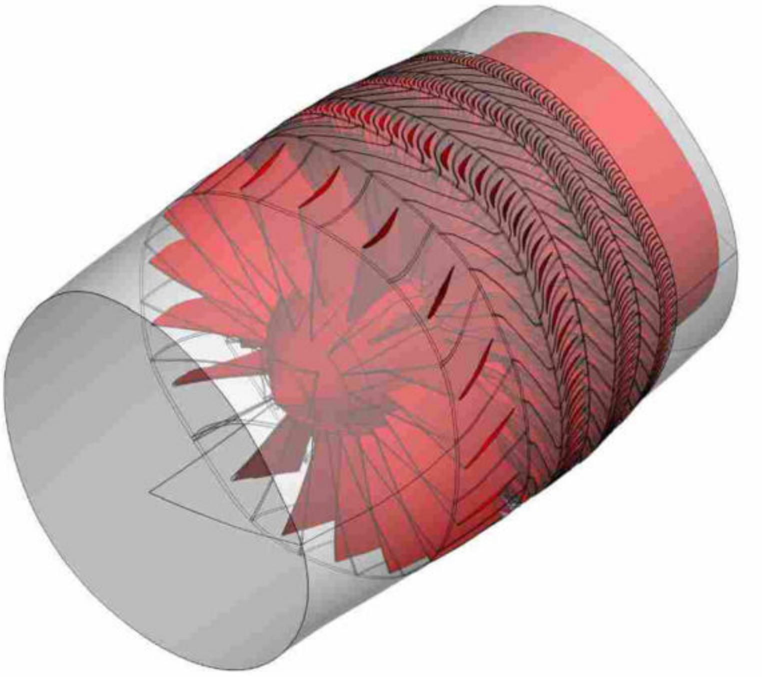

Figure 3.5: Computational domain consisting of seven regions and 660 million nodes.

flow through a converging nozzle is choked the massflow at that flow condition is the maximum possible for a given nozzle area. By specifying a sufficiently low back pressure at the exit plane, the nozzle will always be choked. This makes the massflow and pressure ratio through the entire fan dependent on the exit area of the converging nozzle at the exit plane, thus simulating a physical throttle. To ensure a choked nozzle the simulations used a nozzle exit static pressure boundary condition equal to the inlet total pressure. The exit boundary condition was specified to be equal to the average inlet total pressure at the exit surface. A nozzle was placed before the exit in order to throttle the mass flow through the rig. The nozzle area could be reduced in order to simulate different operating points along a speed line. The nozzle was placed nearly half the length of the fan downstream of Stator 3 to prevent any of the nozzle's behavior from traveling upstream to interfere with the flow through the fan geometry [38].

3.5.1 Time Average Simulation Results

Figure 3.7a shows the speedlines generated from time-averaged results of both the distorted and clean simulations. The values are non-dimensionalized by the experimental massflow and

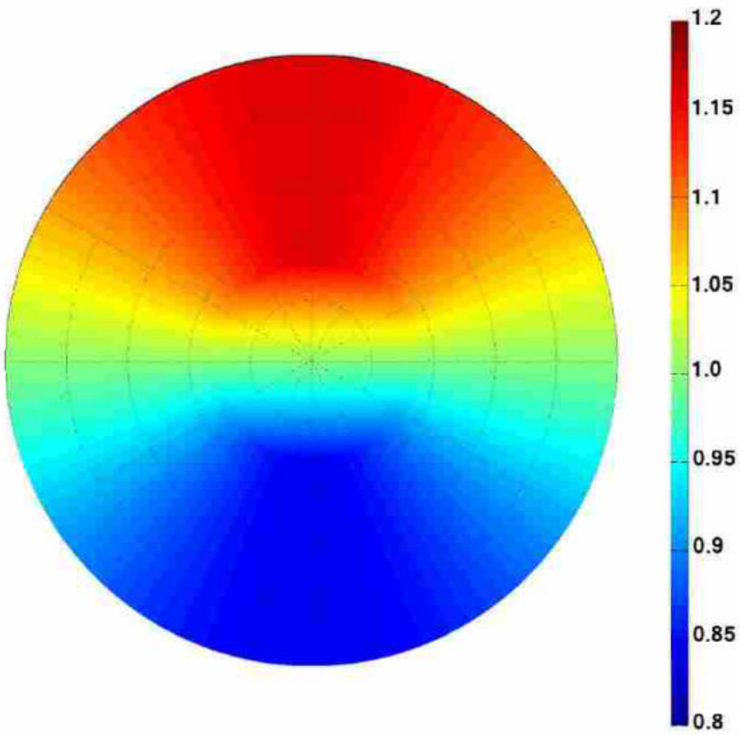

Figure 3.6: Total pressure inlet boundary condition with a 20% 1/rev distortion pattern. The magnitude is normalized by freestream conditions

pressure ratio of the design operating point. For clean inlet the peak efficiency point corresponded to the 0.88 pressure ratio and for the distorted case the peak efficiency corresponded to the 1.08 pressure ratio. The distorted case approaches stall much sooner than the clean case. The near-stall point (lowest massflow for both series) shows a massflow nearly 3% higher for the distorted case than in the clean case. The pressure ratio at stall for the distorted case is also approximately 20% lower than the clean. The range of massflow predicted by the distorted simulations is less than 3% of the design massflow, as opposed to a range of over 5% for the clean flow. Efficiency plots and other details are provided in [52].

Figure 3.7b shows the stage by stage pressure ratios for the various operating points in this study. This data has been normalized by the experimental pressure ratios for each stage. The peak efficiency point corresponds to a normalized massflow of 1.007 and the near-stall operating point corresponds to a normalized massflow of 0.984. The third rotor stage is apparently responsible for most of the variation between the pressure ratios of the operating points, as the other two rotor stages do not deviate far from the values of the operating point. The first rotor stage shows a regular

(a) Speedline of fan in both clean and distorted cases.

(b) Stage by stage characteristic map of distorted fan

Figure 3.7: Time-averaged flow characteristics

increase in pressure ratio between each operating point. Interestingly, the second rotor stage shows a slight decrease in pressure ratio between the peak efficiency and near stall points, and the third rotor shows a much smaller increase in pressure ratio between the same two points.

3.6 Data Extraction

Nodal solution data from each simulation was extracted from a radial surface at thirty percent immersion from the outer diameter for each rotor blade row as seen in Fig. 3.8. The same nodes were used in the extraction for each simulation. The data was then arranged into a **D** matrix for POD operations.

Space limitations prohibits the presentation and analysis of data at other immersions. Data extracted at 10%, 30%, 50%, 70%, and 90% immersions can be found in references [48] [1]. 30% immersion was chosen as it is representative of the fan performance without endwall effects and focused the scope of this paper on investigating the effects of distortion on shock intensity and movement.

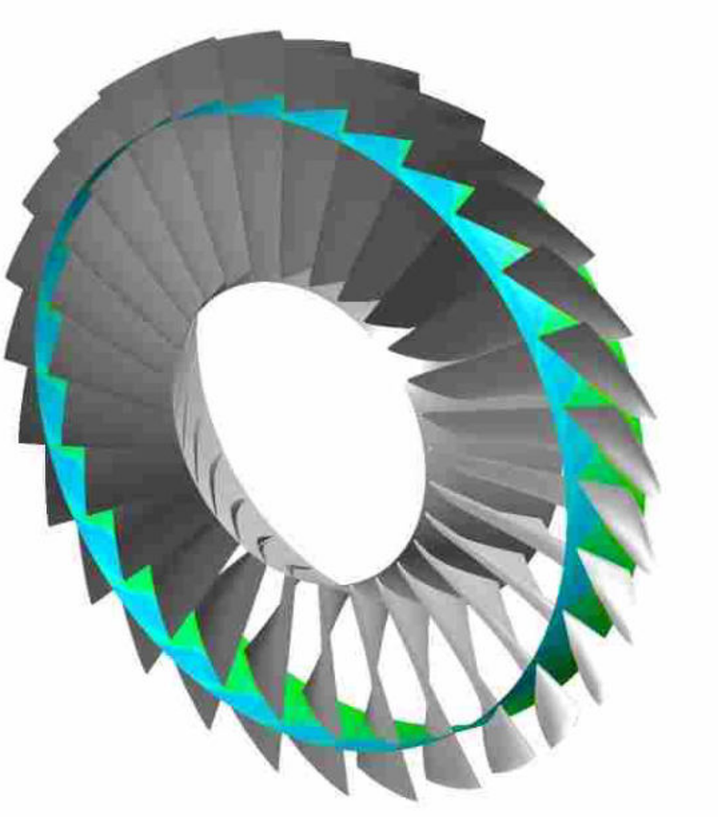

Figure 3.8: Extracted data at 30% immersion for each blade passage in a given rotor.

3.7 Calculation of the POD

Data was taken for each blade in the row being analyzed so that a separate **D** was formed for each of the three rotor blade rows at the distorted operating condition for static pressure, axial velocity, static temperature, entropy, and entropy flux. Each of these **D** matrices were compiled with an associated POD calculation. The first four modes were used in the following comparisons because they typically corresponded to the largest singular values. Clean inlet comparisons were made for comparison to baseline operating conditions, and establishing which phenomenon is caused by distortion and which is only influenced by the distorted inlet. The clean inlet simulations use the same simulation configuration described above, with the substitution of a clean inlet boundary condition with no distortion. The same nozzle area reduction technique was also used to simulate the various conditions along the speedline.

While there are many variables that could be analyzed this thesis focuses on the static pressure and axial velocity, and entropy flux. Static quantities help comprehend the role of velocity distortion since the stagnation parameters have an overall masquerading effect and may not reveal the underlying mechanism completely. This was determined when Yao et al [47] and [36] investigated the circumferential phase difference between total pressure distortion and generated total temperature distortion. Static pressure also identifies induced swirl due to the imbalance of the static pressure in the circumference caused by the total pressure distortion. From a designers perspective analysis of the rotor blade static pressure distribution provides insight into the effect of the 1/rev distortion on loading, shock strength, shock location, pressure rise, and incidence. Axial velocity useful variable of interest because of its ability to capture features which are not captured by pressure such as boundary layers and separation regins.

CHAPTER 4. RESULTS

The results presented in this chapter were chosen in order to illustrate the most insightful aspects of the POD analysis including the breadth and depth of its capabilities. Variables of static pressure, entropy flux, and axial velocity were analyzed to explore the flow physics of 3 rotors of a compressor with a distorted inlet. Design and near stall operating conditions were analyzed and compared as well as a clean inlet comparison. In the beginning of the section on static pressure, a more detailed discussion of the case of distorted inlet at design, rotor 1 is presented. Plots of the modes and coefficients are included to explain their characteristics and general appearance. Low order reconstructions are then presented to demonstrate the information extracted from the data by each mode. This section is included to illustrate the basic aspects of a POD analysis and the level of depth that a POD analysis can achieve. A rotor comparison of the distorted data is then presented followed by comparisons to the clean inlet simulations. The analysis of static pressure then moves on to the comparison to the near stall operating condition. Following static pressure is the analysis of axial velocity. A similar analysis is performed to static pressure this time in the context of the new flow features revealed. A modal analysis is performed and is compared to a more traditional analysis of the flow to confirm the conclusion of separated flow. The analysis then includes a comparison to near stall and a clean inlet comparison. Finally, the analysis of entropy flux is presented. The analysis of entropy flux does not reveal new flow features but is focused on the property itself through the fan and how this variation is related to irreversibility.

POD analysis for this research was performed on total and static pressure, total and static temperature, entropy, entropy flux, and axial velocity. It was found that static pressure, entropy flux and axial velocity were best at communicating the variety of flow physics in these simulations. Many attributes are common among each of the simulation datasets analyzed using POD. These common attributes are commented on but often not presented for brevity. Instead, plots that best illustrate the the similarities and differences between clean and distorted flows at design and near stall operating conditions through the three stages are presented. Although many of the modes are not included or commented on, they are all included in Appendix A for reference. This presentation is then intended to illustrate the ability of POD to delve deep into a specific flow condition, or provide a broad comparison of several flow conditions quickly and effectively.

4.1 Static Pressure

4.1.1 Modal Analysis: Distorted Inlet at Design, Rotor 1

Figure 4.1a depicts mode 1 of the POD of the static pressure at rotor 1 of the distorted simulation at design operating condition. Mode 1 contains information on the average behavior of the flow. The presence of the bow shock at the leading edge of the blade can be readily seen as well as a portion of the bow shock from the following blade. None of the values of the mode are zero which means that this mode contributes information to the flow over the entire blade passage.

Figure 4.1b depicts mode 2 of the dataset. The majority of the values in this mode are close to zero, with regions of high magnitude concentrated in the locations of the shock waves. Higher order modes contain information representing the variation of the data from the mean values. Therefore, the information they carry is concentrated around flow features that vary with time and space. The shockwaves in this distorted inlet flow move upstream and downstream in response to the pressure variation resulting from the inlet distortion. Mode 2 of this POD aids in characterizing the motion of the shock waves. If the motion and amplitude of the shock wave were a linear phenomenon, the shock could be characterized with only a scalar multiple of mode 1. However, this is not the case, so additional modes are necessary to capture the nonlinear amplification or attenuation of the shockwave magnitude and/or motion.

Modes 3 and 4 (Figures 4.1c and 4.1d) share many characteristics of mode 2 with the majority of values being close to zero and the presence of regions of high magnitude values in regions around the shock. Modes 3 and 4 aid in characterizing the exact location of the shock front at a given angular location and also characterize the motion of the shock as the blade rotates.

Modes 2, 3 and 4 contain a higher magnitude range of values than mode 1. This is because the majority of the values of modes 2, 3 and 4 are close to zero while the values farther from zero have much higher magnitudes in order to satisfy the constraint that $\|\phi\| = 1$. The values of

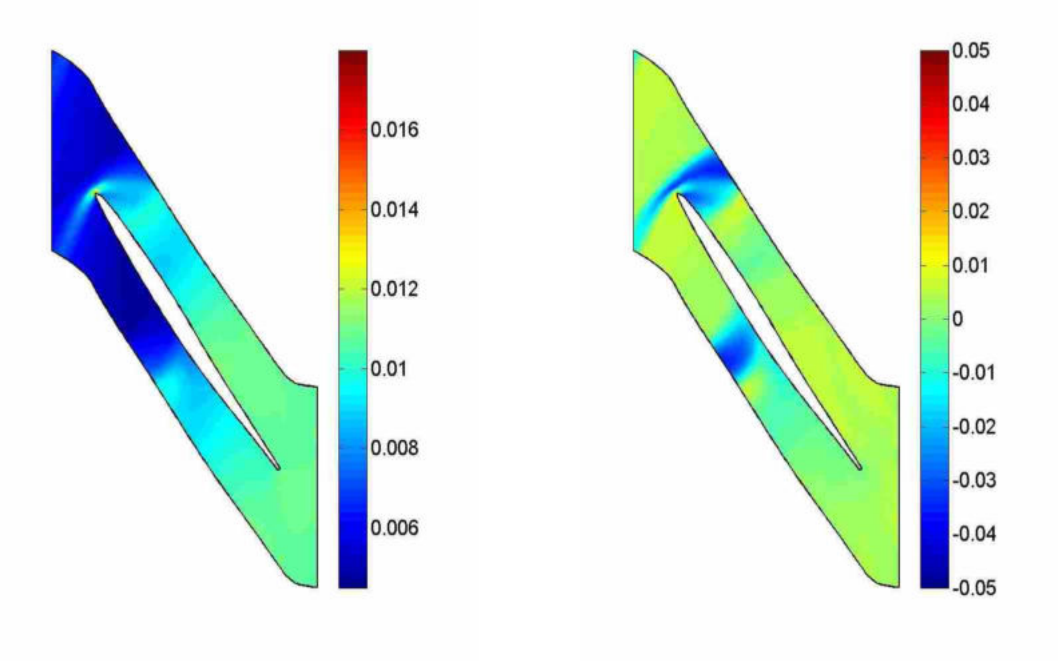

(a) mode 1 (b) mode 2

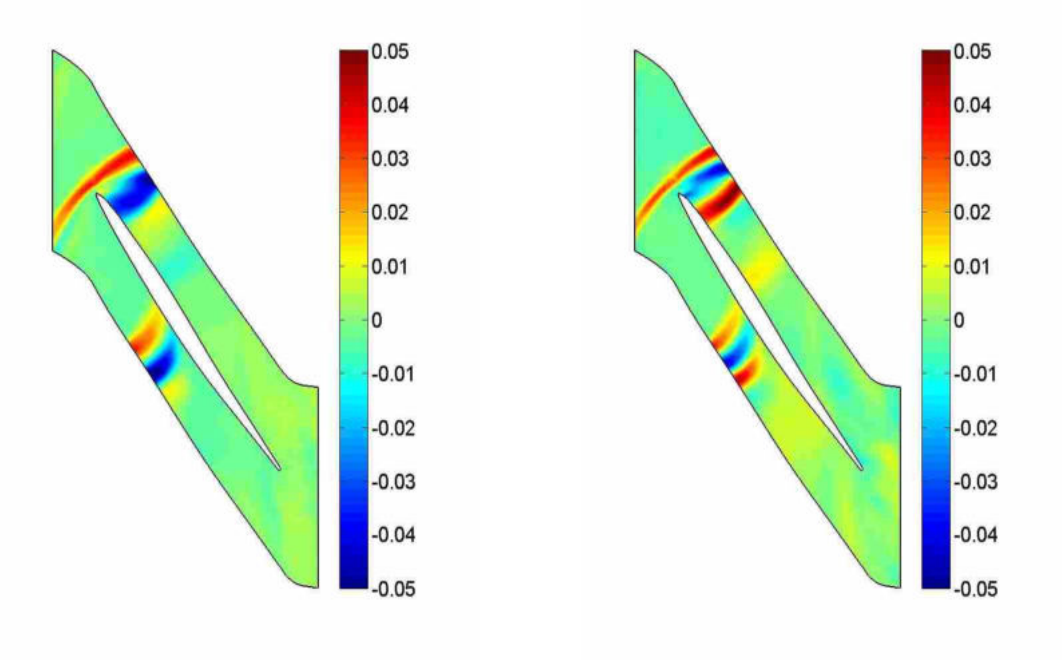

(c) mode 3 (d) mode 4

Figure 4.1: POD modes 1-4 from distorted inlet at design operating condition, rotor 1, static pressure. Note that mode 1 clearly contains the passage shock structure as discussed in the text.

mode 1 are of much smaller magnitude because the mode carries information over a very broad range, i.e. the average behavior for each node. Modes 2, 3 and 4 carry information over a much more limited range, i.e. almost only on the shock wave, so the areas containing information are of much higher magnitude. While the relative values of the modes are important for the identification of flow features and their variation in time and space, it is the associated modal coefficients that determine the influence of each mode in the reconstruction of the data.

4.1.2 Coefficients.

The coefficient values associated with the modes of Fig. 4.1 are shown in Fig. 4.2. The standard deviation for each coefficient vector is also included in the legend. Standard deviation is discussed later as a useful metric for the analysis of distortion transfer. While the modal values are associated with a particular location in space, the coefficient values are associated with a particular angular location in the blade row. The coefficients then capture the variation in the data with angular position, or time if the blade were allowed to rotate through the distortion to that location. As seen in Fig. 4.2, the coefficients for mode 1 capture the effect of the 1/rev distorted inlet condition with the same 1/rev pattern. The amplitude of this coefficient vector contains information on the magnitude of the distortion. The coefficients for mode 1 are not centered about zero whereas higher order coefficient sets are. This is because the coefficients for mode 1 contain information regarding the magnitude of the data. Higher order coefficient sets capture the information on the fluctuation from the mean. It is also notable that when the coefficient value associated with a particular mode is zero, that mode contributes no information to the flow at that instance. The mode 1 coefficients are far from zero so mode 1 always contributes information, whereas subsequent modes cross zero regularly such that there are angles when there is no contribution from the mode at all.

It is important to note that the values associated with modal coefficients do carry units unlike the modes themselves which are unitless analogous to unit vectors. However the absolute values of the coefficients are not meaningful until multiplied by the appropriate modal value. Coefficient values are useful for determining the relative behavior of the flow as the blade rotates. Meaningful absolute values are found by combining the modes and coefficients through a reconstruction. The data in this study is normalized by reference conditions and is therefore unitless, thus so are the coefficients, which is why no units are listed on the ordinate of Fig. 4.2.

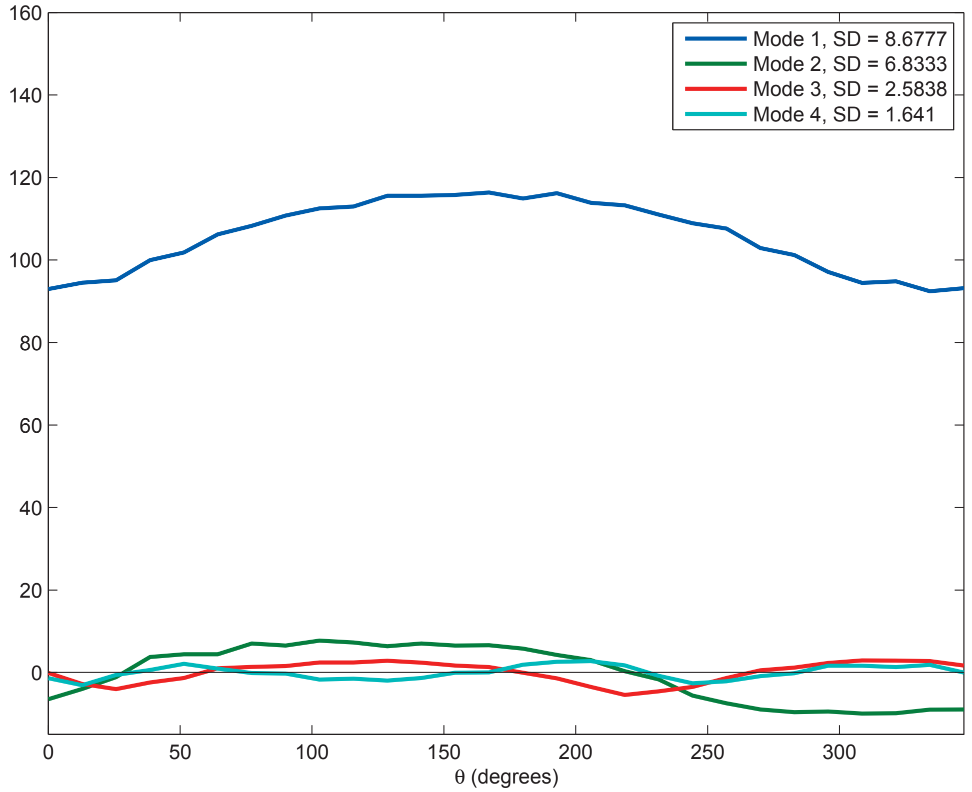

Figure 4.2: POD modal coefficient values associated with modes 1-4 and corresponding standard deviation (SD).

It is also observed that the 1/rev pattern is dominant in modes 1 and 2. This suggests that the 1/rev inlet condition has the most profound effect on the features characterized by their associated modes. Mode 1 captures the average behavior of the flow. Mode 2 captures the oscilating behavior of the shock wave. The higher order modes can be combined to reconstruct the exact location of the shock wave on the blade at a given angular position. It can therefore be concluded that inlet distortion has the most profound effect on these flow aspects [37].

Figure 4.3 depicts the singular values associated with the data. The singular values always decrease and are a reflection of the relative contribution of each mode to representing the data. As can be seen in the figure, a large portion of the information contained in this flow is characterized by the first three modes associated with the largest singular values. Additionally, a much larger portion of information is captured by mode 1 than mode 2, mode 2 than mode 3 etc.

The singular values may be used to evaluate how many modes are significant to the POD analysis. As can be seen in the figure there is initially a sharp decrease in the singular values,

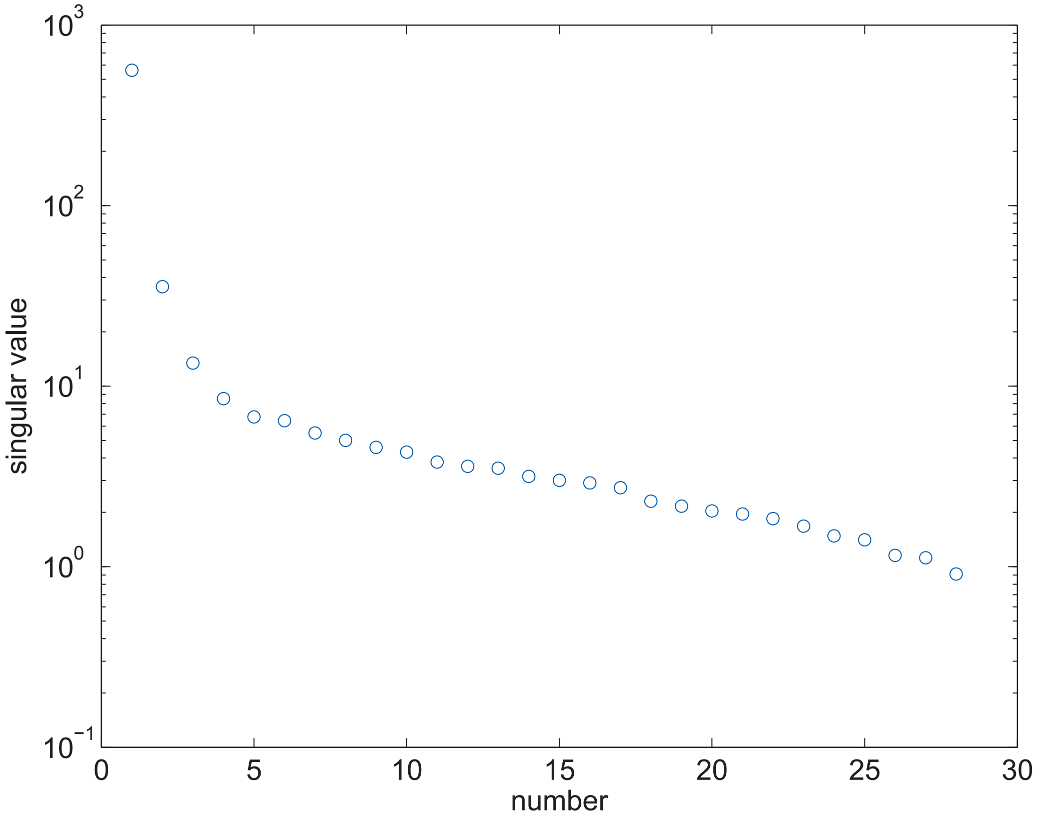

Figure 4.3: POD singular values.

followed by an abrupt transition to a much more gradual slope. This transition happens between modes three and four. The exact mode that this transition happens at may vary for a given dataset, but it was found that this transition generally never occured later than mode 4 for all of the data performed in this analysis. For this reason only the first four modes are included in the analysis. The higher order modes correspond to singular values so low that their relative contribution to the data is minimal. The singular values are the best place to start in an evaluation of how many modes to use in an analysis. It is suggested that the number of modes used in the analysis is selected based on the criteria described above. The following section containing low order reconstructions of the data illustrates the relative contribution of each mode as shown by the singular values.

4.1.3 Low Order Reconstructions

In order to appreciate the information captured by each mode, it is useful to visualize the mode's contribution to its associated low order reconstruction. The following reconstructions of order 1 through 3 illustrate the aspects of flow characterized by modes 1 through 3. Figure 4.4b is a representation of the first order reconstruction for rotor1, blade 10 with Fig. 4.4a displaying a plot of the original static pressure data. Figure 4.4e displays the associated reconstruction error which is calculated by subracting the reconstruction from the original simulation data. It can be seen that mode 1 captures the majority of the flow information but neglects the finer resolution aspects of the shock waves. The largest values of error are concentrated in the region around the bow shock. This is because the location of the shock varies depending on circumferential location because the inlet distortion affects the location of the shock. Mode 1 does not capture this phenomenon. It is the subsequent modes that carry the information about the location of the shock.

The second order reconstruction is produced using modes 1 and 2 and is depicted in Fig. 4.4c. This reconstruction provides much more detail on the location of the shock wave and the error around that region seen in Fig. 4.4f decreases significantly. This error is diminished further in the third order reconstruction produced from modes 1, 2 and 3, shown in Fig. 4.4d and 4.4g. However, the rate at which the error is reduced with each increase in order is slowing down. This is because each mode is contibuting less and less information proportional to the singular values (Fig. 4.3). Higher order reconstructions continue to hone in on the location and amplitude of the shock wave, and once that is well established additional modes contribute only minor perturbations spread throughout the data.

4.1.4 Rotor Comparison, Distorted Inlet at Design

Similar analyses can be done for each rotor individually, and then compared to glean insight into distortion transfer and generation, as well as the overall compression process. The modes for rotor 3 capture the same flow features as rotor 1, but with different magnitudes and spatial locations. The mean flow is captured in mode 1 with subsequent modes 2 through 4 having values mostly close to zero and providing higher magnitude information over a more limited spatial area. This is mainly concentrated around the shock wave to capture its motion.

It is important to recognize that care must be exercised when comparing POD output for different datasets. Differences in grid size or flow physics may influence the magnitudes of POD output such that direct comparison of exact values of modes and coefficients may not be meaningful. In the analysis below, the modes and coefficients for the rotors are compared for static

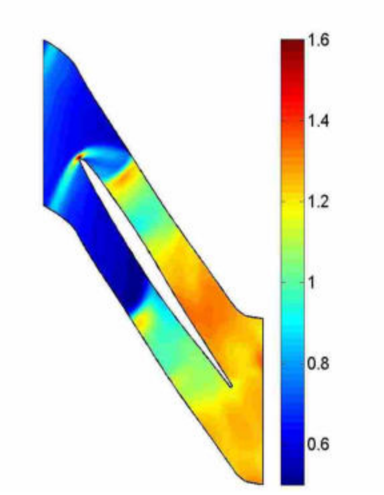

(a) original

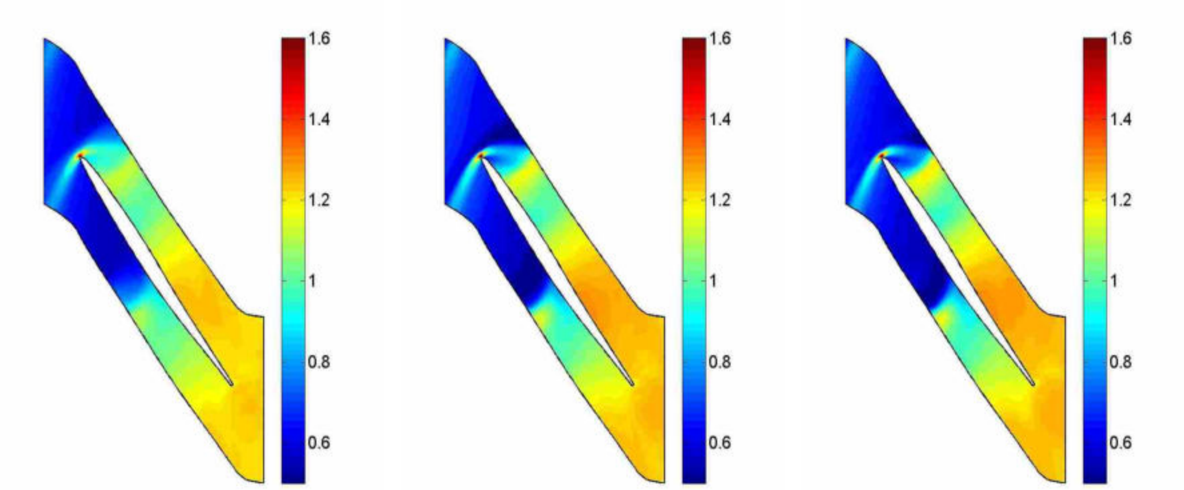

(b) order 1 reconstruction (c) order 2 reconstruction (d) order 3 reconstruction

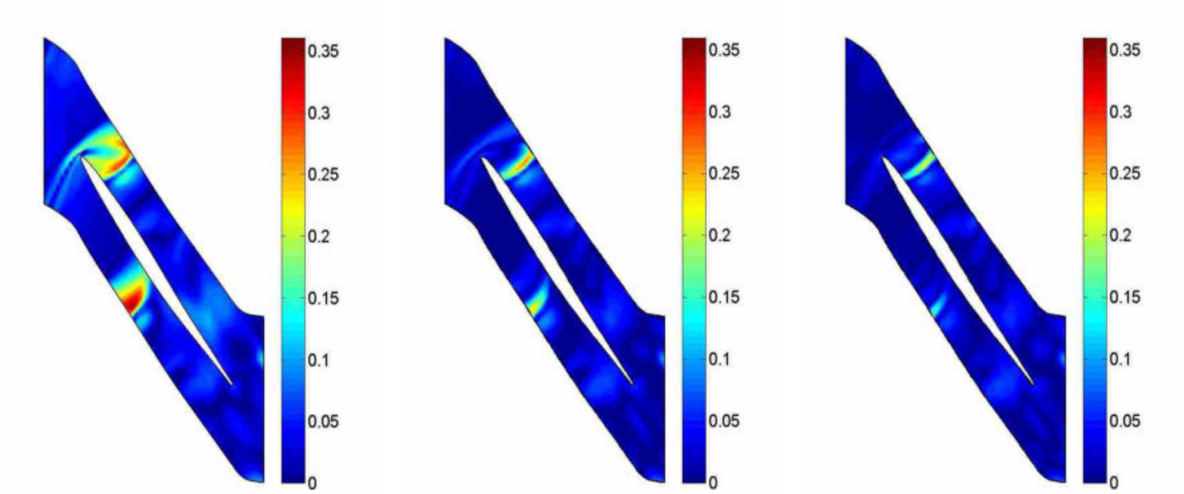

(e) order 1 error (f) order 2 error (g) order 3 error

Figure 4.4: Order 1-3 reconstructions for blade 10, rotor 1 of distorted inlet simulation at design operating condition. The error is calculated by subtracting the reconstruction from the original data.

pressure. The grids for all three rotors are similar in size so it was determined that the difference in POD output stemming from the differences in the grid were minor. As such a qualitative comparison of their relative magnitude may be compared. The modes for all three rotors were also found to contain similar flow features, and because of this, the relative magnitudes were also similar. For these reasons conclusions were made in light of qualitative comparisons of the relative magnitudes of the modes and coefficients in favor exact quantitative comparisons.

The modes are not all presented for the sake of brevity, however, a notworthy comparison is that of mode 3 in rotors 1, 2 and 3 shown in Fig. 4.5. This analysis of shock wave range of motion is also extended later on in the comparison to the near stall simulation data. Generally speaking, the modes look similar, with bands of high magnitude positive and negative values concentrated around the shock region. However, the bands on rotor 3 are noticibly more broad with the high magnitude region spanning 34.0% of the chord length compared to 18.2% in rotor 1. This suggests that the range of motion of the shock wave in rotor 3 is bigger than in rotor 1. Actual measurement of the shock wave range of motion in the original data yielded values of 35.9% and 18.6% for rotor 3 and rotor 1, respectively. It is also observed that the shock wave range of motion is decreased dramatically in rotor 2 followed by a dramatic increase in rotor 3.This confirms not only that the modes are accurate in characterizing the relative change in shock wave motion, but also that the modes may be used as a tool for measuring the range of motion of the shock. Throughout the analysis, the modes were accurate in predicting the range of motion of the shock wave accurate to within 2.5% of the chordlength. This calculation of shock wave range of motion required the observation of only one POD mode, whereas the verification required processing the data from each blade row over the full annulus. This is illustrative of the time and computational expense reductions brought about by working with a reduced order description of the data. The intent of this analysis thus far has been to quantify the ability of POD to extract the above information. A more detailed explanation of the cause of this physical causes of this phenomenon is presented in the near stall comparison.

Coefficients

The coefficients reveal much different information about the similarities and differences in the rotors. Figure 4.6 depicts a comparison of the first order modal coefficients for each rotor. The

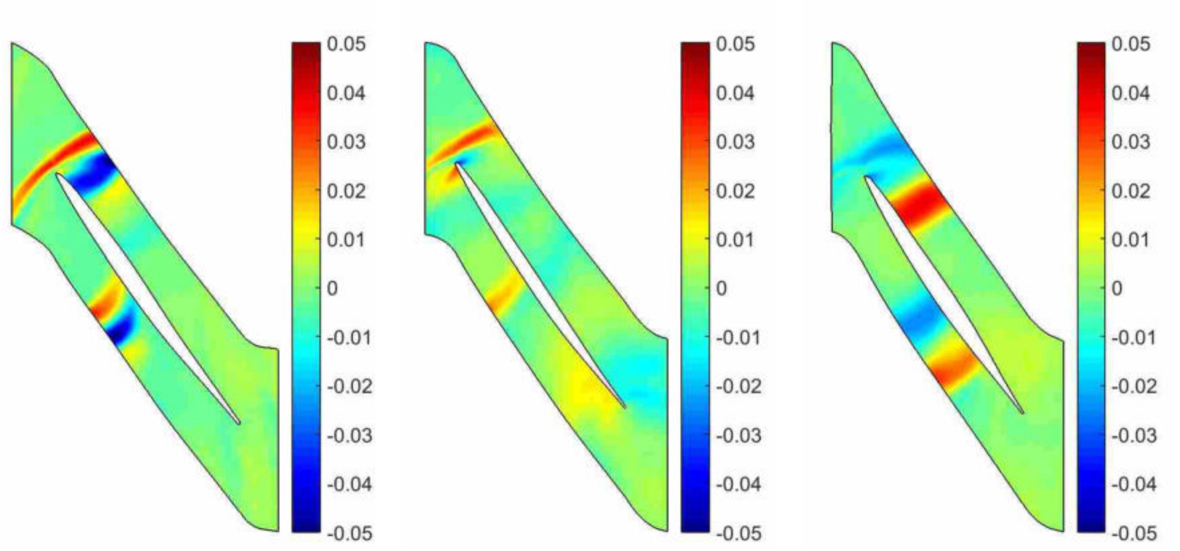

(a) rotor 1, mode 3, banded region near leading edge: 18.2% chordlength

(b) rotor 1, mode 3, banded region near leading edge: 5.3% chordlength

(c) rotor 3, mode 3, banded region near leading edge: 34.0% chordlength

Figure 4.5: Comparison of mode 3 from rotors 1, 2, and 3.

pressure rise through each row can be seen in the magnitude of the coefficients. There are also higher frequency fluctuations present in rotors 2 and 3 due to the blade row interactions.

The standard deviation (SD) can also be used to measure the variation in the data captured by each mode and coefficient vector. While the magnitude of the standard deviation does not have direct physical significance, it is a good metric for distortion amplitude especially when comparing two flow fields. The standard deviation by definition is the statistical measure of the spread of the dataset. Inlet pressure distortion induces circumferential spread in total and static properties. Since the POD modal coefficients describe the circumferential variation on the data, the standard deviation is a way to quantify the effect of distortion on the flow.

Comparison of the standard deviation of each rotor found in the legend of Fig. 4.6 shows that the variation of the average behavior of the flow between rotors 1 and 2 increases, whereas it decreases between rotors 2 and 3. The increase in standard deviation suggests an amplification of the distortion pattern, while the decrease suggests an attenuation of the average distortion pattern. This is consistent with the work of Yao et al. who concluded that this attenuation was a result of the throttling of the exit boundary condition imposed on the simulation [36].

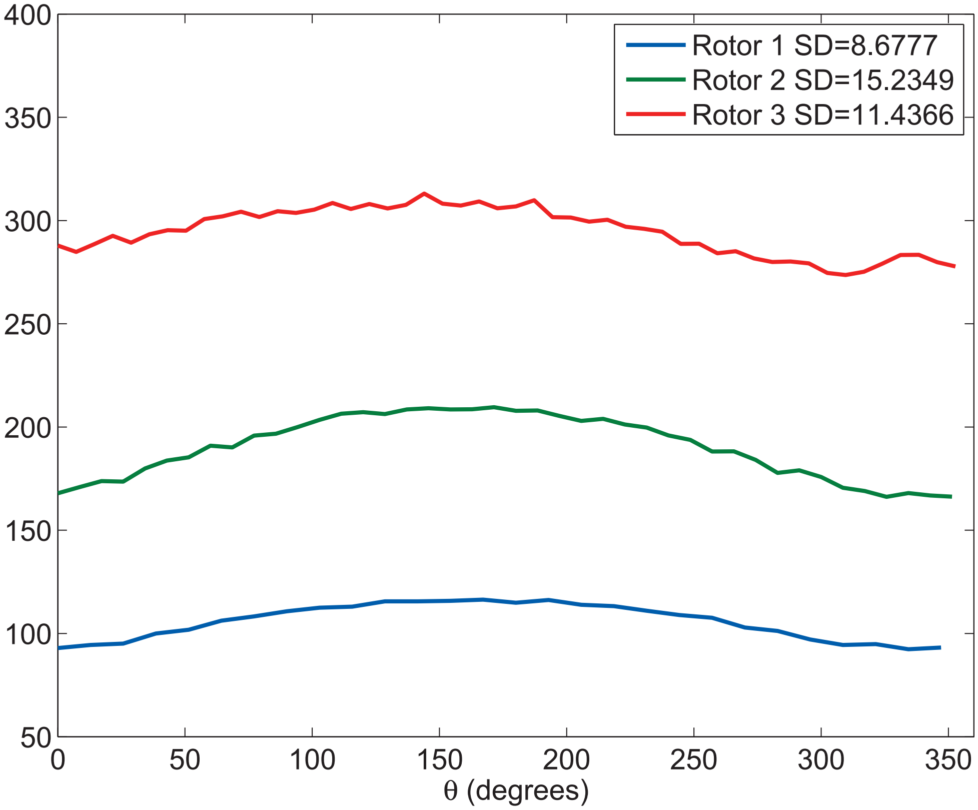

Figure 4.6: Comparison of mode 1 coefficients for all 3 rotors.

Because the standard deviation of the coefficients is a good metric for distortion amplitude comparison, it is a useful tool to investigate the effect exit throttling on the distortion behavior. Comparing the standard deviation of each set of coefficients indicates which mode is affected the most as the blade rotates. Combining that information with the spatial information contained in the modes themselves provides a picture of how the distortion is driving unsteadiness as it travels through the fan.

The standard deviation typically decreases with each modal coefficient set, i.e. the standard deviation of the coefficients for mode 2 is larger than those for mode 3. It is often observed, however, that the standard deviation of mode 1 may be lower than the standard deviation of the higher order modal coefficients. This is because modes *2-n* characterize variation in the data from the mean. Mode 1 has the responsibility of characterizing the mean behavior of the data in addition to a portion of the variation. This can create instances where the portion of variation captured by mode 1 is smaller than the portion captured by mode 2. The singular values however, always decrease.

The coefficient values for modes 2-4 of rotors 1, 2 and 3 are compared in Fig. 4.7. General observations are that the data contains higher frequency content as the rotor number increases. This is likely due to unsteadiness such resulting from blade row interactions and downstream stages ingesting wakes from upstream stages. The standard deviation of each coefficient vector increases as the rotor number increases. This could be caused by either larger variation in the data, or the variations could be spread over a larger area resulting in smaller modal values. In other words, the variation could be spatial within the blade row passage, or it could be more connected to angular location. It is impossible to determine this information from the coefficients alone. This is why it is critical to obverve the modes and coefficients together as has been performed in this research. Observation of mode 2 for the three rotors shows that the spatial structures in this particular mode are small yielding high modal values. This indicates further significance in the magnitude of the coefficients for mode 2 because the large values and standard deviation are magnifying comparatively large modal values. In the case of mode 1 the spatial structures are spread out and relatively small which is why the corresponding modal coefficients are so large to compensate for this spread. The standard deviation also increases with each rotor suggesting distortion amplification.

As stated above that it was possible for the standard devation of mode 2 to be higher than mode 1, this is indeed the case with rotor 3. This can be seen by comparing the standard deviation values for rotor 3 from Fig. 4.6 and Fig. 4.7. The standard deviation value of 17 is higher than the standard devation for mode 1 as well as mode 1 from rotor 2. Observations on the coefficient values such as standard deviation show the effect of distortion changes between rotor two and rotor three. The standard deviation of the coefficients for rotor two indicate mode one is dominant which characterizes shock amplitude. The standard deviation of the coefficient values for rotor 3 indicate mode two is dominant which characterizes shock range of motion. The coefficients then make it possible to observe how distortion effects the blade row by indicating what mode is dominant. The flow features characterized by the dominant mode are the flow aspects most profoundly impacted by the conditions under investigation. This example also illustrates the value of working with extracted components. The modal coefficients associated with rotor 3 suggest that

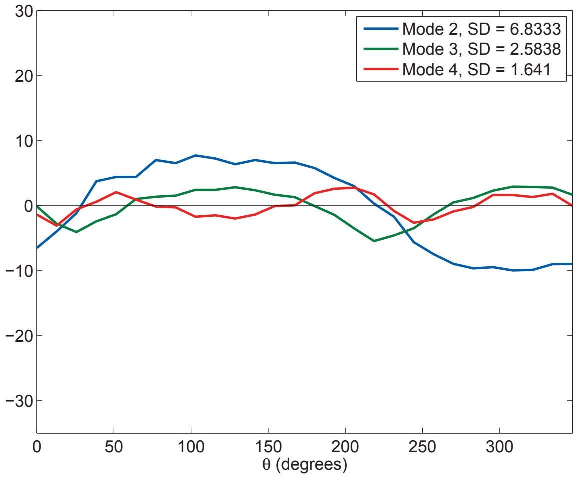

(a) rotor 1

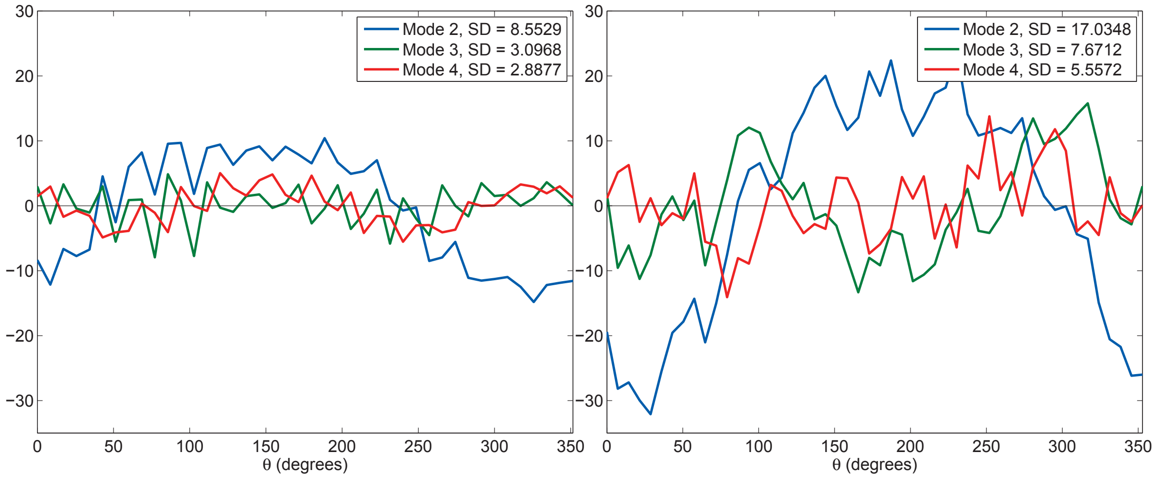

(b) rotor 2 (c) rotor 3

Figure 4.7: Comparison of modal coefficients 2-4 for all three rotors.

mode 2 describes where the majority of the distortion effects are captured, and the corresponding mode 2 reveals that the distortion is most influencing the location of the shock wave.

A bar plot containing the standard deviation values for each mode of rotors 1-3 are shown in Fig. 4.8. Observation of the standard deviation of the mode 1 coefficients shows that the mean pressure oscillation is amplified between rotor 1 and 2 but decreases between 2 and 3. This is the same phenomenon described above. The mode 2 coefficients show a slight increase between rotors 1 and 2, and a large increase between 2 and 3. Combining this information with the fact that the shock wave range of motion increases dramatically in rotor 3 shows how the distortion information

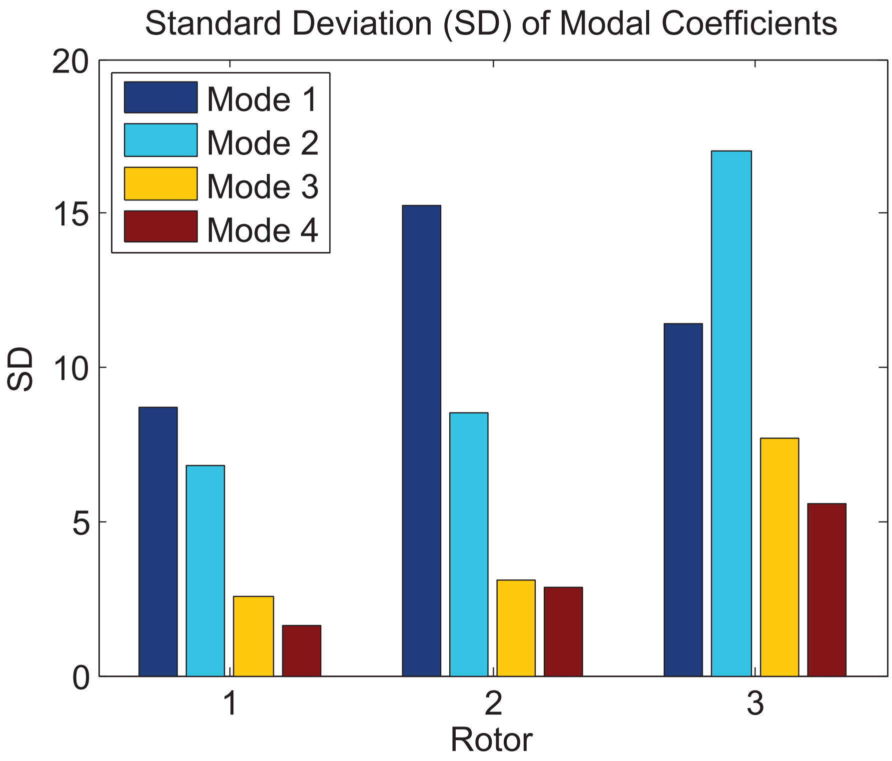

Figure 4.8: Comparison of modal coefficient standard deviation (SD) for all three rotors.

is being transferred from mean pressure field oscillations to shock wave range of motion. In other words, since the variation in the mean pressure field was attenuated due the throttling exit condition as discussed above [36], the distortion must manifest itself in the next dominant flow phenomenon, which is shock wave oscillation. The throttling of the exit boundary condition then minimizes the effect of inlet distortion on the mean pressure field. The standard deviation then drops dramatically in the coefficients for modes 3 and 4. Modes 3 and 4 also contain structures describing the location of the shock wave and characterizing higher order fluctuations. The standard deviation for these modal coefficients also increases significantly in rotor 3 reinforcing the same conclusions.

4.1.5 Rotor 1, Clean Inlet at Design

For the purposes of comparison, a similar analysis was performed on simulation results from the same rig with clean total pressure inlet flow at design operating condition. The modes are shown in Fig. 4.9. It is immediately apparent that these modes look very different from their distorted counterparts. Mode 1 from the clean case looks similar to mode 1 from the distorted case (Fig. 4.1a) suggesting that the mean spatial behavior of the two flows is similar. However, the shockwave feature represented in mode 1 looks much sharper compared to the shockwave captured by mode 1 in the distorted case. This is because the shock wave moves much less in the clean case (0.786% chordlength for clean compared to 18.8% for distorted) so the average behavior has a much smaller range. Modes 2, 3 and 4 do not appear similar at all to the corresponding distorted modes (Figs. 4.1b-4.1d). The clean modes do not have distinct areas of zero magnitude and high values are not concentrated around a distinguishable feature such as a bow shock but seem to be spread throughout to capture more minor fluctuations in the flow as the blade rotates.

Coefficients and Singular Values.

The associated modal coefficients are plotted in Fig. 4.10. As expected, the coefficient values are very flat with the absence of the 1/rev distortion pattern. The calculation of the standard deviation (reported in the figure) reveals very small variation compared to the distorted case. Mode 1 for the clean case is close in magnitude to the distorted case (Fig. 4.2). It is also noted that the standard deviation for the mode 2 coefficients is larger than the standard deviation for mode 1. This is another example of the first mode capturing a smaller portion of the variance, but still contributing the most information by carrying the mean values of the data. This is reflected in the singular values which are plotted in Fig. 4.11. Upon comparison with the distorted case (Fig. 4.3) reveals that the singular values associated with the clean case are of much smaller magnitude after the first value. This is because there is so little variation in the data. Almost all of the information contained in the data can be carried by the first mode and its associated coefficients. This can be readily observed in the first order reconstruction.

Reconstructions.

The first order reconstruction shown in Fig. 4.12 demonstrates the effectiveness of mode 1 at reproducing the data to a high accuracy. This is because the data contains very little variation from the mean so higher order modes do not contribute significant information. Higher order reconstructions do not add much to the data, and reduce the error by very little. Comparison of

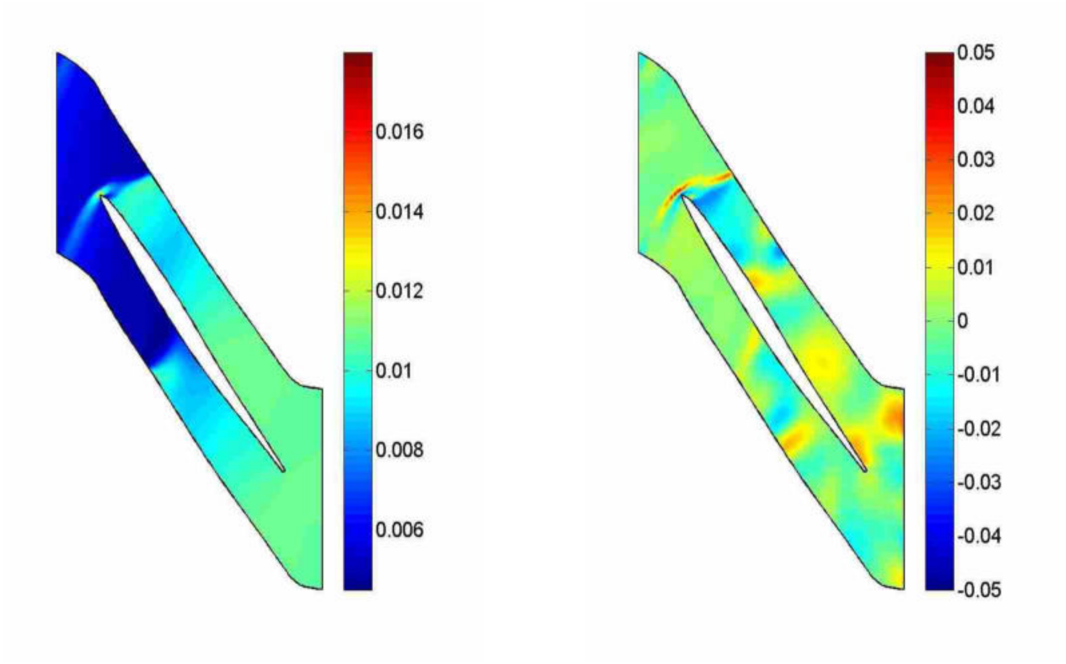

(a) mode 1

(b) mode 2

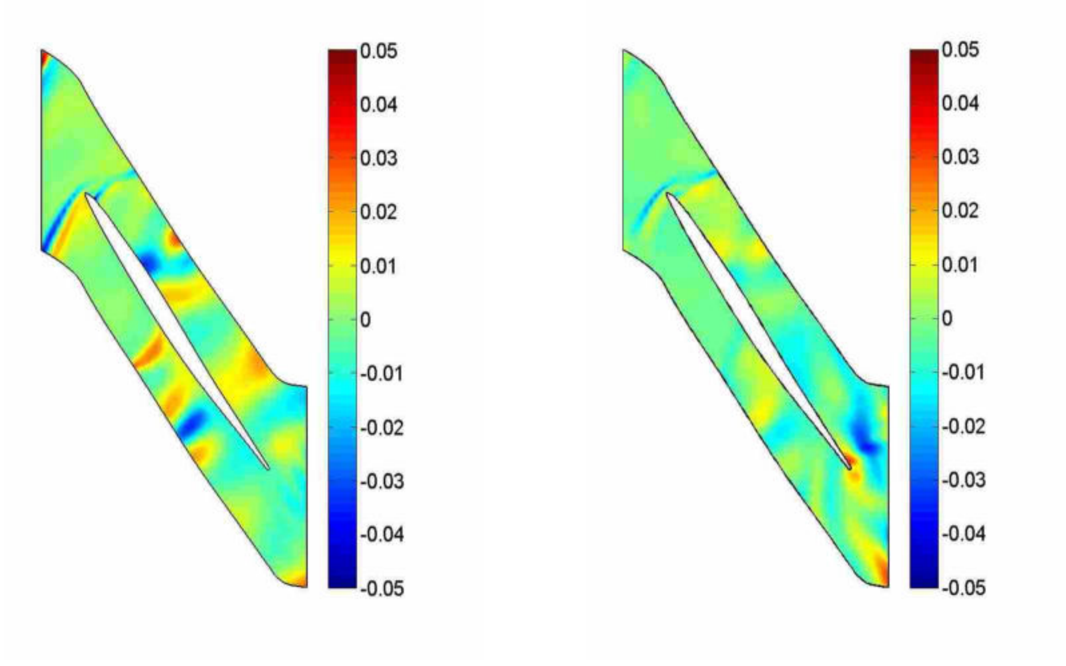

(c) mode 3

(d) mode 4

Figure 4.9: POD modes 1-4 from clean inlet at design operating condition, rotor 1, static pressure.

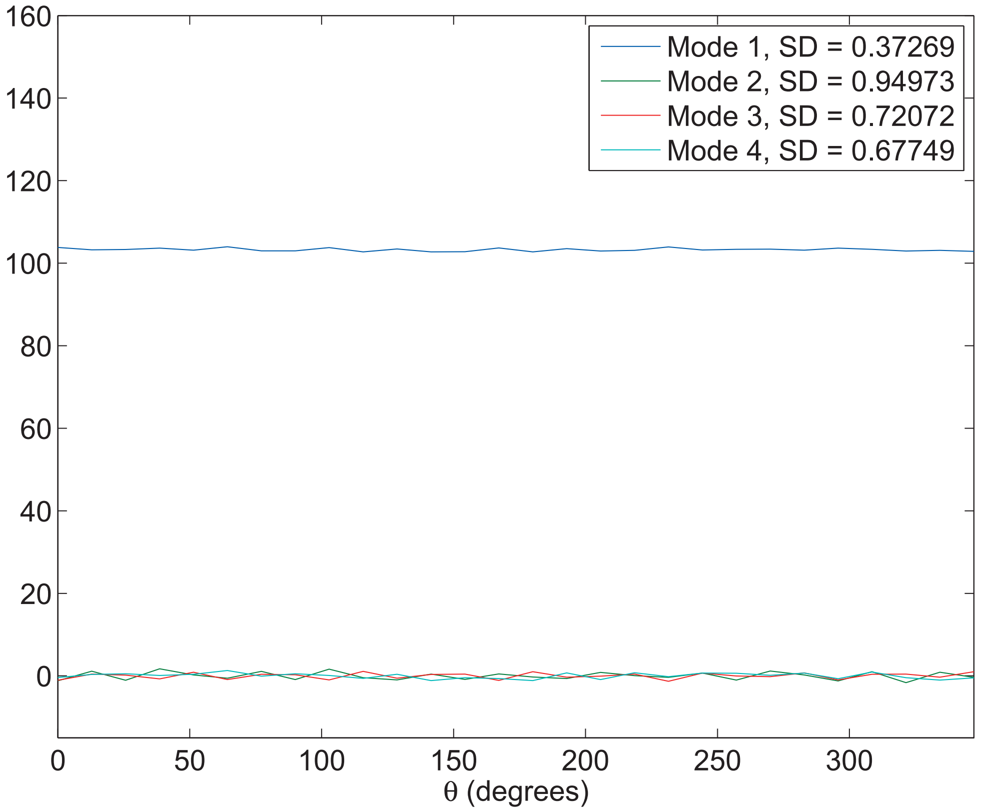

Figure 4.10: POD modal coefficient values associated with modes 1-4 and corresponding standard deviation (SD).

Fig. 4.12 to Fig. 4.4 shows that the first order reconstruction of the clean data has a much lower error than even the third order reconstruction. Observation of Fig. 4.12c shows that there is a small area of higher error around the region of the shock wave but that for the most part the error is spread relatively uniformly throughout the domain. The error is not concentrated around a particular feature as profoundly as in the distorted case because the flow features are mostly stationary in a clean inlet flowfield.

4.1.6 Rotor Comparison, Clean Inlet at Design

Modes.

Comparison of the modes for rotors 1, 2 and 3 for the clean simulation yields a different conclusion than the rotor comparison for the distorted case. Mode 1 for rotors 2 and 3 (not shown) look similar to mode 1 for rotor 1 (shown in Fig. 4.9) as they capture the mean behavior. However,

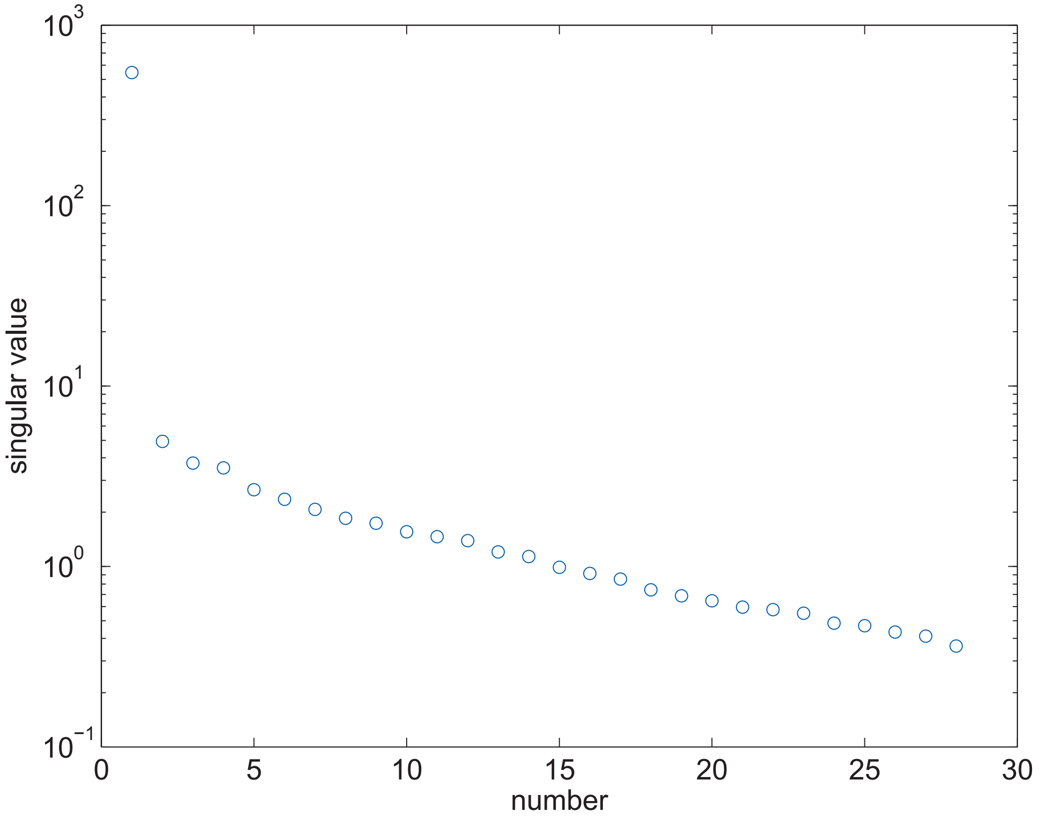

Figure 4.11: POD singular values.

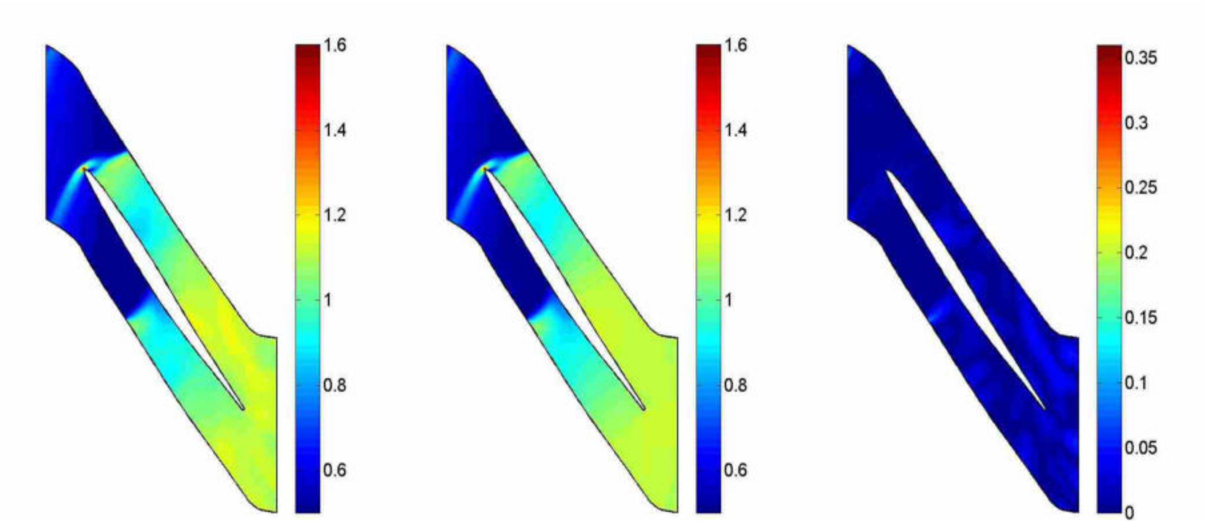

(a) original (b) reconstruction (c) error

Figure 4.12: Order 1 reconstruction for blade 10, rotor 1 of clean inlet simulation at design operating condition.

modes 2, 3 and 4 differ in rotors 2 and 3 from rotor 1. As the flow passes rotor 1, the subsequent blade row interactions and wake ingestion induce variations in the flow. This creates motion in the bow shock. Because of this new variation, modes 2, 3 and 4 shift their responsibility to characterizing this shock wave motion. This phenomenon can be observed in the comparison of mode 2 from rotors 1 and 3 shown in Fig. 4.13. The minor fluctuations previously captured by modes 2, 3 and 4 are then shifted to later modes. This phenomenon also causes the corresponding singular values to increase indicating that the modes are capuring more variation.

In the case of rotors 2 and 3, the modes begin to look very similar to the distorted case with a concentration of high magnitude values in a banded region around the shock wave. An example of this is illustrated in Fig. 4.13 where mode 2 from rotors 1 and 3 are compared. The mode for rotor 1 only captures minor perturbations where as for rotor 3 there is a clear emphasis on the shock. The corresponding widths of the banded regions of these modes are 2.29%, 1.95%, and 3.78% chordlength for rotors 1, 2, and 3, respectively. The modes suggest the creation of motion in the bow shock as the flow progresses. The actual motion of the shock for this scenario as measured from the simulation data is 0.76%, 1.95% and 5.09% chordlength for rotors 1, 2, and 3, respectively. The POD modes in this situation predicted the motion of the shock wave to within 2% of the chordlength, however at these scales the relative error is large. The corresponding singular values for these modes are 4.93 for rotor 1, 30.48 for rotor 2, and 42.5 for rotor 3. This is an indication that mode 2 also carries much more information for rotors 2 and 3 than it does for rotor 1. This can also be seen in the modes themselves where the shock structure is much more defined for rotors 2 and 3 than for 1. This may also account for the large discrepancy in the modal prediction and the actual range of motion for rotor 1. The shock structure is not well defined so it is difficult to quantify the width of a region that is not as well defined as those in rotors 2 and 3.

Coefficients.

While the modes for rotors 2 and 3 begin to look similar to the distorted case, the difference between the two flows is shown in the absence of the 1/rev distortion pattern in the coefficients of the clean case. This can be seen in the comparison of the coefficients associated with mode 1 shown in Fig. 4.14. The 1/rev distortion pattern is clearly absent and the data contains higher frequency content as the rotor number increases, suggesting blade row interactions. Modes 2, 3 and 4 are

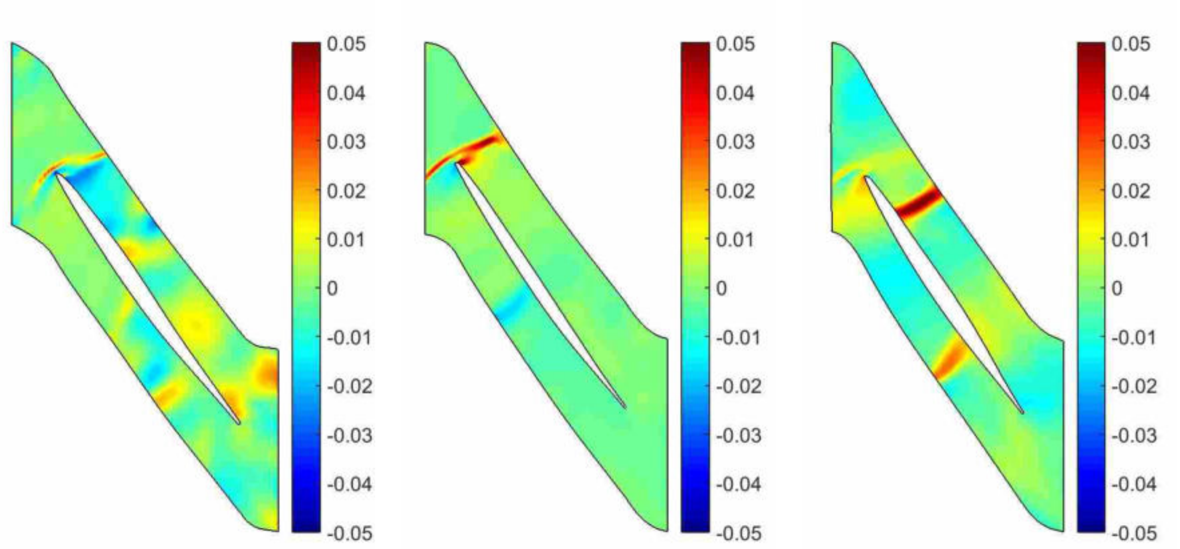

(a) rotor 1, mode 2: σ=4.93, width of banded region at leading edge: 2.29% chordlength

(b) rotor 1, mode 2: σ=30.5, width of banded region at leading edge: 1.95% chordlength

(c) rotor 3, mode 2: σ=42.5, width of banded region near leading edge: 5.09% chordlength

Figure 4.13: Comparison of mode 2 from rotors 1, 2 and 3. Clean inlet at design operating condition.

plotted in Fig. 4.15. As can be seen the variation in the data increases significantly with each rotor. The modes for rotors 2 and 3 characterize shock wave motion, so it can be concluded that the blade row interactions induce some oscilation to the shock waves. However, these oscillations are high frequency compared to the 1/rev distortion pattern.

4.1.7 Near Stall Comparison

The analysis of static pressure performed above on design operating condition simulation data was also performed for the near stall operating condition. This section contains analysis comparing the two. A great deal of insight can be gained about the differences between design and near stall by observing the higher order modes. Higher order modes characterize deviations from the mean behavior such as structures moving spatially or changing in amplitude. Mode 2 for the three rotors at design and near stall operating condition is shown in Fig. 4.16 The columns in the figure correspond to the rotors, and rows 1 and 2 correspond to design and near stall operating condition, respectively. Mode 2 always depicts the flow features that are varying the most. In

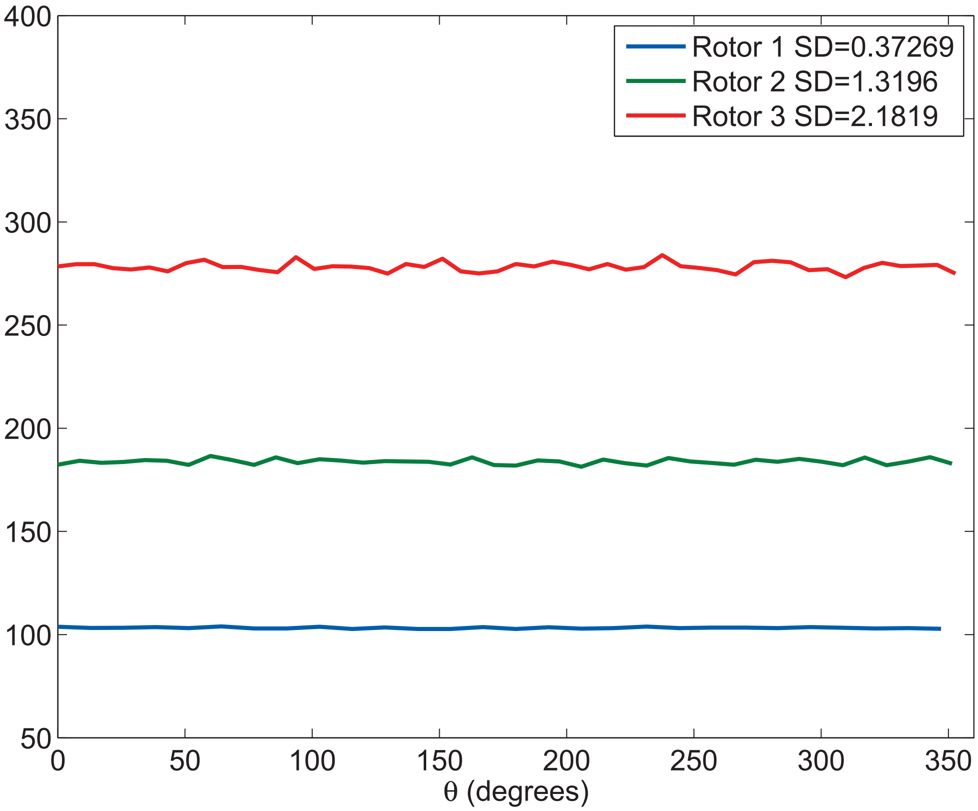

Figure 4.14: Comparison of mode 1 coefficients for all three rotors.

the case of all of these situations the motion of the shock front is the most dynamic feature. For these particular datasets, the main structure shown in the mode is a wide banded region in the area where the shock wave resides through the rotation of the fan. The banded region tells us generally where the shock resides, and also provides limits on the fore and aft positions of the shock when the blade is in the low and high pressure extremes from the distorted inlet condition. The banded region contained in mode 2 is marked in Fig. 4.16 by two red asterisks denoting the extremes in the range of motion.

Several trends are noticed when the differences between design and near stall are observed. First, as is expected the location of the shock wave is pushed farther upstream in the near stall case. This is because of the increase in back pressure associated with the near stall operating condition. In these simulations, the inlet boundary condition stays the same, and so the fan is pushed to near stall by increasing the back pressure, and thus increasing the overall pressure ratio for the fan. This in turn causes the shock front to be pushed forward. The second observation is that the range

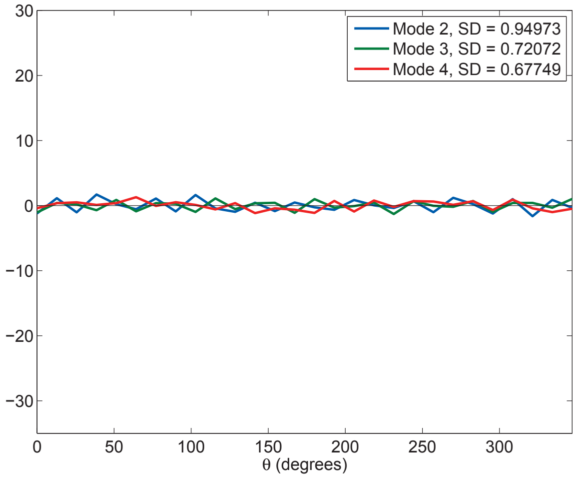

(a) rotor 1

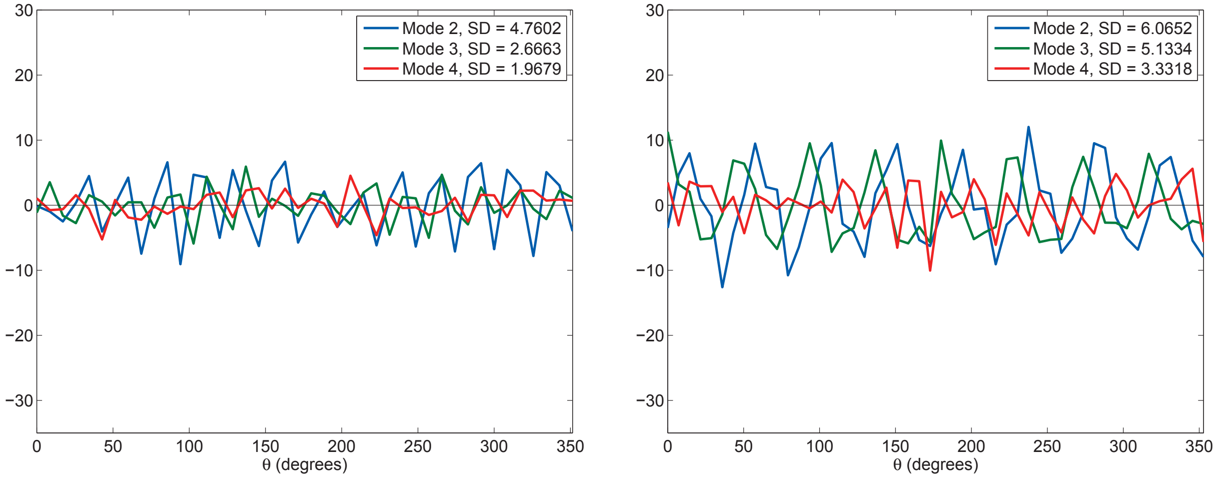

(b) rotor 2

(c) rotor 3

Figure 4.15: Comparison of modal coefficients 2-4 for all three rotors.

of motion of the shock wave is decreased significantly in the near stall case. In both design and near stall, the range of motion increases from rotors 1 to 3 (Figs. 4.16a and 4.16c for design and Figs. 4.16d and 4.16f for near stall). It also increases from rotor2 to 3 in both cases. In the case of rotor 1 to 2, the range of motion increases slightly in the near stall case and decreases in the design case.

An explanation for the cause of this phenomenon can be found in the differences between the flow physics for each case. Weston describes the behavior of the shock waves by describing how the total pressure distortion varies the pressure ratio of the fan at different circumferential

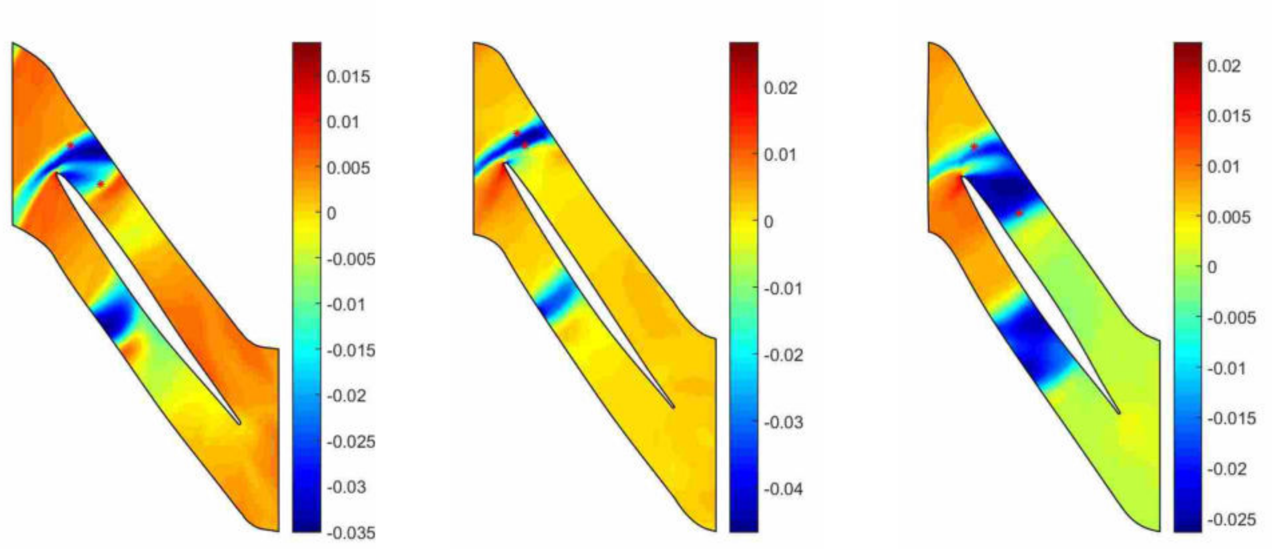

(a) Design–Rotor 1.

(b) Design–Rotor 2.

(c) Design–Rotor 3.

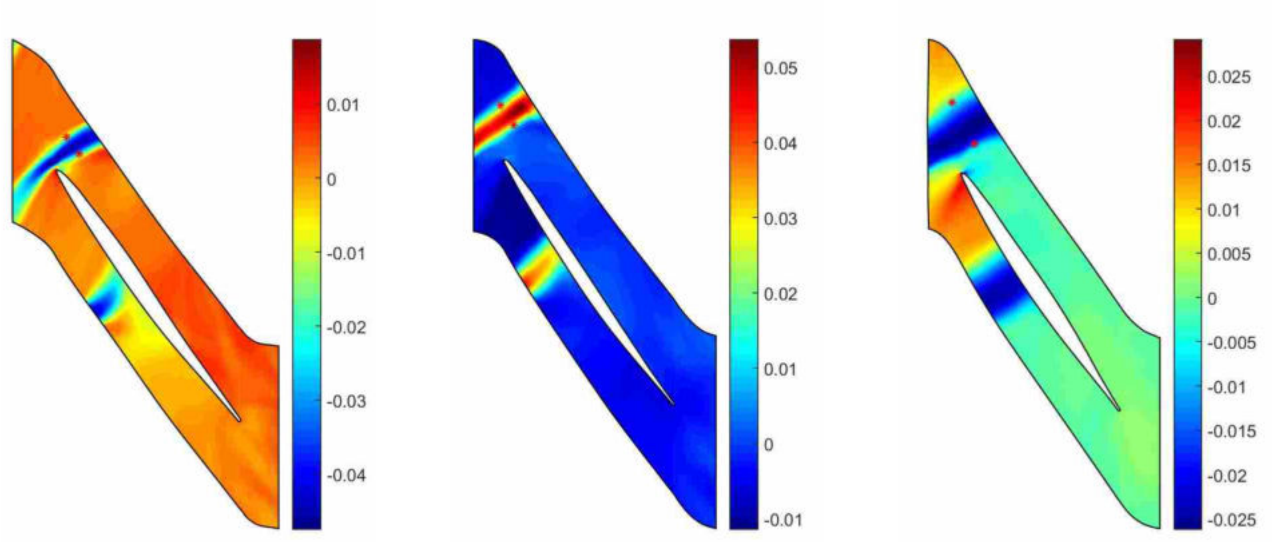

(d) Near Stall–Rotor 1.

(e) Near Stall–Rotor 2.

(f) Near Stall–Rotor 3.

Figure 4.16: Static pressure POD mode 2 from distorted inlet at design and near stall operating condition for rotors 1-3.

locations. This in turn changes the location of the shock wave in the blade row passage [1]. The induced static pressure gradients from the total pressure distortion are what push the shock up and down stream. In the near stall case the back pressure is increased. This pushes the shock wave further up the blade row passage. The pressure gradients are still present but their effect is lessened due to the higher back pressure. Thus the shock wave still oscillates but with a smaller range of motion. An additional explanation for the compressed range of motion in the near stall case is that the aft position of the range of motion is pushed forward due to the back pressure condition from being in near stall. The fore position is limited in how far forward it can travel before stall is induced. Thus in the near stall condition the effects of distortion are lessened and this leads to less circumferential variation in the operating condition.

Validation of the behavior suggested by mode 2 with the actual behavior was also calculated. The red stars fore and aft of the banded region in Fig. 4.16 represent the measured values of the range of motion based on the values of the pressure derivative along the gridline. The location of the highest derivative value was the assumed location of the shock wave, or in the case of a POD mode, the location of the fore or aft extreme position of the shock in its circumferential range of motion. A comparison of the predicted range of motion for each mode with the actual range of motion is shown in Fig. 4.17. The case of rotor 3 for the near stall condition where a bar is missing indicates that the mode was capturing a different flow structure and so was not applicable to the comparison. It can be seen that there are varying levels of accuracy depending on the mode used to estimate the range of motion. It is noted that none of the modes ever overestimate the range of motion, and for all cases there is a mode capable of estimating the range of motion to within a few percent. It is the authors recommendation that a researcher using this type of analysis for their own work would pick the mode indicating the largest range of motion for the most accurate results in estimating the actual behavior.

4.2 Axial Velocity

4.2.1 Modal Analysis

Static pressure is well suited to identify and characterize the location and motion of the passage shock. However, there are additional features in the flow which static pressure is incapable

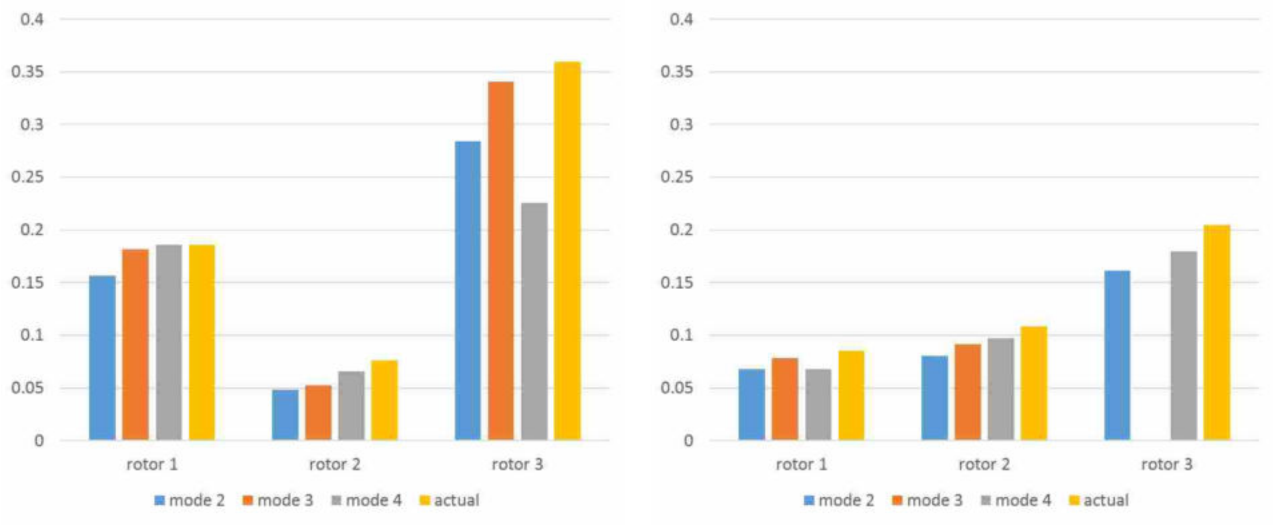

(a) Design.

(b) Near Stall.

Figure 4.17: Comparison of estimated and actual shock wave range of motion (% chordlength) for design and near stall operating condition.

of identifying. Axial velocity is an ideal candidate to reveal additional flow dynamics which are not present in the static pressure flow field. Axial velocity was chosen to investigate boundary layer and wake behavior in these flows. Although it was determined that the boundary layers are too thin for POD to identify, it was found that the analysis of axial velocity reveals the presence of a separation region. Other parameters such as static temperature and total properties will also identify additional behavior, but axial velocity seemed a natural choice for analysis since the inherent physics of wake structures involve momentum deficit.

Figure 4.18 contains a rotor comparison of modes 1 and 2 of the POD of axial velocity through the fan at design operating condition. The primary flow features contained in these modes are a shock structure similar to those contained in the static pressure modes, and a wake-like structure on the low pressure surface and trailing edge. This is a flow separation region. This structure is not present in the static pressure modes due to the physics of the structure. It is a momentum deficit, with uniform static pressure. Figure 4.19 contains a rotor comparison of modes 1 and 2 of the POD axial velocity through the fan for the near stall condition. It is observed that the phenomonon is similar in the near stall case with the same wake-like structure on the low pressure surface and trailing edge.

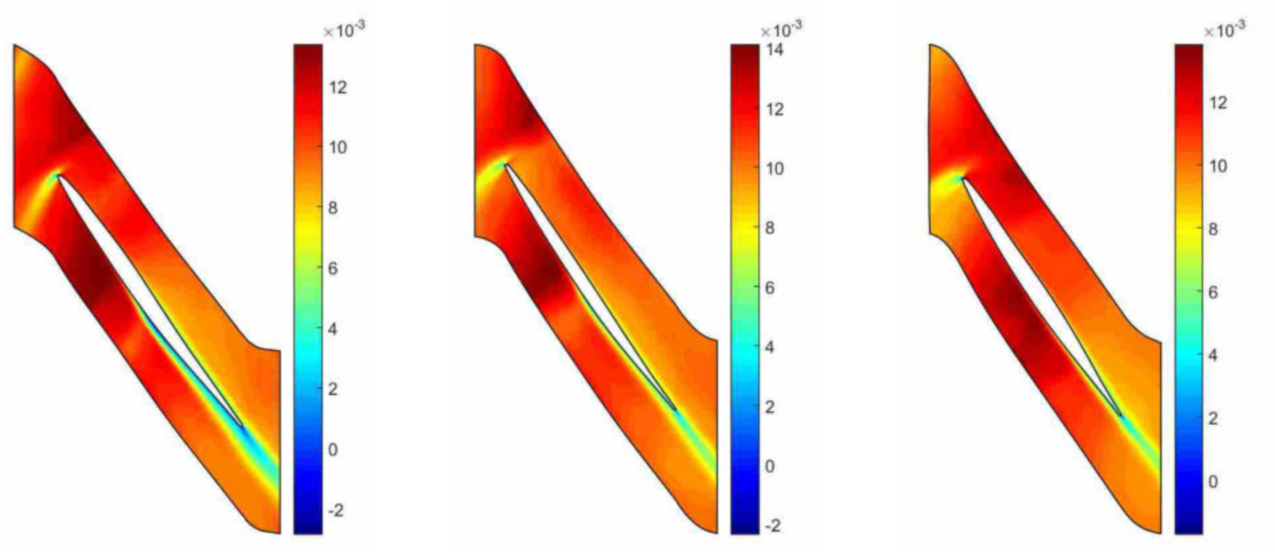

(a) Rotor 1–Mode 1. (b) Rotor 2–Mode 1. (c) Rotor 3–Mode 1.

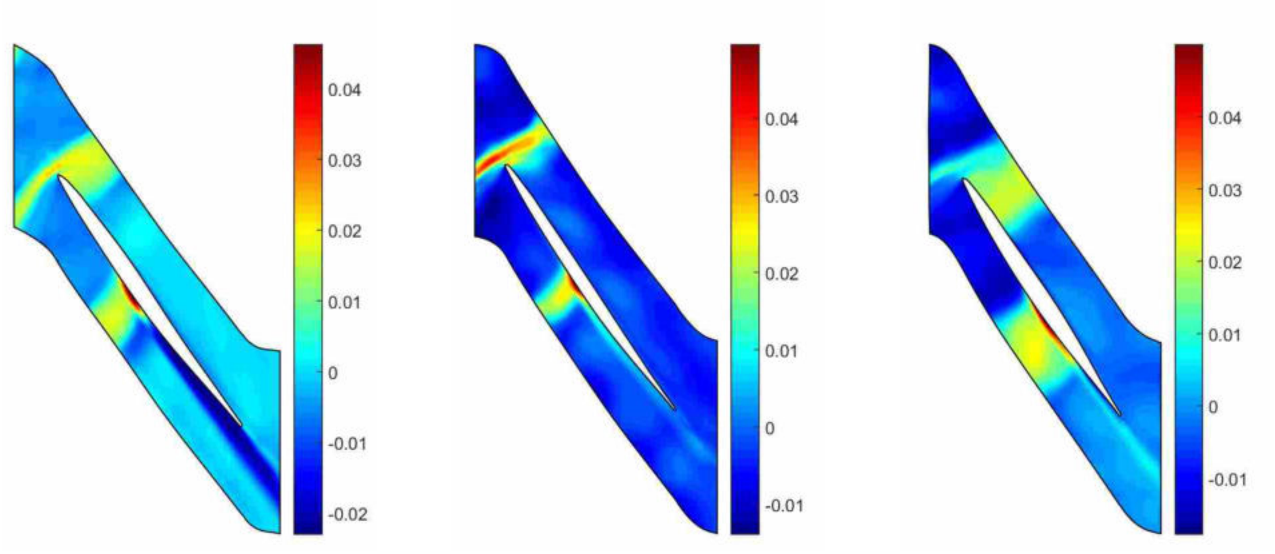

(d) Rotor 1–Mode 2. (e) Rotor 2–Mode 2. (f) Rotor 3–Mode 2.

Figure 4.18: Axial velocity POD modes 1 and 2 from distorted inlet at design operating condition for rotors 1-3.

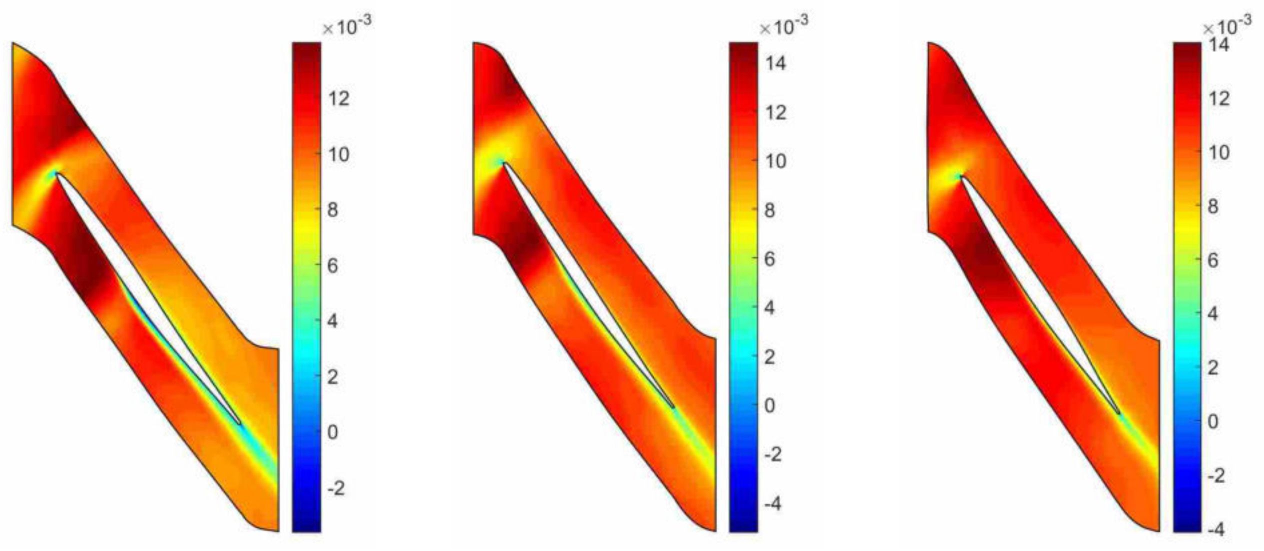

(a) Rotor 1–Mode 1.
(b) Rotor 2–Mode 1.
(c) Rotor 3–Mode 1.

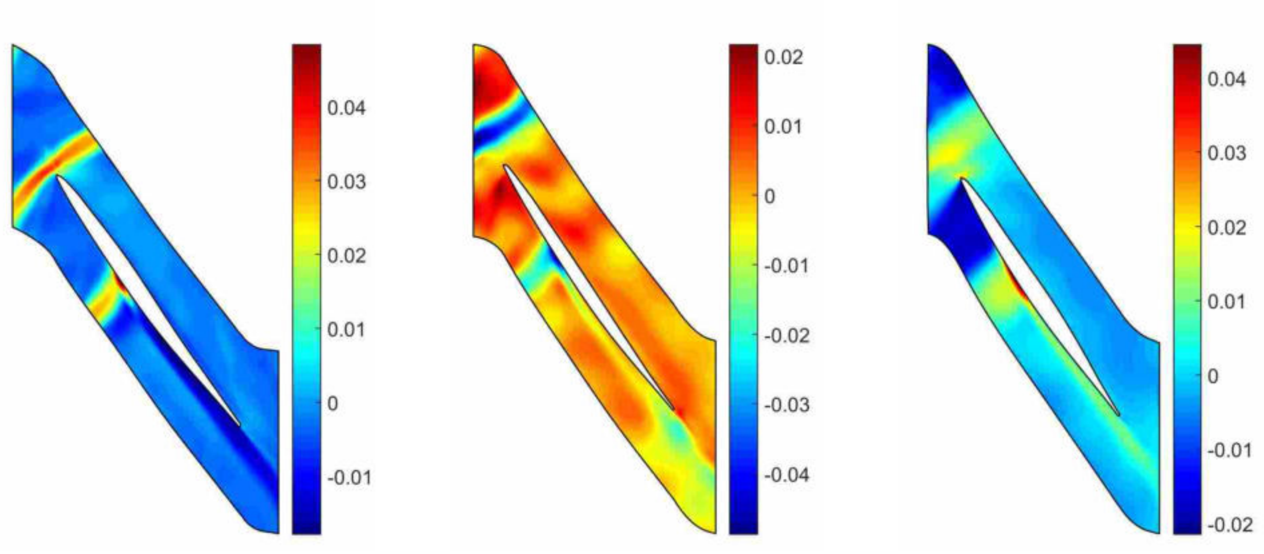

(d) Rotor 1–Mode 2.
(e) Rotor 2–Mode 2.
(f) Rotor 3–Mode 2.

Figure 4.19: Axial velocity POD modes 1 and 2 from distorted inlet at near stall operating condition for rotors 1-3.

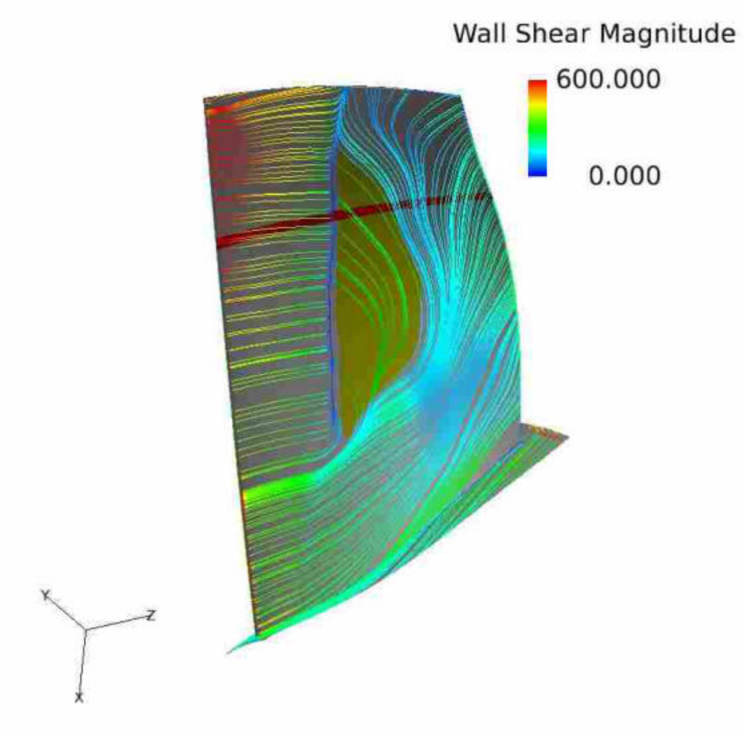

Figure 4.20: Streamlines of wallshear magnitude illustrating separation point at rotor 1. The yellow highlighted region corresponds to a separation bubble.

In order to verify that the structure is truly a separation region, the data for the full span of the blade was post-processed using FieldView. The results of this postprocessing analysis are shown in Fig. 4.20. The surface of the blade shown is the low pressure surface, corresponding to the bottom surface on the 2 dimensional figures. The direction of rotation is into the page. The bold red line represents the slice taken at 30% immersion which corresponds to the 2 dimensional data in the blade passage figures for rotor 1 for the modes and simulation data. The thinner lines are streamlines which are seeded uniformly at the leading edge of the blade. The color contours represent the magnitude of the wall shear stress. As can be seen the streamlines proceed uniformly in the axial direction until roughly 40% of the chord at which point they coalesce into a well defined line traveling in the radial direction. This line corresponds to the location of the passage shock. At this point the color of the streamlines abruptly turns to dark blue which is zero on the color scale. The coalescance of the streamlines in this fashion coupled with the magnitude of the shear stress transitioning rapidly to zero indicates a separation line. There is then an arrowhead shaped region where the streamlines are sparce which corresponds to a separation bubble. This arrowhead shaped region is marked in the figure as the yellow highlighted region. Finally at about 65% chord the streamlines fan out again indicating reattachment. The shear stress is still at relatively low magnitude at the exit compared to the incoming flow. Upon verification that the flow was indeed separated via the above analysis, an interpretation of the modes could be perfomed with this information in mind.

The modes contained in Fig. 4.18 illustrate that the separated structure is much more pronounced in rotor 1 (Figs. 4.18a and Fig. 4.18d) than in rotors 2 and 3. The structure in rotor 1 is both larger and of a higher magnitude. The presence of this feature in mode 2 for the three rotors indicates that this is a dynamic structure. In other words the location of the structure and/or the magnitude of its velocities changes circumferentially. The magnitude of the modal values surrounding a structure are commensurate with the magnitude of the variation of the structure. For example, the structure in mode 2 of rotor 1 (Figs. 4.18a and Fig. 4.18d) contains values close to the maximum in that mode whereas in rotors 2 and 3 the maximum values are concentrated more around the shock wave and the separation region contains values of a smaller magnitude. For rotors 2 and 3 modes 3 and 4 (not shown) contain no separation structure whereas rotor 1 modes 3 and 4 still contain the separation structure. The fact that the structure maintains a presence in the higher order modes indicates it is a highly dynamic structure.

In rotor 1, the separation region is present in mode 2 for both design and near stall. It is not present in any of the higher order modes for the clean simulations at any operating point. This is because the higher order modes contain dynamic structures. When there is no inlet distortion as in the clean simulation, the separation structure is present but does not change in size or magnitude. Thus the separation structure is not caused by the distortion, however it is influenced by the distortion just as the location of the shockwave is. A closer look at mode 2 of rotor 1 (Fig. 4.19d) for the distorted case at design shows a separation region approximately 48% wider than the separation region in mode 1 (Fig. 4.19a). This indicates that the separation structure is changing in size. The separation structure is also behind the banded shock region. This is because the separation region always begins at the location of the passage shock. This suggests a causal relationship between the shock wave and the separated region. The shock trips a separated region on the downstream surface of the blade. It is difficult to discern from the modes and coefficients alone the exact circumferential behavior of this separated structure. In order to gain more insight, the original data must

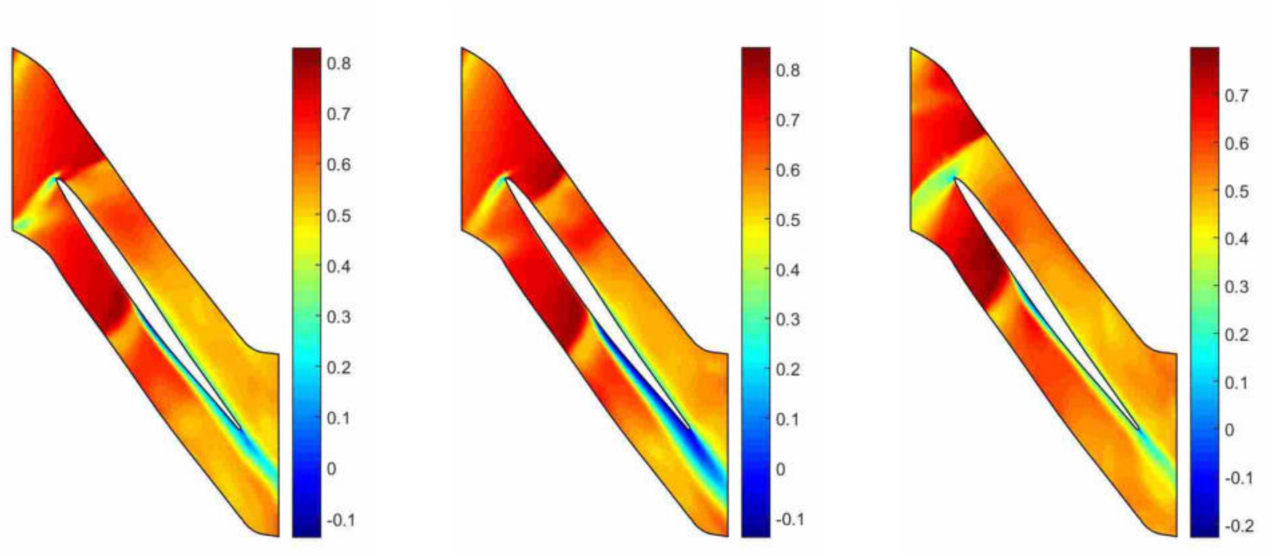

(a) Clean.

(b) Distorted–high pressure zone. Separation zone 74% larger than the clean condition at the trailing edge of the blade.

(c) Distorted–low pressure zone. Separation zone 33% smaller than the clean condition at the trailing edge of the blade.

Figure 4.21: Comparison of simulation data for clean and distorted inlets at design operating condition.

be investigated. POD is useful for a preliminary analysis to point the investigator in the direction of the most dynamic structures and to give a general idea of their behavior. With this preliminary information in mind, more specific information may be sought.

Figure 4.21 provides a comparison of the distorted inlet data at design operating condition at two circumferential locations along with a comparison to the clean data. Figure 4.21a contains clean data at an arbitrary circumferential location (there is minimal circumferential variation). Figures 4.21b and 4.21c contain distorted data from the circumferential locations where the separation region is the thickest and thinnest, respectively. These circumferential locations are 180 degrees opposite each other. The separation region is thickest (approximately 74% larger than the separation region under clean conditions) in the high pressure portion of the flow when the shock wave is pushed further downstream. The separation region is thinnest (33% smaller than that for the clean inlet condition) in the low pressure portion of the flow when the shock wave is further upstream. The thickness of the separation region is determined by the strength of the shock wave. Shock wave strength is defined in Eqn. 4.1, where Δp is defined as the static pressure jump across the shock and $\overline{p}$ is defined as the average of the maximum and minimum static pressures. When the shock is located further downstream the shock is stronger (Shock Strength = 0.7452) which causes a more pronounced interaction between the shock and the boundary layer, and thus a thicker separated region. The weaker shock located upstream (Shock Strength = 0.5353) produces a comparitavely minor interaction and thus a thinner separated region.

$$Shock\ Strength = \frac{\Delta p}{\overline{p}} \tag{4.1}$$

The phenomenon of flow separation which is induced by the shock wave comes from the shock wave boundary layer interaction. This is a common phenomenon in turbomachinery. Hilgenfeld et al. [53] performed experimental and numerical investigations on shock wave boundary layer interactions on a highly loaded transonic compressor cascade. They studied shock wave/laminar boundary layer interactions. Their study is related to this research in the sense that the compressor used in this research is also transonic. They found that the "emerging shock system interacts with the laminar boundary layer, causing shock-induced separation with a turbulent reattachment." The phenomenon observed by Hilgenfeld et al. is very similar to the physical behavior occuring in this research.

The analysis of shockwave turbulent boundary layer interaction has also been studied by Grilli et al. [25]. This analysis uses DMD as a tool for analysis. They find the presence of a low frequency mode associated with pulsation of the separation bubble, accompanied by forward and backward motion of the shock. This phenomenon is also consistent with the physics observed above. The thickness of the separated region identified on the low pressure surface of the blade oscillates in shape according to the forward and backward motion of the shock wave as well. Gaitonde [54] also describes similar physics regarding the "phenomenology of low frequency unsteadiness".

Michelassi [55] also studied shock boundary layer interaction in a turbine linear cascade using a Navier-Stokes solver. It was found that in the flow over the turbine blade the shock wave induced a flow separation. This flow separation was found to affect the boundary layer development. The model used was found to predict the separation point. This is another example of flow separation induced by a shock wave/boundary layer interaction.

4.2.2 Near Stall Comparison

The near stall operating condition produces a qualitative result similar to Fig. 4.21. Quantitatively the near stall condition produces a thinner separated region in the high pressure portion of the flow. At design operating condition when the blade enters the high pressure zone the separation region thickens to 74% larger than the separation region under clean conditions. This is more than the near stall condition where the separation region is 15% thinner than the design condition. In other words, the near stall operating condition thins out the separated region at the trailing edge of the blade in the high pressure zone. This is because the shock is pushed further upstream in the near stall condition due to the higher back pressure causing a weaker shock and a less pronounced interaction between the shock and the separated region.

In the low pressure zone, both design and near-stall operating conditions yield a separation zone that is the same thickness. Further investigation as to the reason for this produced the observation that the shock waves are in the same position for both design and near stall. Since it is the position of the shockwave that determines the thickness of the separation region that is why they are the same thickness. Inspection of Fig. 4.16a and 4.16d will reveal that the farthest forward position of the shock wave is the same for both design and near stall operating conditions. This can be seen by observing the position of the red asterisk furthest upstream in the figure. This marks the position of the extremes of the range of motion of the shock wave. This particular behavior where the shock waves are in the same position at the farthest forward position is only observed in rotor 1.

4.2.3 Clean Comparison

Mode 1 for the clean condition at design operating condition is shown in Fig. 4.22a. A comparison between clean and distorted inlets yields that Mode 1 for design (Fig. 4.22b) contains a separated structure that is the same thickness as the separation region in the clean operating condition. At design operating condition with a distorted inlet, POD modes 2 (Fig. 4.22c) and 3 (Fig. 4.22d) contain a separation structure. The structure in mode 2 is thinner than the structure in mode 3 with each structure at 48% and 74% thicker than the clean separated structure respectively. It is typical for a POD mode to contain a structure smaller than the actual structure. Because all of

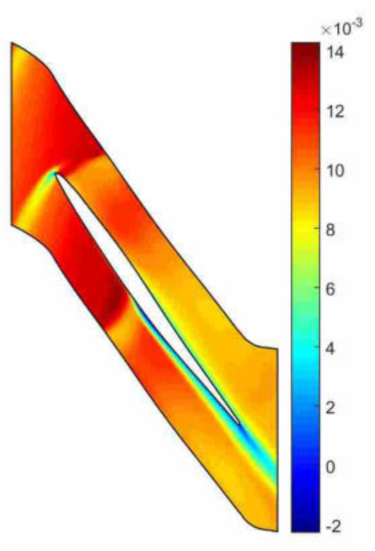

(a) Mode 1, clean inlet.

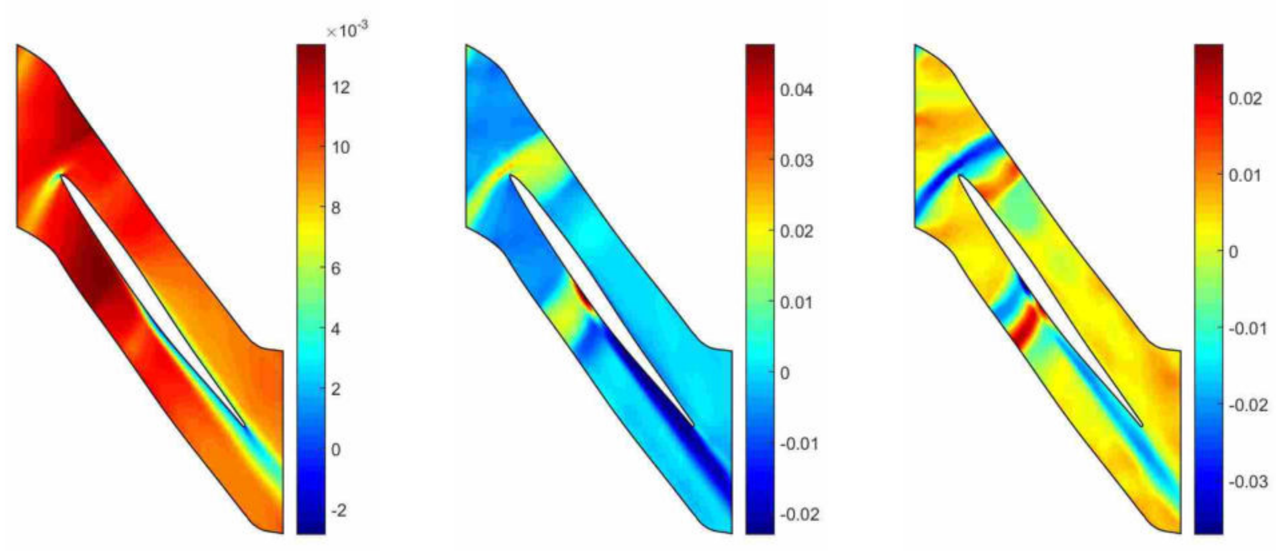

(b) Mode 1, distorted inlet (c) Mode 2, distorted inlet (d) Mode 3, distorted inlet

Figure 4.22: POD modes of axial velocity associated with the comparison of clean to distorted inlets. Design operating condition.

the POD modes are used together to reconstruct the data a single mode will often underestimate the size. In this case, mode 3 accurately predicts the maximum thickness of the shock wave structure.

4.3 Entropy Flux

Analysis of static pressure and axial velocity do well uncover the dynamics of the primary flow features. For this grid density, those flow features are the shock wave and the separation region. Vortex shedding is certainly present in this type of flow, but it was found that the grid density was not adequately refined to capture such small-scale activity. Static pressure reveals the dynamics of the shock wave, but does not provide information on the separation region. This is because the pressure is constant in this region. Axial velocity reveals both features, but because of velocity fluctuations downstream, the shock region is more difficult to decipher. POD is a useful tool for identifying the dynamics of the shock wave in axial velocity, because the modes filter out these higher order fluctuations. However, static pressure still proves more useful for analysis of the shock region because of the physical reasons mentioned above which make the flow in this region substantially less noisy.

Although observation of additional flow properties does not yield further insight into the dynamics of the shock wave and separation region, it is insightful to analyze additional properties to gain insight into how that particular property itself varies within the feature. Efficiency is a key area of interest to turbomachinery designers, and so entropy and related properties are useful for determining the regions where possible inefficiencies may reside.

Entropy flux is defined in Eqn. 4.2. It is introduced and used by Gorrell et al [56, 57]. Because this parameter relates the change in absolute entropy to density and axial velocity, it is able to more clearly define flow features such as vortex shedding and fluid wakes [58]. It also scales the magnitude of an entropy increase by the momentum flux, thus it more clearly identifies processes that increase entropy based on the momentum flux that is involved. This is advantageous for understanding the true impact of entropy generating processes. For example, processes involving a minor entropy increase but a high momentum flux are scaled proportional to the amount of total entropy generation.

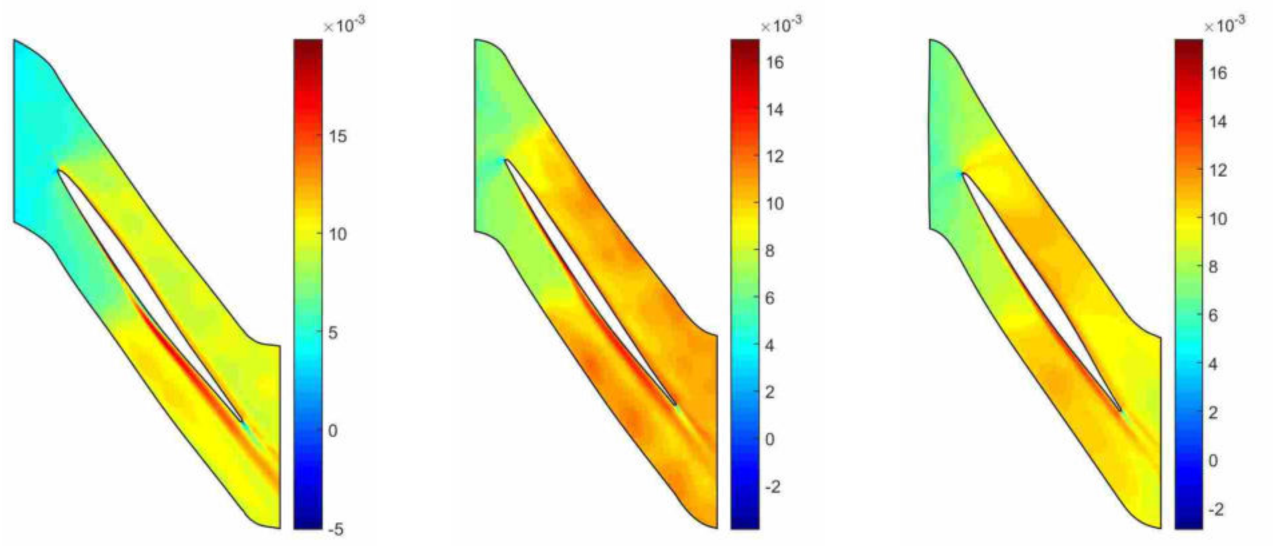

(a) Rotor 1.
(b) Rotor 2.
(c) Rotor 3.

Figure 4.23: POD mode 1 of entropy flux at design operating condition with distorted inlet.

$$s_{flux} = \frac{\rho U \Delta s}{C_p} \tag{4.2}$$

Figure 4.23 contains mode 1 of the entropy flux for all three rotors at design operating condition. Mode 1 identifies 3 distinct zones with different entropy flux levels. This is the case for all three rotors. Entropy flux is highest in the separation region. This is caused by low velocity, but high entropy and density. The primary reason for such high values in the separation region is because entropy is significantly higher in this region. An intermediate region of entropy flux is located after the shock wave outside of boundary layer. In this region velocity is low, entropy is slightly higher because of the shock wave, and density is high. Finally a low entropy flux region is located before the shock wave. In this case entropy and density are lowest but the velocity is relatively high. From the standpoint of efficiency, it is important to recognize that high entropy does not necessarily imply irreversibility or entropy generation. However, the high entropy in the separation region should be interpreted in the context that flow separation inherently generates entropy. It is then observed that the separation region is a primary region of inefficiency to be addressed in design work. The near stall condition has a much smaller separation region in rotors 2 and 3 when compared to design this is in agreement with previous analysis.

4.4 Alternative Methods: DMD Analysis of a Cylinder in Crossflow

One of the strongpoints of a DMD analysis is the ability to extract dominant frequencies and the flow features associated with them. The cylinder in crossflow is an ideal candidate for this type of analysis because the vortex shedding frequency is a well understood phenomonon. A cylinder in crossflow was simulated using Star CCM+ in order to evaluate the strength of each method in extracting the characteristic shedding frequency. Three simulations were run on the same geometry at a three different Reynolds numbers to simulate a range of shedding frequencies. The primary goal of this exercise was to compare the capabilities of POD and DMD in extracting the dominant shedding frequency. The actual shedding frequency was calculated from an FFT on the lift coefficient on the cylinder. This frequency was used as a benchmark for POD and DMD to compare to.

The cylinder in crossflow simulation was performed using a mesh from the Star CCM+ tutorial files. The mesh is presented below in Fig. 4.24. As can be seen the mesh has been refined in the wake region as well as in proximity to the cylinder. The fluid being modeled is incompressible air. The inlet boundary condition is a constant freestream velocity. The walls are modeled as symmetry planes, and the outlet is a constant pressur boundary condition. The flow is modeled as laminar. Grid independance was not studied because the mesh used was from a tutorial file. The simulation produced results in agreement with those of Daily et al. [59] for the first simulation case. It was then assumed that the mesh was sufficient for the variation in Reynolds number associated with this investigation. Additionally the main purpose of this investigation was to investigate the various abilities of POD and DMD to extract frequency information. As long as a consistent and measurable frequency was produced by the simulation, it would serve the purposes of this analysis.

Vortex shedding is a transient phenomenon and so coupled implicit unsteady solver was used to converge each time step. The Courant Number was set to 100 and each time step was 0.02 s. Maximum inner iterations were set to 15 which produced sufficiently low residual values. The coefficient of lift was monitored to establish the time when the simulation had reached a quasi-steady vortex shedding pattern. The coefficient of lift is shown in Fig. 4.25. As can be seen in the figure, the simulation reaches a quasi-steady vortex shedding pattern at roughly 8 seconds. A contour plot of vorticity at 12 seconds is shown in Fig. 4.26. The same procedure was implimented

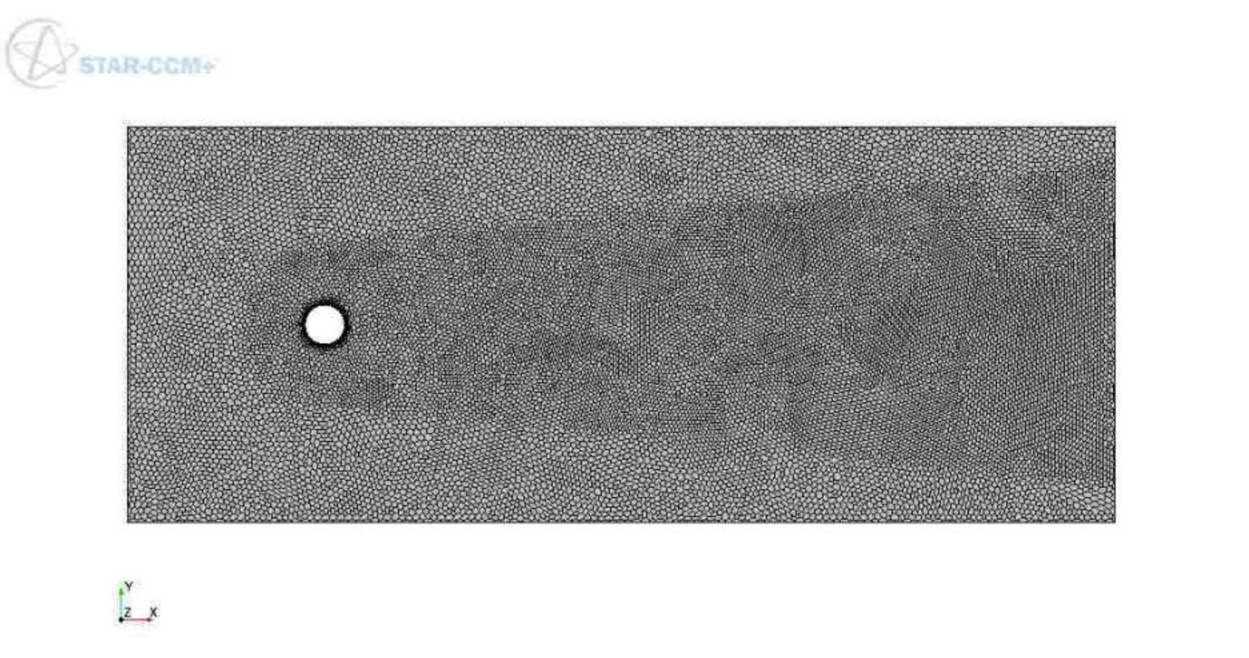

Figure 4.24: Unstructured mesh for cylinder in crossflow simulation.

to produce 3 simulations at various Reynolds numbers. The simulations were then post-processed using POD and DMD.

By showing that DMD could correctly extract the frequency we would have reasonable assurance that the DMD algorithm was being implemented correctly as outlined by Schmid [22]. DMD could then be objectively compared to the POD algorithm so that conclusions could then be made about the advantages of each.

Table 4.1 contains the results of the post-processing using POD and DMD. U is the freestream velocity, D is the diameter of the cylinder, Re is the Reynolds number, St is the Strouhol number, f_{Cl} is the characteristic shedding frequency as measured from the coefficient of lift, and f_{POD} and f_{DMD} are the extracted characteristic frequencies using POD and DMD, respectively. These are the only two components extracted by POD and DMD in this data. Velocities and dimensionless numbers serve as inputs to produce the simulation data. The Reynolds number ranges from 75 to 175 through the 3 simulations. This corresponds to a good range for which the Strouhol number is well correlated with Reynolds number in predicting the shedding frequency. Additionally, because theReynolds number is relatively low, the variation in Reynolds number is significant enough to vary the frequency a substantial amount, which was the key objective of this investigation.

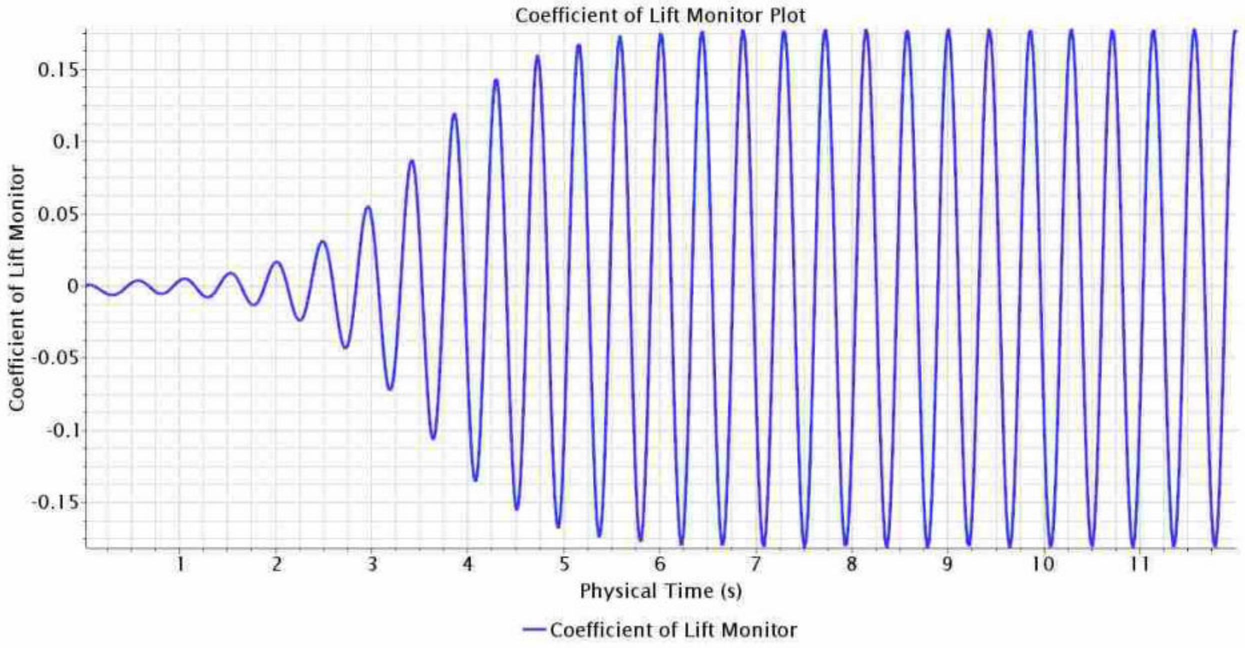

Figure 4.25: Coefficient of lift monitor plot for the cylinder in crossflow.

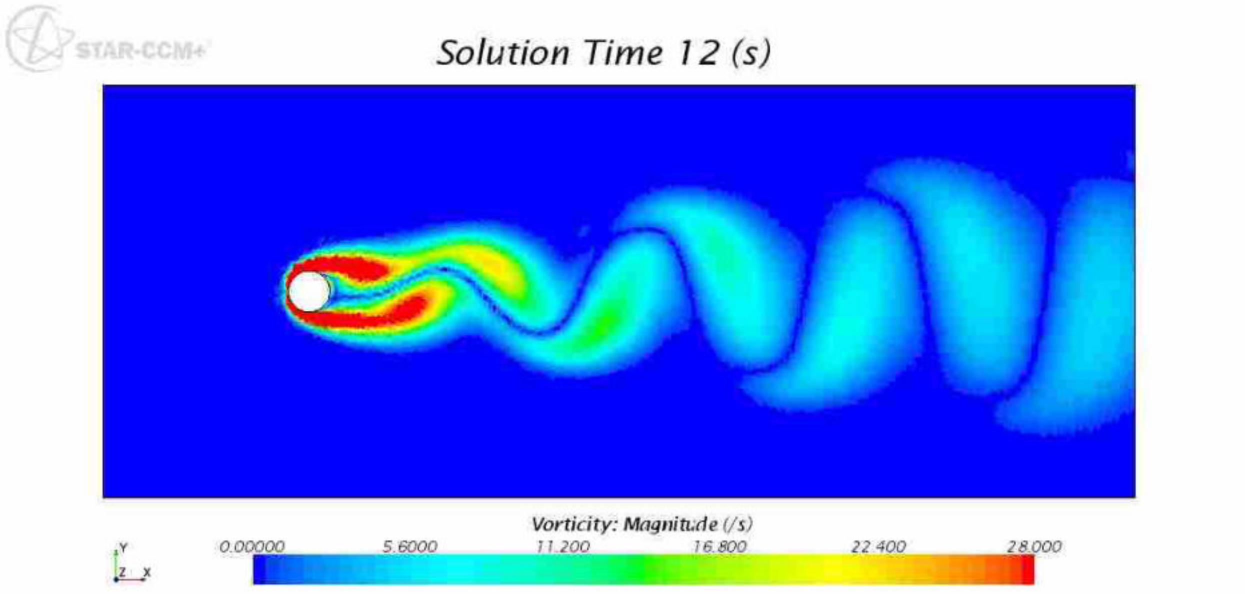

Figure 4.26: Contour plot of vorticity at 12 seconds.

Table 4.1: Results of Cylinder in Crossflow Simulation Post-Processing

	Case 1	Case 2	Case 3
U (m/s)	0.15	0.25	0.35
D (m)	0.01	0.01	0.01
Re	75	125	175
St	0.15	0.1592	0.185
f_{Cl}	2.25	3.98	6.48
f_{POD}	2.25	3.98	6.48
f_{DMD}	2.34	4.099	6.37

DMD is able to capture the general trend but is not as accurate as POD in capturing the shedding frequency. It should be noted that extracting the frequencies using POD requires additional frequency analysis (fourier analysis) of the expansion coefficients. The frequencies yielded by the DMD algorithm are inherent to the matrix decomposition and are a direct output of the method itself. POD by itself gives no information on the temporal dynamics.

Figure 4.27 shows the DMD eigenvalue spectrum for the first case. The eigenvalue containing the dominant frequency can be easilly identified using the ranking based on the coherence norm (the dark red circle not at zero). It is important to note that there are lower frequency modes in between the dominant frequency and the eigenvalue at zero. The coherence norm is the critical piece of information which enables the identification of the dominant frequency. The coherance norm is obtained using the POD modes. The real component for this eigenvalue is close to zero which suggests a neutrally stable feature. The corresponding mode is shown in Fig. 4.28a with mode 2 from the POD analysis shown below it in Fig. 4.28b. They are extremely similar as both are capturing the same feature. It is also expected that they should look similar because this DMD mode was selected based on the coherence norm which is evaluated based on which DMD modes most closely resemble the POD modes.

In an FFT of the mode 2 coefficients from the POD analysis, the frequency leakage mentioned in [28] was observed but this does not affect the accuracy of the dominant frequency extraction.

In light of the example shown above, we make the following conclusions about the claims made in the introduction. The claim that DMD provides additional information not provided by

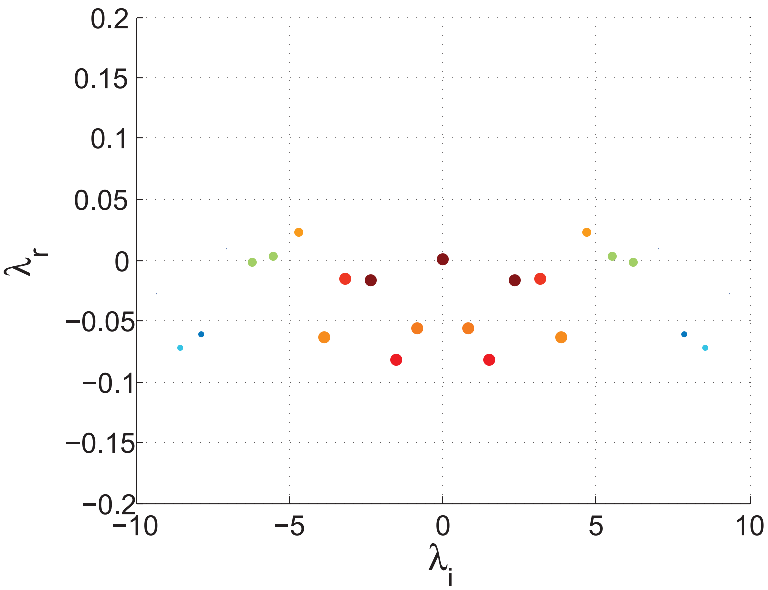

Figure 4.27: DMD Eigenvalue Spectrum for Case 1 of Cylinder in Crossflow.

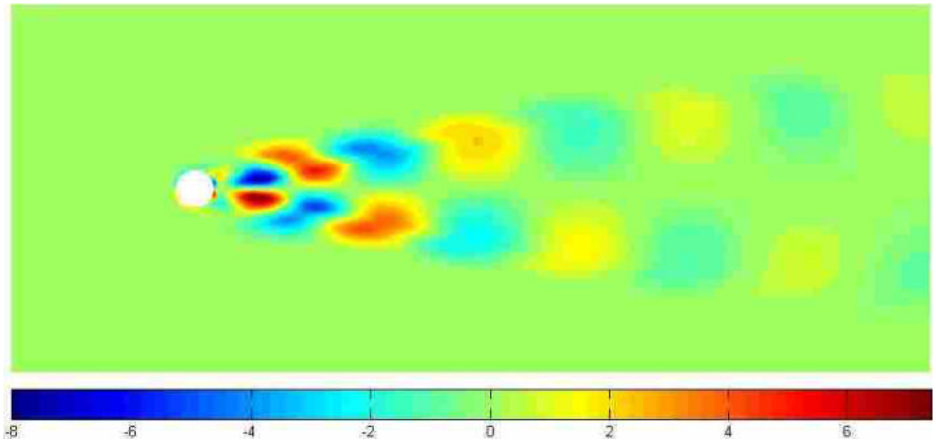

(a) DMD mode 2 from case 1

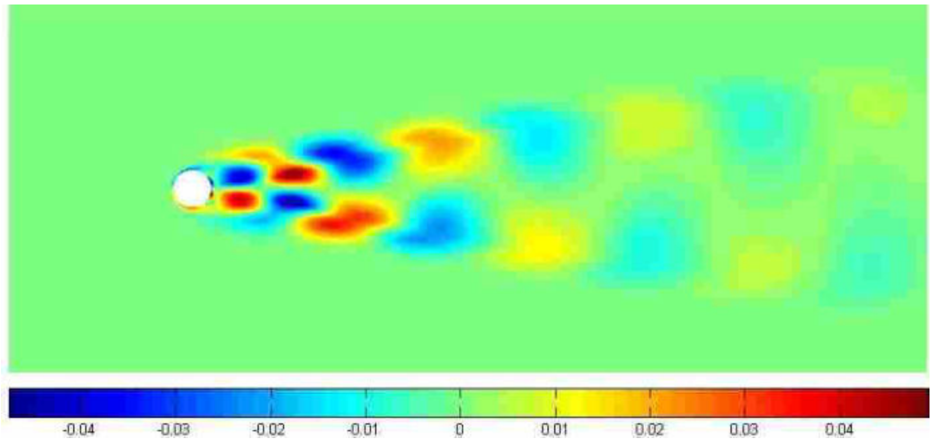

(b) POD mode 2 from case 1

Figure 4.28: Comparison of DMD and POD vortex shedding modes.

POD [27] is true but it is possible to obtain the frequency information using additional techniques. It is not possible to obtain stability information about a given feature using POD.

While it is true that DMD provides different modes than POD [28] it gives no indication of their relative significance to characterizing the flow. One must make the assumption that modes associated with the lowest frequencies are the most significant and this may not necessarily be the case. For example, the DMD eigenvalue spectrum shown in Fig. 4.27 contains several modes associated with frequencies lower than the dominant frequency identified by the combined POD analysis. There is no way of evaluating which mode corresponds to the dominant frequency without the ranking provided by POD. It is then a significant challenge to know which of the many DMD modes to give significant consideration in analysis. A significant advantage of POD is the ranking of the modes provided in the eigenvalue spectrum. In our analysis the DMD modes were ranked according to energy content using the POD modes. This resulted in the most significant DMD modes appearing very similar to the POD modes. By ranking the modes in this way DMD provided very little new information. If there are other ways to determine which DMD modes are the most significant we are not currently aware of them and more research needs to be done on the subject. In summary, while sorting the modes according to frequency may be more desirable, this method alone gives no indication of which modes are the most important. It is the combined method of frequency isolation with energy ranking using POD that has proven to be most effective.

Finally Schmid's claim that the POD modes can be misleading [22] in the sense that the high energy modes may not contain all of the information that is relevant to the flow is likely true based on his research on the subject. It is important to recognize this possible shortcoming of the method in an analysis setting. Neither POD nor DMD is comprehensive in its ability to clearly segregate and extract every feature. Rather, each method extracts features and dominant flow behavior based on certain criteria. For this reason both methods are recommended for use as tools for analysis.

CHAPTER 5. CONCLUSION

High-Fidelity time-accurate simulations are now established as a useful means to understand the effects of distortion on the performance of fans and compressors. A new method to analyze and quantify the effects of distortion around the circumference of individual blade rows in a multistage fan has been presented. This method identifies the important contributions of unsteady flow necessary to accurately model the complex flow physics associated with distorted flow. In the analysis of large CFD datasets, POD provides a means of obtaining the most information about a simulation in the most consise way possible. Mathematically, POD is a linear spectral method which represents a data matrix as a linear combination of modes. These modes are the principle components of the data and characterize the mean behavior of the data as well as the variation from the mean. The basis vectors, called basis modes capture the spatial variance while the associated modal coefficients characterize the variation with a third dimension. This allows for an efficient preliminary analysis of the data in order to establish meaningful direction for further inquiry into topics of interest. In this analysis the variables of static pressure axial velocity, and entropy flux were analyzed for 3 rotors of a compressor with a distorted inlet. Design and near stall operating conditions were compared as well as clean inlet operating conditions. This analysis establishes POD as a useful means for efficent analysis of large CFD data. This research also represents the first published research using POD as an analysis tool to study the effects of inlet distortion turbomachinery.

To exhibit the range of capabilities of POD as a tool for analysis of distorted flow, an in depth presentation of the POD results for rotor 1 at design operating condition with a 1/rev total pressure inlet condition was analyzed. The POD shows shock movement resulting from such a distortion. Mode 1 contains information on the average behavior of the flow. Higher order modes contain information representing the variation of the data from the mean values. Therefore, the information they carry is concentrated around flow features that vary with time and space. Mode 2 of this POD characterized the motion of the shock waves. Modes 3 and 4 characterized the exact location of the shock front at a given angular location and also the motion of the shock as the blade rotates. While the modal values are associated with a particular location in space, the coefficient values are associated with a particular angular location in the blade row. The coefficients captured the variation in the data with angular position, or time if the blade were allowed to rotate through the distortion to that location. Mode 1 coefficients captured the effect of the 1/rev distorted inlet condition on the blade row with the amplitude containing information on the magnitude of the distortion. Higher order coefficient captured the information on the fluctuation from the mean.

POD mode analysis showed the range of shock motion in rotor 3 was noticibly greater (34.0% of chord) compared to rotor 1 (18.2% of chord). Actual measurement of the shock wave range of motion yielded values of 35.9% and 18.6% for rotor 3 and rotor 1, respectively. This research established that the modes are accurate in characterizing the relative change in shock wave motion and may be used as a tool for measuring the range of motion of the shock. In this study the modes were accurate in predicting the range of motion of the shock wave accurate to within 2% of the chordlength.

Analysis of the standard deviation of the coefficients showed an increase in standard deviation corresponded to an amplification of the distortion pattern, while a decrease correlates to an attenuation of the distortion pattern. This multistage fan analysis showed because the average distorted flow behavior is attenuated in rotor 3 due to the exit condition, the effects of transferred to shock wave oscillations. The modal coefficients suggests that mode 2 is where the majority of the distortion effects are captured, and the corresponding mode 2 reveals that the distortion is most influencing the location of the shock wave. This illustrates the benefits of gaining insight from the extracted components of POD. This is an example of how POD may be used as a tool to establish dominant flow behavior. In this particular case the identification of dominant flow behavior, and the shift in dominant behavior from mean pressure field oscillation to shock wave range of motion was made straightforward through POD. Without the use of POD in this study this behavior would not have been obvious and may not have been identified.

The coefficients were analyzed to show the variation of the data with angular location. The 1/rev total pressure distortion pattern was observed with the most pronounced magnitude in the coefficients for modes 1 and 2. From this it was shown that the distortion most drastically affects the flow features associated with modes 1 and 2 which were the average flow behavior and location of the shock wave on the blade at a given angular position.

A comparison of the rotors showed the 1/rev distortion pattern present throughout the coefficients for all three rotors. A distortion amplification was observed between rotors 1 and 2 with an attenuation between 2 and 3. This attenuation yielded a corresponding increase in shock front location variation in rotor 3.

Generally speaking, clean inlet modes look very different from their distorted counterparts. They captured more subtle variations in the data due to the absence of the more drastic 1/rev distortion variation. This corresponded to much smaller singular values in the clean case. However, blade row interactions created variation in the data which caused oscillation in the shock front in rotor 3. This caused the modes to look more like the distorted case. The difference between the two flows was captured in the coefficients with the distorted carrying a clear 1/rev oscillation while the clean carried oscillations of much higher frequency and smaller magnitude.

In the static pressure analysis mode 2 was found to consistently capture the range of motion of the shock front for both design and near stall. In the near stall case the shock wave was pushed forward and its range of motion decreased. This was attributed to a decrease in pressure ratio variation due to the increased back pressure. In general it is concluded that as the fan approaches stall the apparent effects of distortion are minimized. This is because the change in operating condition places the fan at a different position on the speedline. This leads to less variation in the operating condition because the location on the speedline is such that the effects of distortion are less pronounced.

Analysis of the axial velocity indicated the presence of a wake like structure which was concluded to be a separation region. This structure was much more prominent and dynamic in rotor 1. A comparison to the clean inlet data showed the separation region is also present in the clean simulation but it is not a dynamic structure. The conclusion was made that this separation in rotor 1 is not caused by the distortion but it is heavily influenced by the inlet conditions. A comparison of the original CFD for design and near stall was made and measurements were taken of the width of the separated region. It was found that the near stall condition does not produce as thick of a separation region due to the decreased range of motion of the shock wave. Once again the conclusion was made that as the fan approaches stall the effects of distortion are lessened which leads to less variation in the operating condition. Entropy flux was used to identify 3 distinct entropy flux levels in the blade row passage. The separated region was the region with the highest entropy due to the irreversibilities associated with separation.

It is possible to arrive at many of the conclusions above through the use of more traditional analysis methods. However these observations about the physics of distorted flow through turbomachinery were made much simpler through the use of POD. POD enables the researcher to distill a large dataset to a few images (modes and coefficients) which contain a large amount of information. Because the information is represented so concisely it enables the researcher to identify the most dominant phenomenon and direct investigation toward these phenomenon of interest. It is then also possible to investigate large sets of related data quickly to investigate the same phenomenon. In this way, because the phenomenon of interest is identified early, more effort may be allotted to investigation specific aspects of the phenomenon or over a large variety of data.

5.1 Future Work

Promising directions for future work in the use of POD in turbomachinery analysis include further investigation of the quadruple POD, alternative methods to percent energy, and investigating the possibilities of using POD to determine the stability of flow structures. In the subject of DMD, the possibilities include investigating the effect of grid refinement on DMD output and frequency prediction, methods for improving the accuracy of frequency prediction, and the accuracy of DMD in predicting the stability of flow structures.

The quadruple POD is introduced in the literature review chapter referencing the work of Zhaung and Hung [12]. Quadruple POD separates flow features into dominant and fluctuating structures by dividing them into four categories: dominant structure, coherent structure, turbulent structure, and noise structure. Since turbomachinery flows are inherently turbulent, and managing and understanding turbulence in turbomachinery is a key subject of interest among designers, the quadruple POD seems to be a promising tool to increase understanding of this subject. The fact that the quadruple POD sorts flow features into a turbulent structure seems promising for quantifying turbulent parameters of interest. Perhaps a promising direction forward with this method would be to develop a technique to impliment it on a turbmachinery dataset and analyze the output in the context of other well known turbulent flow parameters.

Percent energy is often reported as a parameter for quantifying the accuracy of a POD reconstruction. The term itself is a misnomer which is prominant throughout the literature. It is a misnomer because it does not quantify energy at all. It is named such because velocity data is commonly used in POD datasets, and energy is derived from velocity, however the term is still used when other variables are used. In addition, percent energy is not an accurate parameter to measure the quality of a reconstruction. It reports the contribution of the higher order modes beginning with mode 2, and in some cases the higher order modes do little to improve the accuracy of a reconstruction. For example, in a flow with little or no variation, a very accurate reconstruction can be created with just a few modes, but the corresponding percent energy will be small indicating a low accuracy. A parameter that best characterizes the contribution of an individual mode, and the accuracy of a reconstruction would be of interest to the community of researchers using POD in the reporting of their results.

Finally, there has not been much work using POD to quantify or identify the stability of a flow structure. Authors on DMD [22, 27, 28] claim that POD is lacking in this ability. It would be useful to evaluate the suitability of POD to determine the stability of a structure. Perhaps using a dataset containing a feature with a known growth or decay rate would be useful to benchmark whether POD is capable of extracting such information.

Authors using DMD [22, 27, 28] claim the ability to evaluate the frequency and stability of flow structures using eigenvalues from the DMD output. These claims have been verified in this thesis, but it was found that DMD was not as accurate as frequency analysis of POD coefficients. One hypothesis for the cause of the innacuracy was the density of the grid. It would be very useful to have information about the effect of grid density on DMD output. The question whether there is an ideal grid size or time step spacing to yield the most accurate results would be a boon to researchers evaluating whether DMD would be a beneficial tool in their analysis. Ideally this would fix the issues of less accurate frequency and stability predictions, making DMD an ideal tool for analysis under the correct conditions.

REFERENCES

[1] Weston, D., 2014. "High Fidelity Time Accurate CFD Analysis of a Multi-stage Turbofan at Various Operating Points in Distorted Flow." MS Thesis, Brigham Young University, Provo, UT, June. 2, 19, 20, 32, 35, 61

[2] Blanc, T. J., Gorrell, S. E., Jones, M. R., and Duque, E. P. N., 2013. "Analysis and Compression of Time-Accurate Turbomachinery Simulations Using Proper Orthogonal Decomposition." AIAA Paper 2013-3620. 2, 6, 14, 20

[3] Chatterjee, A., 2000. "An introduction to the proper orthogonal decomposition." *Current Science,* **78**(7), April, pp. 808–817. 5, 7

[4] Blanc, T., 2014. "Analysis and Compression of Large CFD Data Sets Using Proper Orthogonal Decomposition." MS Thesis, Brigham Young University, Provo, UT, April. 5, 6, 7, 8, 14, 20, 29, 104

[5] Blanc, T. J., Jones, M. R., Gorrell, S. E., and Duque, E. P. N., 2016. "Reduced Order Modeling of Conjugate Heat Transfer Processes." ASME Journal of Heat Transfer, **138**(051703). 6, 8

[6] Pobitzer, A., Tutkun, M., Andreassen, O., Fuchs, R., Peikert, R., and Hauser, H. "Energy-scale aware feature extraction for flow visualization." IEEE Symposium on Visualization. 9

[7] Roussinova, V., Shinneeb, A.-M., and Balachandar, R., 2010. "Investigation of fluid structures in a smooth open-channel flow using proper orthogonal decomposition." *Journal of Hydraulc Engineering,* **136**(3), March, pp. 143–154. 9, 10

[8] Shim, Y. M., Sharma, R. N., and Richards, P. J., 2013. "Proper orthogonal decomposition analysis of the flow field in a plane jet." *Experimental Thermal and Fluid Science,* **51**. 10

[9] Feng, L.-H., Wang, J.-J., and Pan, C., 2011. "Proper orthogonal decomposition analysis of vortex dynamics of a circular cylinderunder synthetic jet control." *Physics of Fluids,* **23**(014106). 10

[10] Greig, D., Siddiqui, K., Karava, P., and Elatar, A., 2015. "Investigation of fundamental flow mechanisms over a corrugated waveform using proper orthogonal decomposition and spectral analysis." *International Journal of Thermal Sciences,* **96**. 11

[11] Charalampous, G., and Hardalupas, Y., 2014. "Application of proper orthogonal decomposition to the morphological analysis of confined co-axial jets of immiscible liquids with comparable densities." *Physics of Fluids,* **26**(113301). 11

[12] Zhuang, H., and Hung, D. L. S., 2016. "Characterization of the effect of intake air swirl motion on time-resolved in-cylinder flow field using quadruple proper orthogonal decomposition." *Energy Conversion and Management,* **108**. 12, 82

[13] Ruscher, C. J., Dannenhoffer III, J. F., and Glauser, M. N., 2013. "Application of snapshot pod on a varying grid." AIAA Aerospace Sciences Meeting Including the New Horizons Forum and Aerospace Exposition. 13

[14] Mulleners, K., and Raffel, M., 2012. "The onset of dynamic stall revisited." *Experimental Fluids,* **52**. 13

[15] Rencher, A. C., and Christensen, W. F., 2012. *Methods of Multivariate Analysis.*, 3^{rd} ed. Wiley Series in Probability and Statistics. John Wiley & Sons Inc., Hoboken, New Jersey, Chap. 12, pp. 405–432. 13

[16] Brenner, T. A., Carpenter, F. L., Freno, B. A., and Cizmas, P. G. A. "A reduced-order model for turbomachinery flows using proper orthogonal decomposition." ASME Turbo Expo. 14

[17] Epureanu, B. I., 2003. "A parametric analysis of reduced order models of viscous flows in turbomachinery." *Journal of Fluids and Structures,* **17**, March, pp. 971–982. 14

[18] Epureanu, B. I., Hall, K. C., and Dowell, E. H., 2001. "Reduced-Order Models of Unsteady Viscous Flows in Turbomachinery Using Viscous-Inviscid Coupling." *Journal of Fluids and Structures,* **15**, pp. 255–273. 14

[19] He, L., and Ning, W., 1998. "Efficient approach for analysis of unsteady viscous flows in turbomachines." *AIAA Journal,* **46**(11), pp. 2005–2012. 14

[20] Hall, K. C., Thomas, J. P., and Clark, W. S., 2002. "Computation of unsteady nonlinear flows in cascades using a harmonic balance technique." *AIAA Journal,* **40**(5), May, pp. 879–886. 14

[21] He, L., 2010. "Fourier methods for turbomachinery applications." *Progress in Aerospace Sciences,* **36**, June, pp. 329–341. 14

[22] Schmid, P. J., 2010. "Dynamic Mode Decomposition of Numerical and Experimental Data." *Journal of Fluid Mechanics,* **656**, July, pp. 5–28. 15, 16, 17, 74, 78, 83

[23] Schmid, P. J., Li, L., Juniper, M. P., and Pust, O., 2011. "Applications of the dynamic mode decomposition." *Theoretical Computational Fluid Dynamics,* **25**. 15, 30, 31

[24] Tu, J. H., Rowley, C. W., and Luchtenburg, D. M., 2013. "On dynamic mode decomposition: Theory and applications." *Journal of Computational Dynamics*. 15

[25] Grilli, M., Schmid, P. J., Hickel, S., and Adams, N. A., 2011. "Analysis of unsteady behavior in shockwave turbulent boundary layer interaction." Proceedings of the 7th European Symposium on Aerothermodynamics. 16, 68

[26] Mariappan, S., Gardner, A. D., Richter, K., and Raffel, M., 2014. "Analysis of dynamic stall using dynamic mode decomposition technique." *AIAA Journal,* **52**(11). 16

[27] Sampath, R., and Chakravarthy, S. R., 2014. "Proper Orthogonal and Dynamic Mode Decompositions of Time-Resolved PIV of Confined Backward-Facing Step Flow." *Journal of Experimental Fluids,* **1792**. 16, 78, 83

[28] Zhang, Q., Liu, Y., and Wang, S., 2014. "The Identification of Coherent Structures Using Proper Orthogonal Decomposition and Dynamic Mode Decomposition." *Journal of Fluids and Structures,* **49**, May, pp. 53–72. 16, 17, 76, 78, 83

[29] Lumley, J. L., 1970. *Stochastic Tools in Turbulence*. Academic Press, USA. 16

[30] Cousins, W. "History, philosophy, physics, and future directions of aircraft propulsion system/inlet integration." In *Proceedings of ASME Turbo Expo 2004*. 17, 18

[31] Mazzawy, R., 1977. "Multiple Segment Parallel Compressor Model for Circumferential Flow Distortion." *Transaction of the ASME, Journal of Engineering for Power*, April, pp. 288–296. 18

[32] Reid, C., 1969. The Response of Axial Flow Compressors to Intake Flow Distortion ASME Paper 69-GT-29, ASME. 18

[33] Hynes, T., and Greitzer, E., 1987. "A Method for Assessing Effects of Circumferential Flow Distortion on Compressor Stability." *Journal of Turbomachinery,* **109**, July, pp. 371–379. 18

[34] Cumpsty, N. A., 1989. *Compressor Aerodynamics*. Longman Group UK Ltd., London, England. 18

[35] Longley, J. P., 1990. "Measured and Predicted Effects of Inlet Distortion on Axial Compressors" ASME Paper 90-GT-214. 18

[36] Yao, J., Gorrell, S., and Wadia, A., 2010. "High-fidelity numerical analysis of per-rev-type inlet distortion transfer in multistage fans–part ii: Entire component simulation and investigation." *Journal of Turbomachinery,* **132**(041015), October, pp. 1–17. 18, 19, 20, 37, 47, 51

[37] Gorrell, S. E., Yao, J., and Wadia, A. R., 2008. High Fidelity URANS Analysis of Swirl Generation and Fan Response to Inlet Distortion *AIAA paper 2008-4985*, 44th AIAA/ASME/SAE/ASEE Joint Propulsion Conference & Exhibit, Hartford, CT, July. 18, 42

[38] Fidalgo, V. J., Hall, C. A., and Colin, Y., 2012. "A study of fan-distortion interaction within the nasa rotor 67 transonic stage." *Journal of Turbomachinery,* **134**, September. 18, 33

[39] Seddon, J., 1984. "Understanding and countering the swirl in S-ducts: tests on the sensitivity of swirl to fences." *Aeronautical Journal,* **88**, April, pp. 117–127. 18

[40] Pazur, W., and Flottner, L., 1991. "The Influence of Inlet Swirl Distortions on the Performance of a Jet Propulsion Two-Stage Axial Compressor." *Transactions of the ASME, Journal of Turbomachinery,* **113**, April, pp. 233–240. 18

[41] Longley, J. P., and Greitzer, E. M., 1992. "Inlet Distortion Effects in Aircraft Propulsion System Integration." In *Steady and Transient Performance Prediction of Gas Turbine Engines, AGARD-LS-183*. 18

[42] Govardhan, M., and Viswanath, K., 1996. Effect of circumferential Inlet flow distortion and swirl on the flow field of an axial flow fan stage ASME Paper 96-GT-263, ASME. 18

[43] Sheoran, Y., Bouldin, B., and Krishnan, P. M., 2012. "Compressor Performance and Operability in Swirl Distortion." *Journal of Turbomachinery,* **134**(041008), Jul. 18

[44] Sghaier, T. B., Mehdi, A., Pachidis, V., and MacManus, D., 2013. "A Parametric Numerical Study of the Effects of Inlet Swirl Distortion on a Transonic Compressor Stage." ASME Paper GT2013-94374. 18

[45] Nessler, C. A., Copenhaver, W. W., and List, M. G., 2013. "Serpentine Diffuser Performance with Emphasis on Future Introduction to a Transonic Fan." AIAA Paper 2013-0219. 18

[46] Sanders, D. D., and List, M. G., 2013. "CFD Performance Predictions of a Serpentine Diffuser Configuration in an Annular Cascade Facility." AIAA Paper 2013-0220. 18

[47] Yao, J., Gorrell, S., and Wadia, A., 2010. "High-fidelity numerical analysis of per-rev-type inlet distortion transfer in multistage fans–part i: Simulations with selected blade rows." *Journal of Turbomachinery,* **132**(041014), May, pp. 1–10. 19, 37

[48] Marshall, M., 2014. "Validation of a Modified Version of OVERFLOW 2.2 for Use with Turbomachinery Under Clean and Total Pressure Distorted Conditions and a Study of Blade Loading in Distortion." MS Thesis, Brigham Young University, Provo, UT, Junel. 20, 35

[49] Marshall, M., Weston, D., Gorrell, S., and Wallis, C., 2013. "Validation of overflow 2.2 for use with turbomachinery." In *Proceedings of the 49th AIAA/ASME/SAE/ASEE Joint Propulsion Conference*, AIAA Paper number 3626. 20, 32

[50] Nichols, R. H., Denny, A. G., Calahan, J. A., Sirbaugh, J. R., Klepper, J. B., and Heikkinen, B. D., 2011. "Firebolt v2.0 - Structured Grid Navier-Stokes Code for Airfram/Propulsion Integration." *AIAA Paper*. 32

[51] Vahdati, M., Freeman, C., and Imregun, M., 2005. "On the use of atmospheric boundary conditions for axial-flow compressor stall simulations." *Journal of Turbomachinery,* **127**, April, pp. 349–351. 32

[52] Weston, D., Marshall, M., Gorrell, S., and Wallis, C. "Analysis of turbofan performance under total pressure distortion at various operating points." In *Proceedings of ASME Turbo Expo 2015*. 34

[53] Hilgenfeld, L., Cardamone, P., and Fottner, L., 2003. "Boundary Layer Investigations on a Highly Loaded Transonic Compressor Cascade with Shock/Laminar Boundary Layer Interactions ." *Journal of Power and Energy,* **217**. 68

[54] V., G. D., 2015. "Progress in Shock Wave/Boundary Layer Interactions ." *Progress in Aerospace Sciences,* **72**, September, pp. 80–99. 68

[55] Michelassi, V., 1997. "ShockBoundary Layer Interaction and Transition Modelling in Turbomachinery Flows." *Proc Instn Mech Engrs,* **211**. 68

[56] Gorrell, S. E., Okiishi, T. H., and Copenhaver, W. W., 2003. "Stator-Rotor Interactions in a Transonic Compressor, Part 2: Description of a Loss Producing Mechanism." *ASME Journal of Turbomachinery,* **125**, pp. 336–345. 71

[57] Gorrell, S. E., Car, D., Puterbaugh, S. L., Estevadeordal, J., and Okiishi, T. H., 2006. "An Investigation of Wake-Shock Interactions With Digital Particle Image Velocimetry and Time-Accurate Computational Fluid Dynamics." *ASME Journal of Turbomachinery,* **128**, pp. 616–626. 71

[58] List, M. G., Gorrell, S. E., and Turner, M. G., 2010. "Investigation of Loss Generation in an Embedded Transonic Fan Stage at Several Gaps Using High-Fidelity, Time-Accurate Computational Fluid Dynamics ." *ASME Journal of Turbomachinery,* **132**. 71

[59] Daily, J. W., and Harleman, D. R. F., 1966. *Fluid Dynamics*. Addison-Wesley, MA. 73

APPENDIX A. POD MODES

This appendix contains POD modes 1-4 for the variables of static pressure, total pressure, static temperature, total temperature, entropy, entropy flux, and axial velocity. These were the variables analyzed in the results chapter. Many of the modes were commented on in the analysis but in many cases the modes were not shown for brevity. Both design and near stall operating condition are shown for rotors 1-3. All of the modes considered are shown in this appendix. The scaling of the colorbar is based on the maximum and minimum values of the mode rather than a standard set of values for all of the modes. In this way the color plot is leveraged to highlight the most prominant features of the flow relative to itself. This seems to be the method of plotting which reveals the most insight.

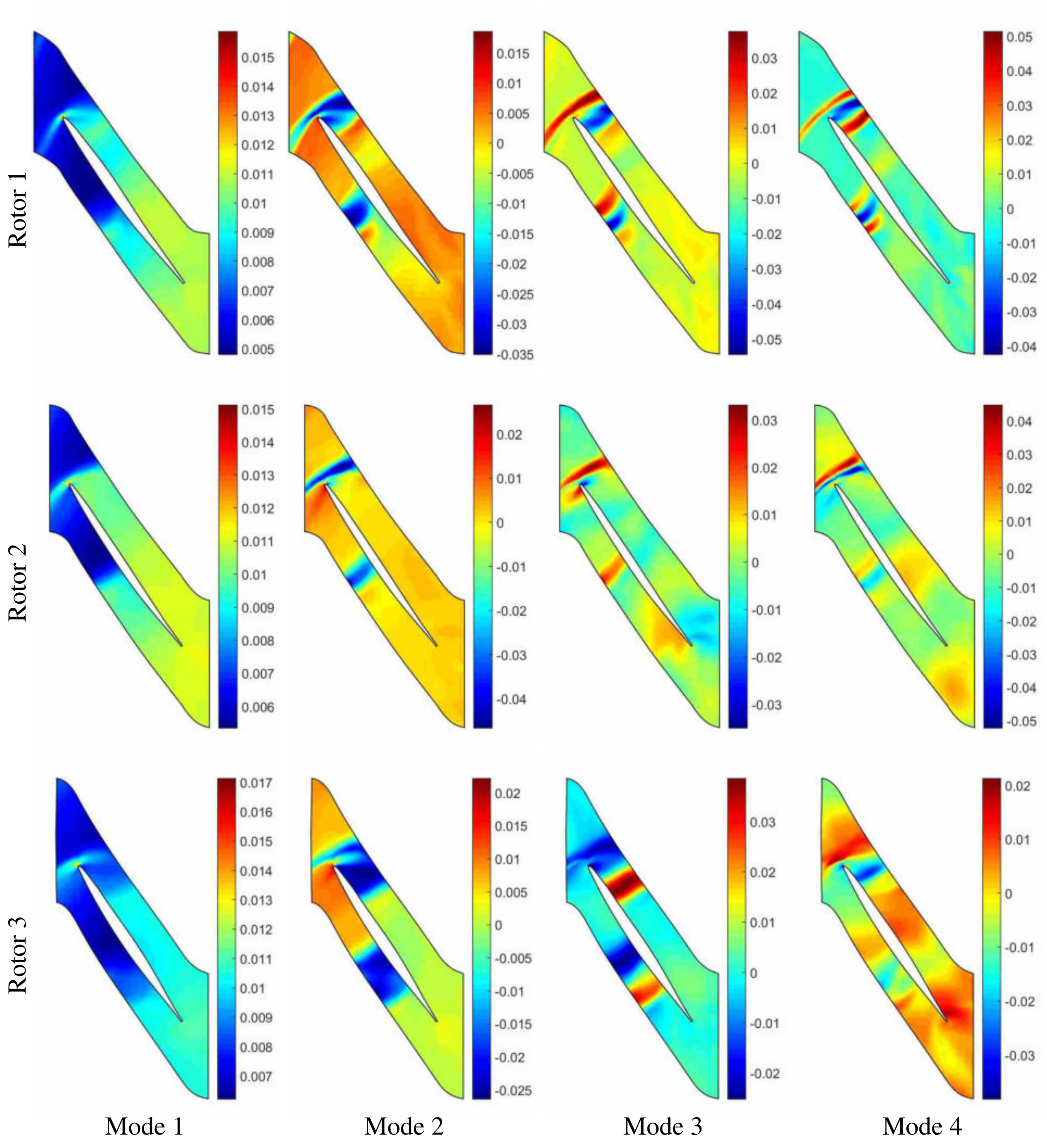

Figure A.1: Static pressure, design operating condition.

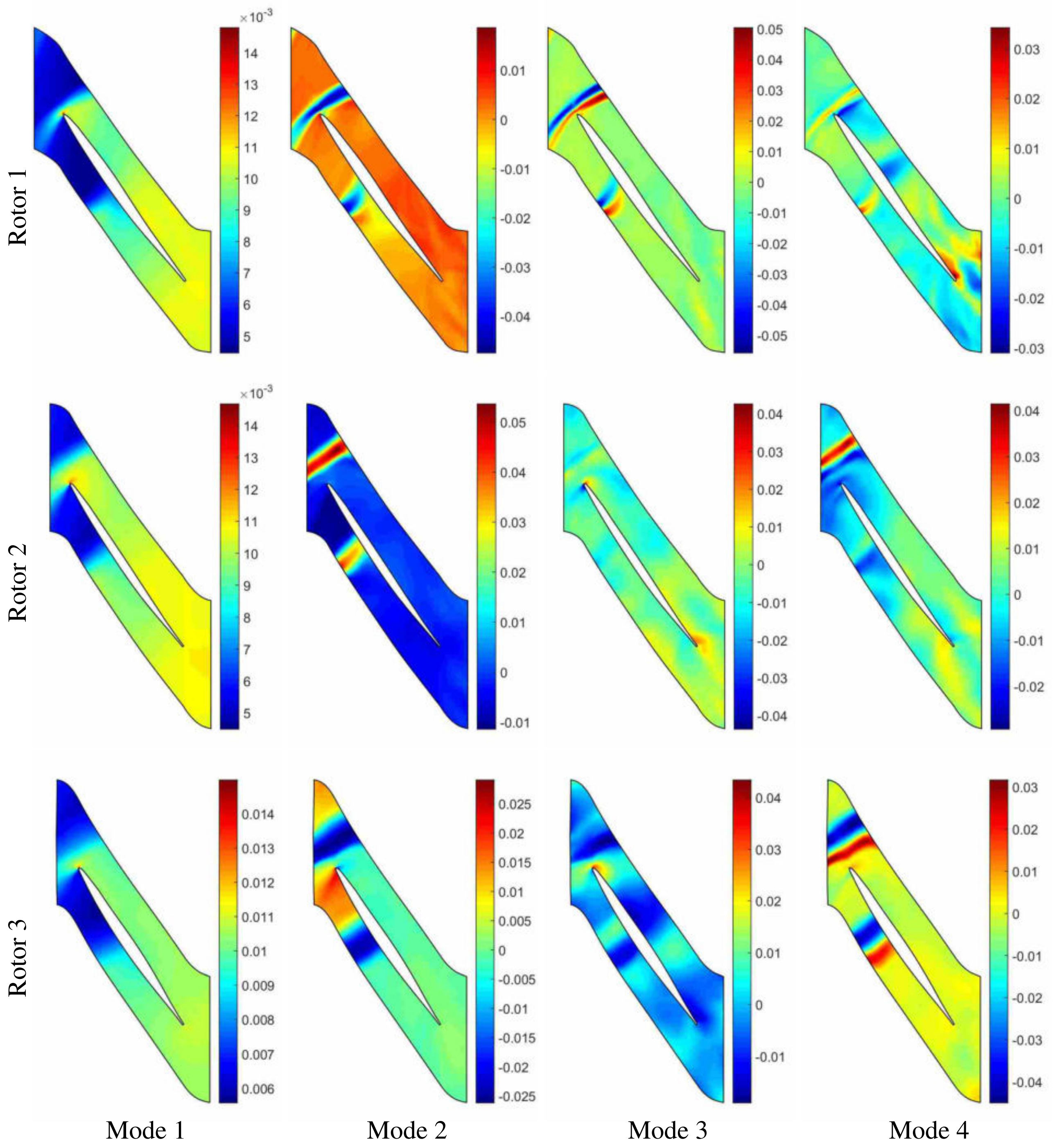

Figure A.2: Static pressure, near stall operating condition.

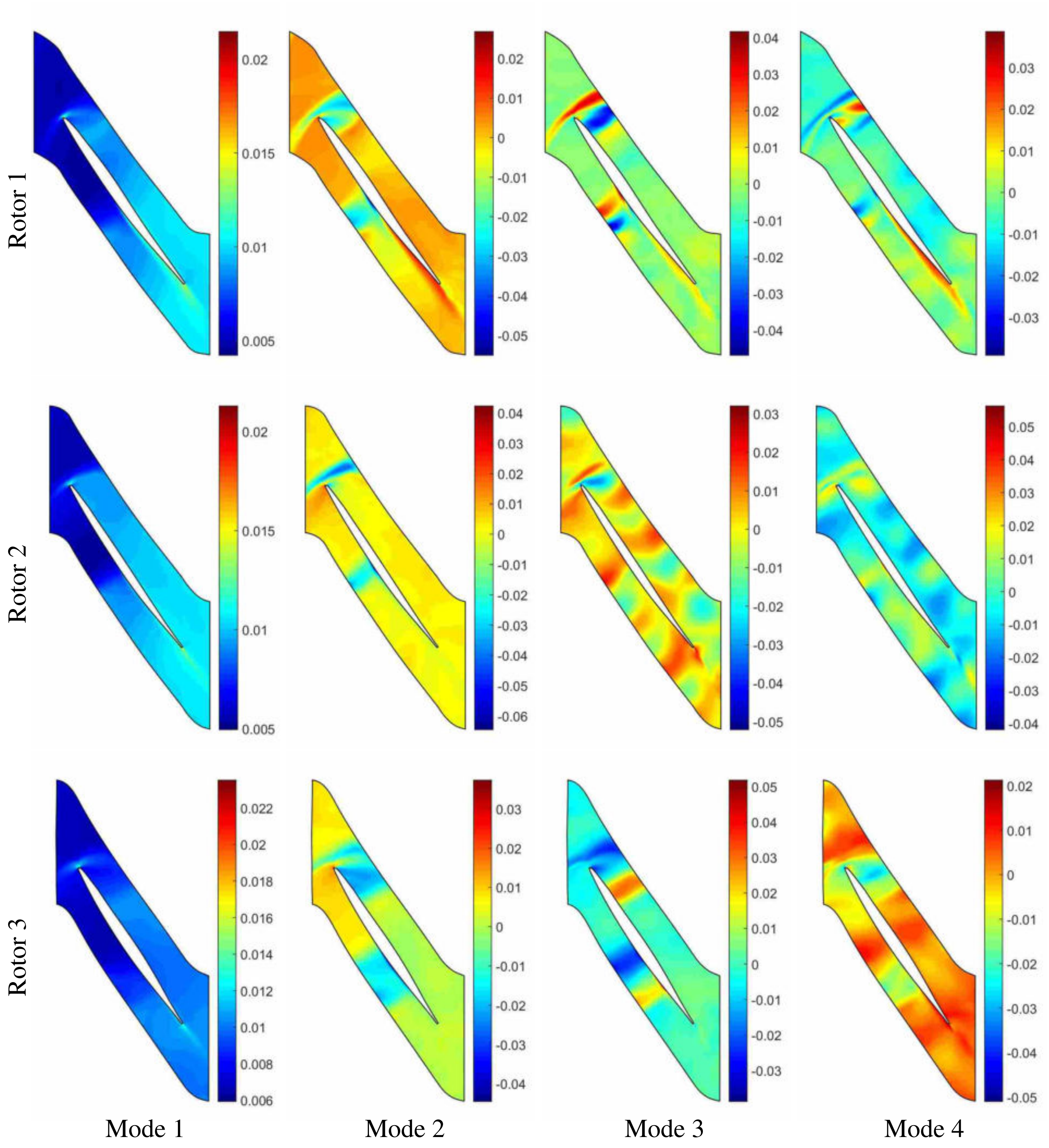

Figure A.3: Total pressure, design operating condition.

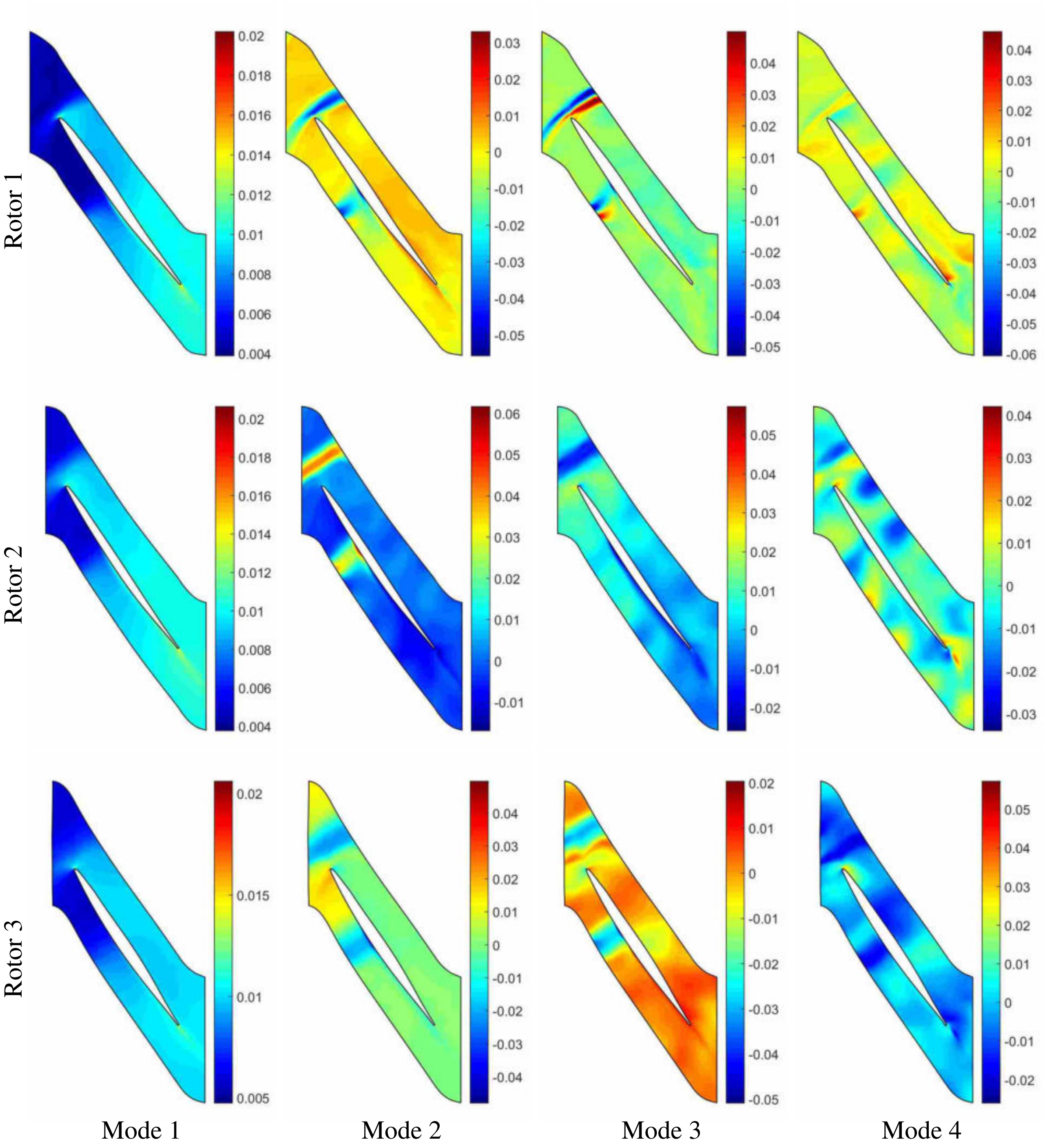

Figure A.4: Total pressure, near stall operating condition.

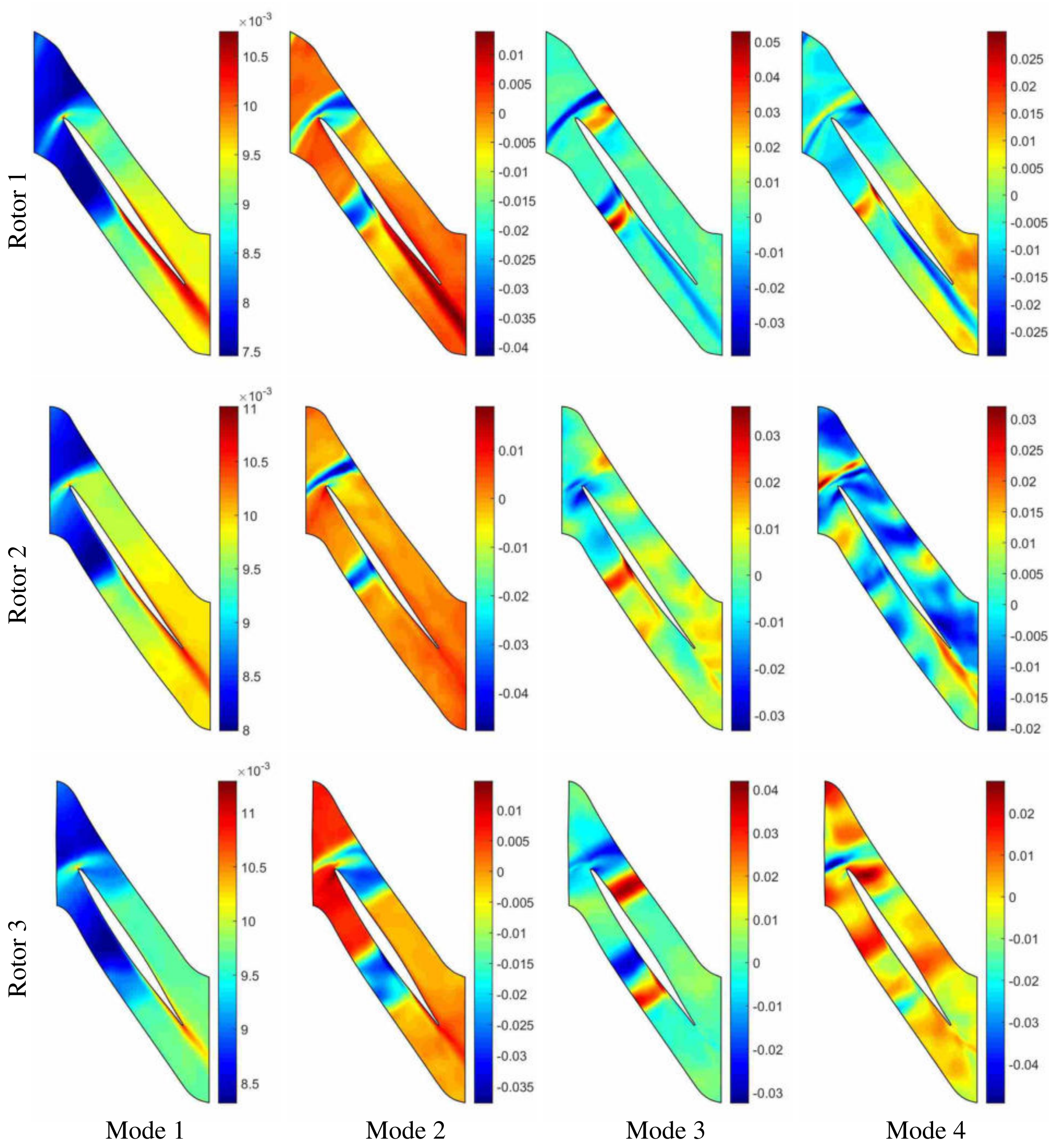

Figure A.5: Static temperature, design operating condition.

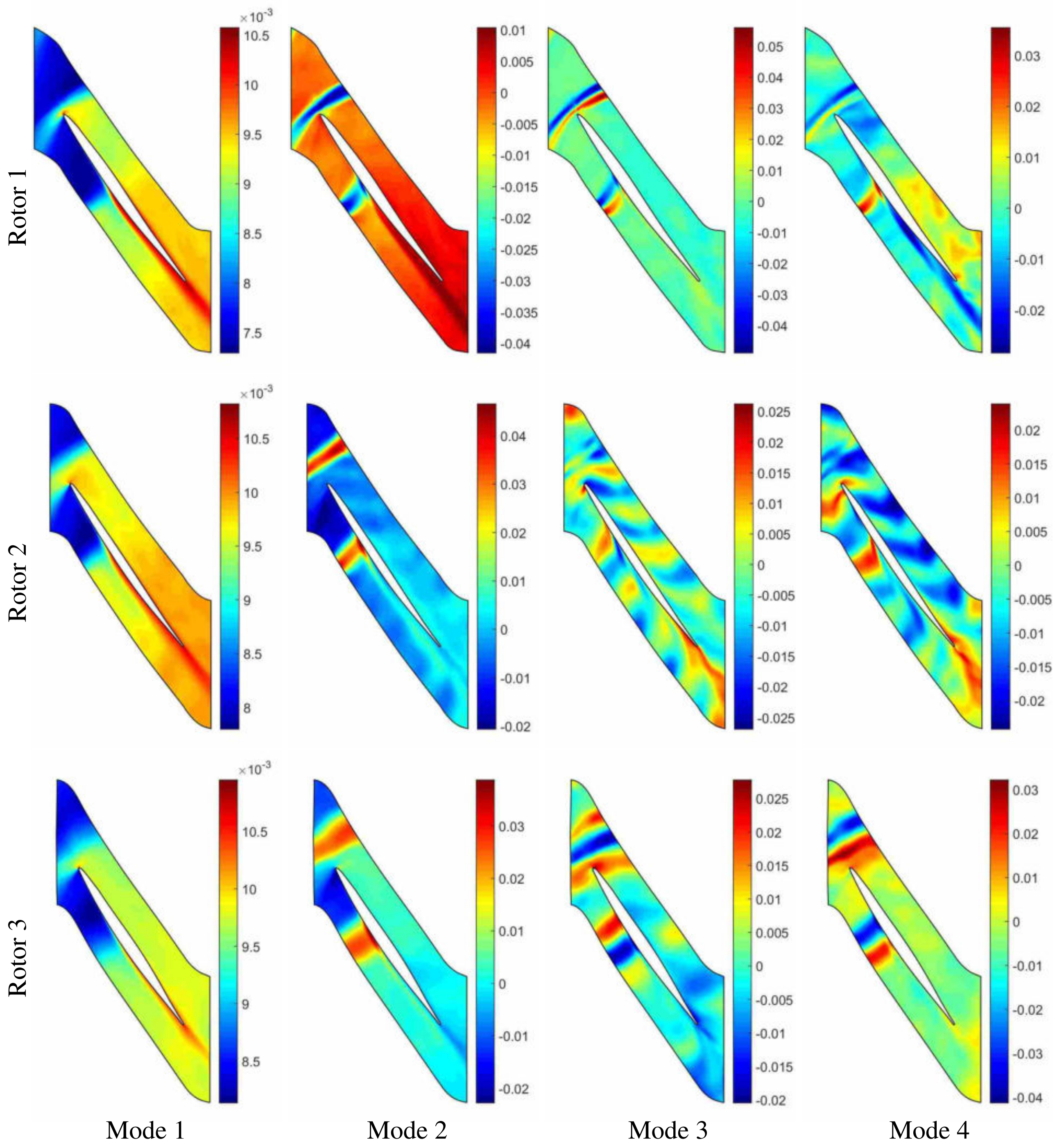

Figure A.6: Static temperature, near stall operating condition.

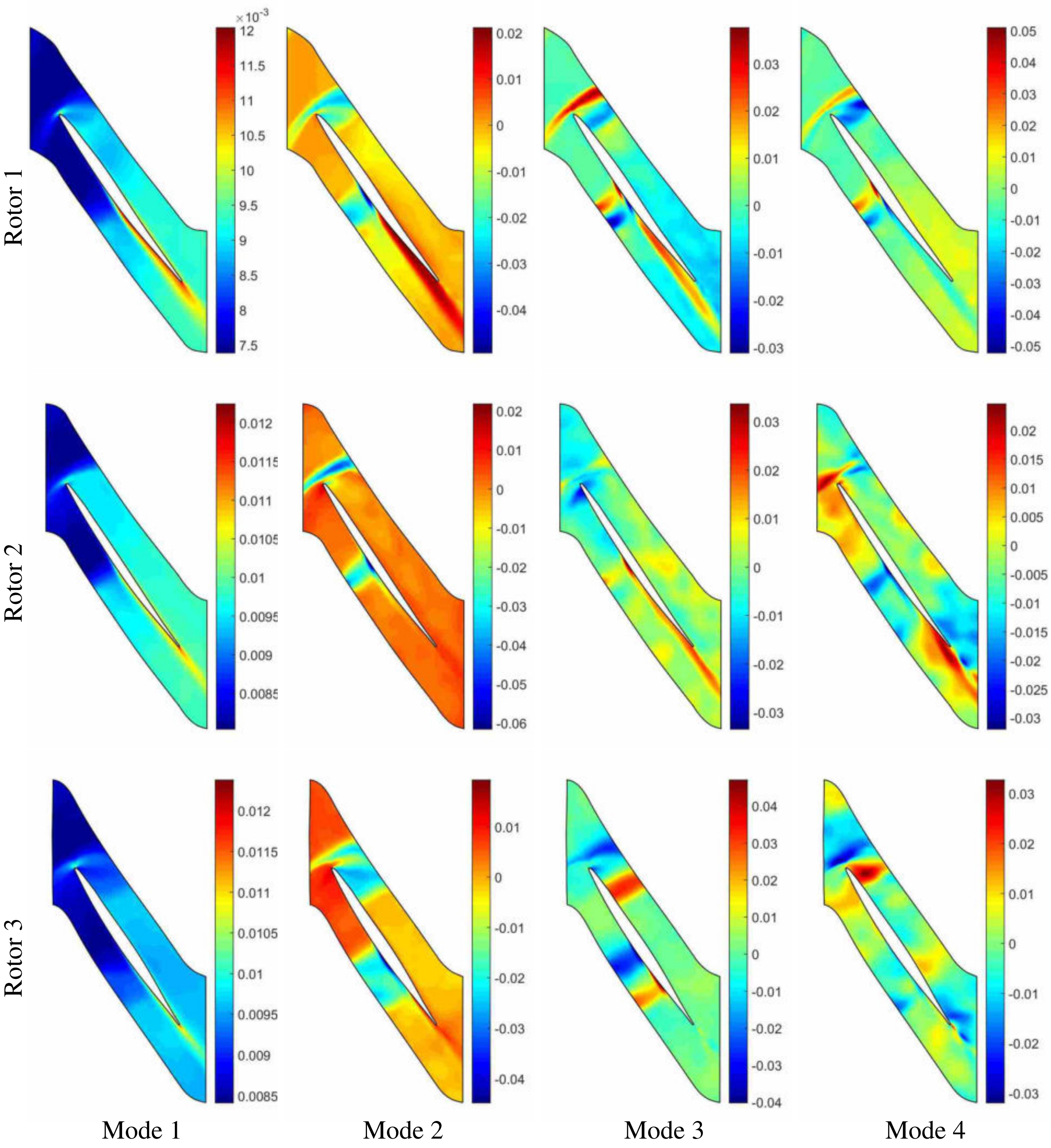

Figure A.7: Total temperature, design operating condition.

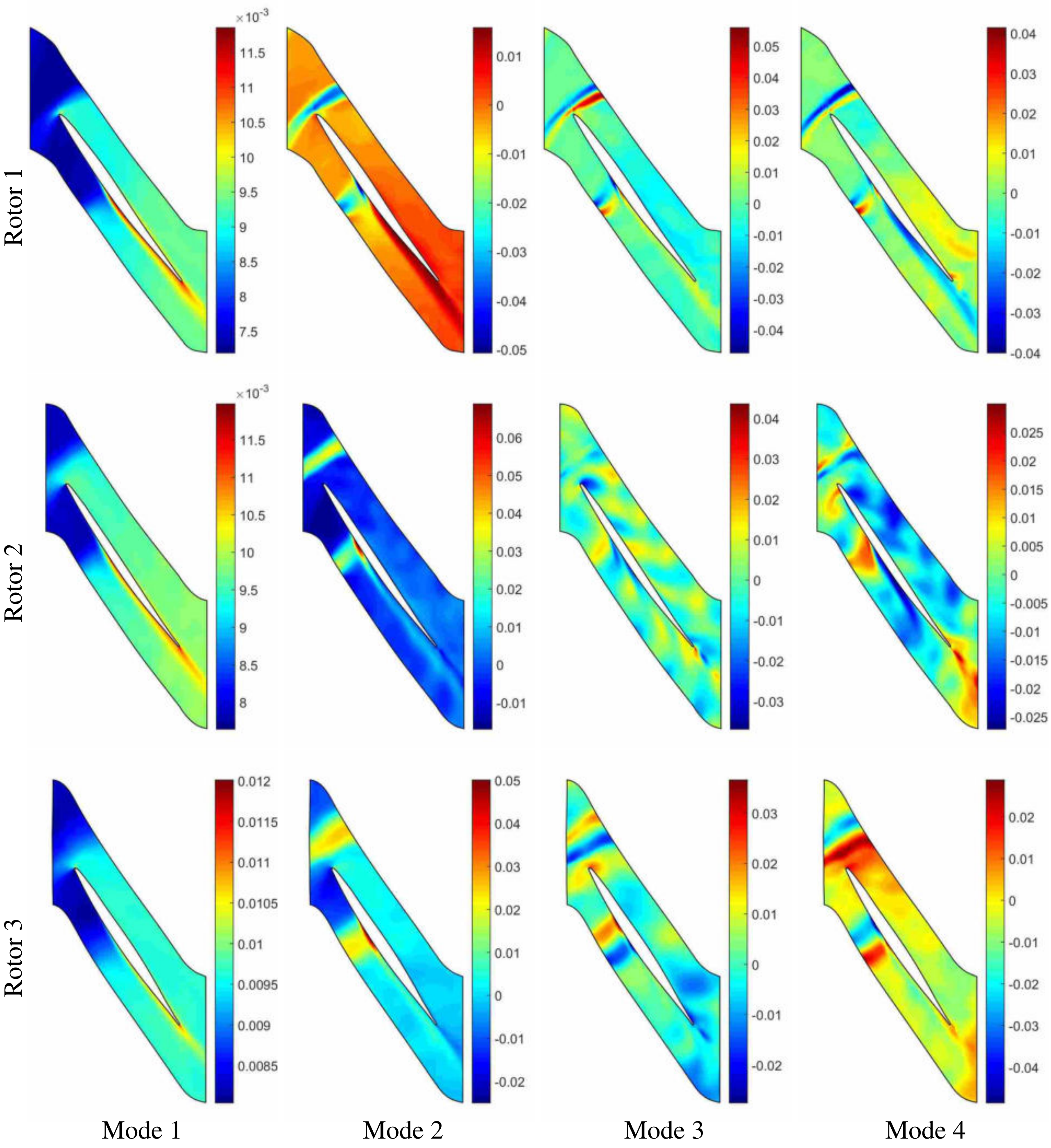

Figure A.8: Total temperature, near stall operating condition.

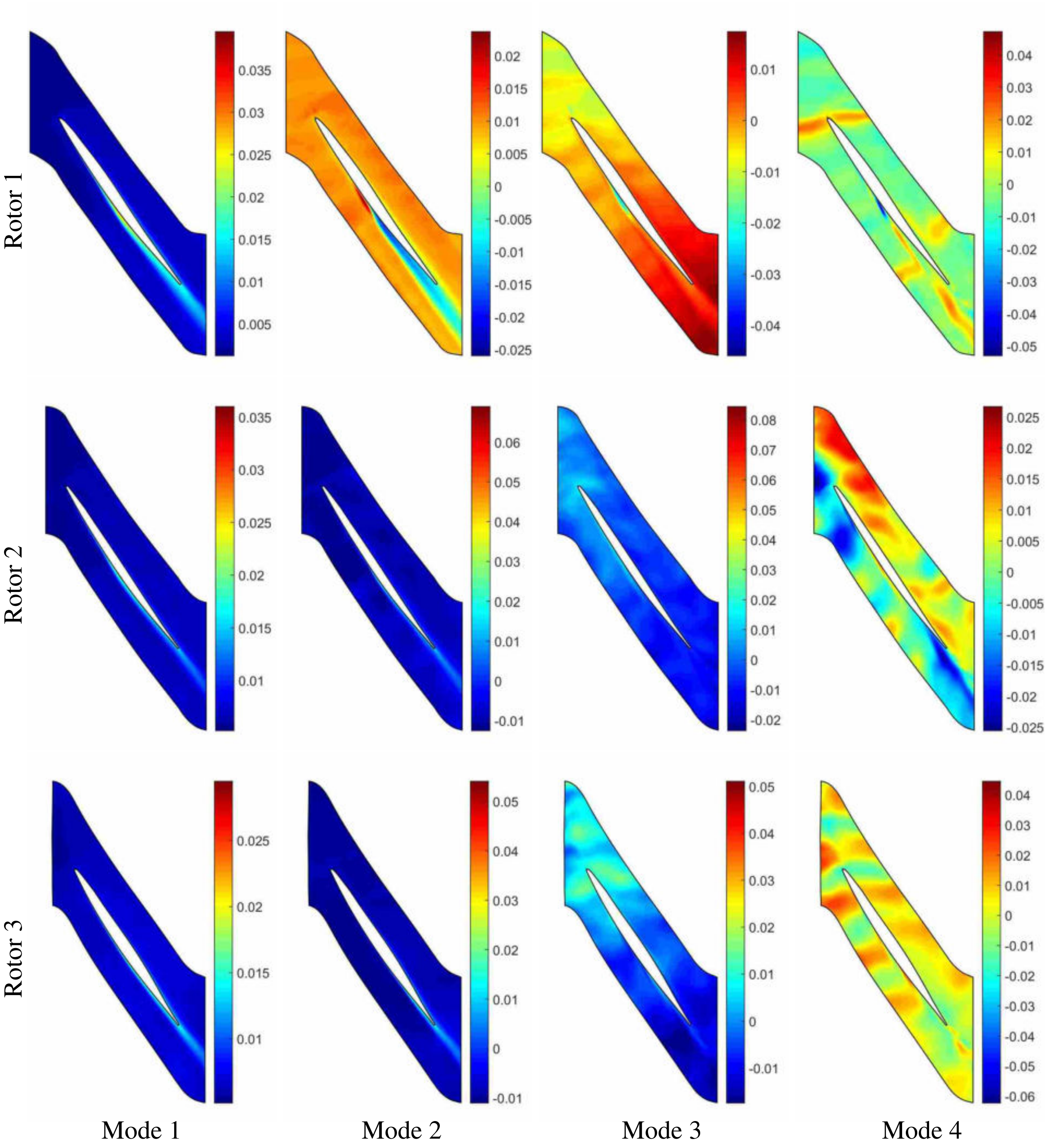

Figure A.9: Entropy, design operating condition.

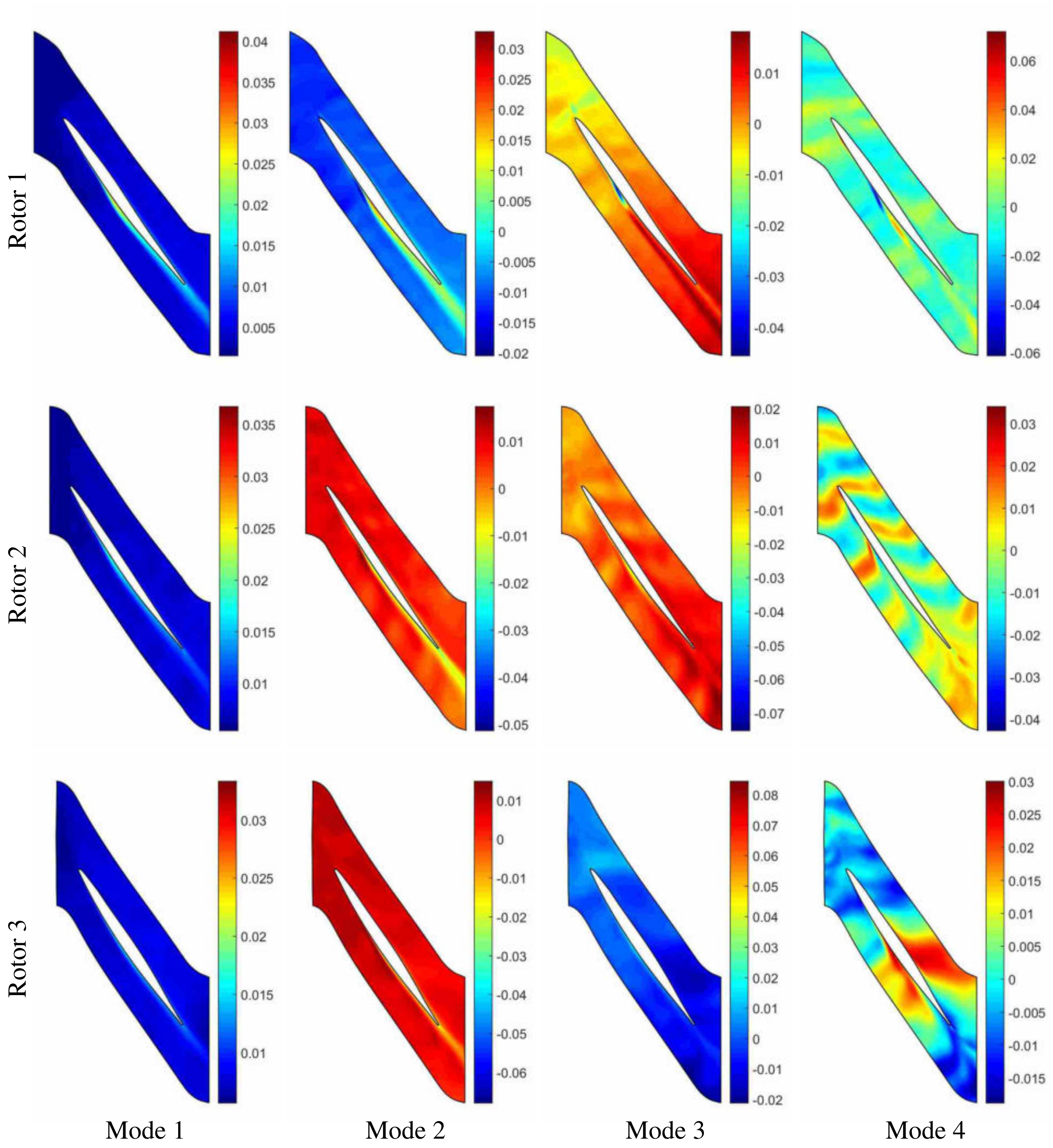

Figure A.10: Entropy, near stall operating condition.

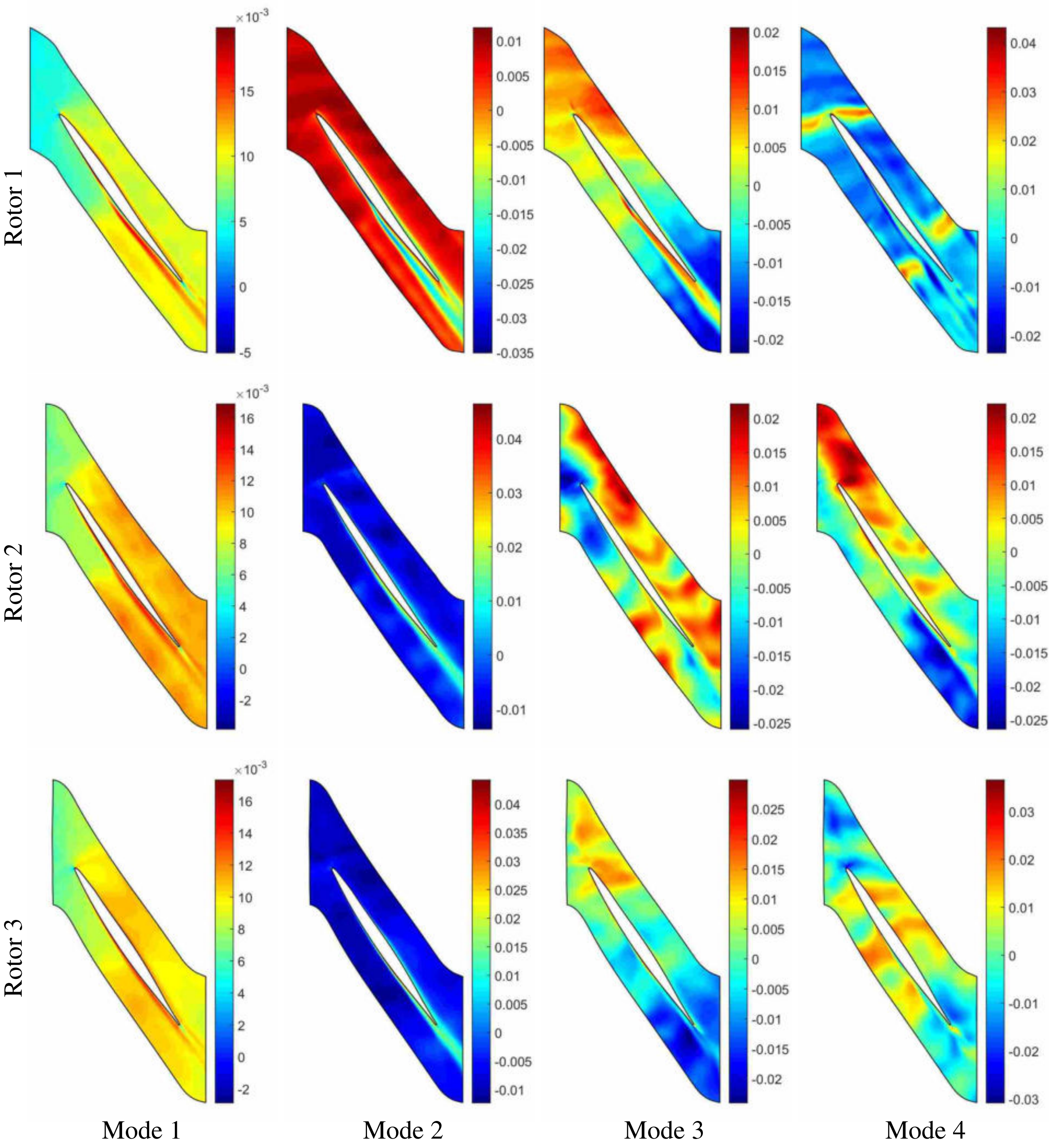

Figure A.11: Entropy flux, design operating condition.

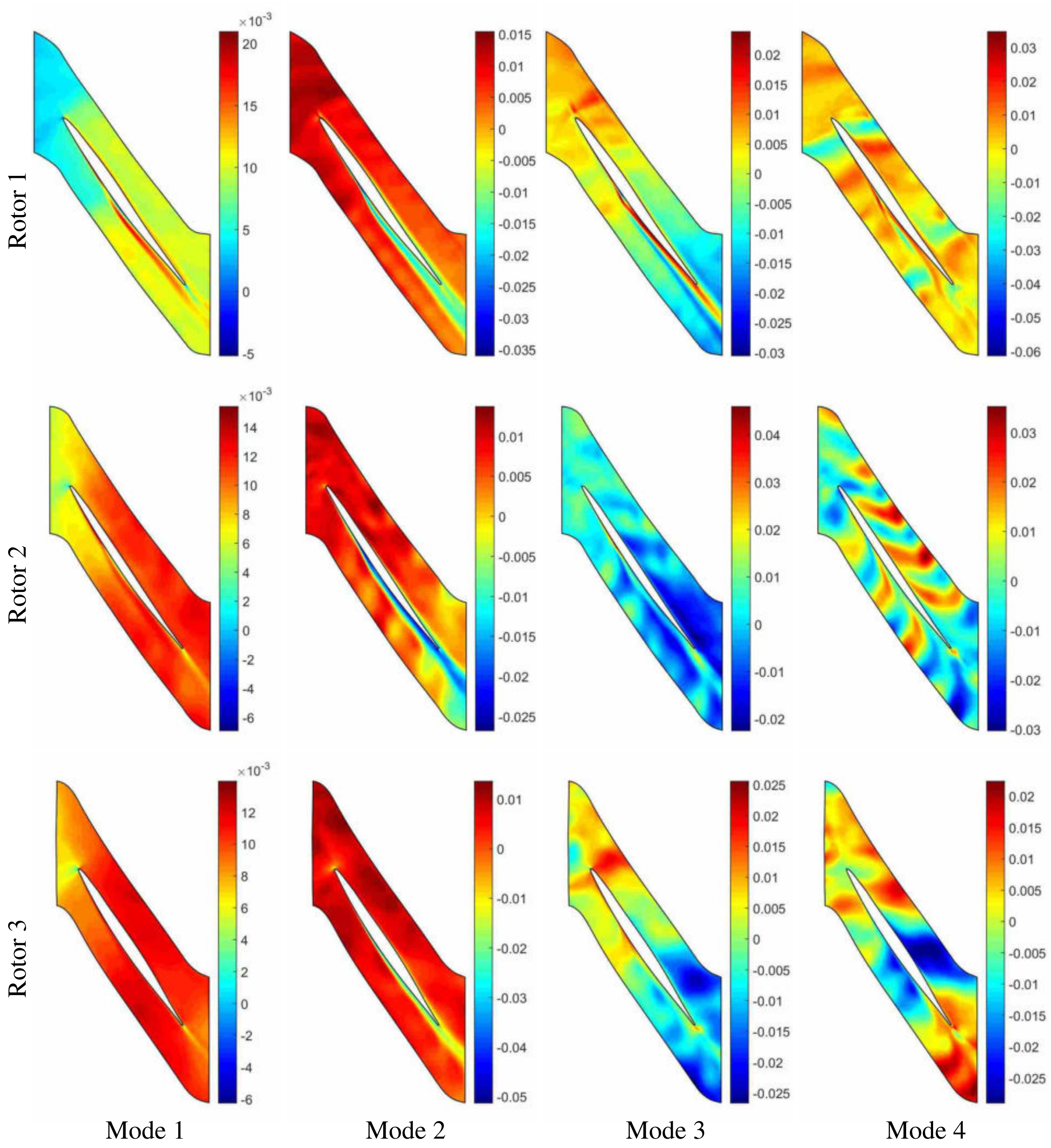

Figure A.12: Entropy flux, near stall operating condition.

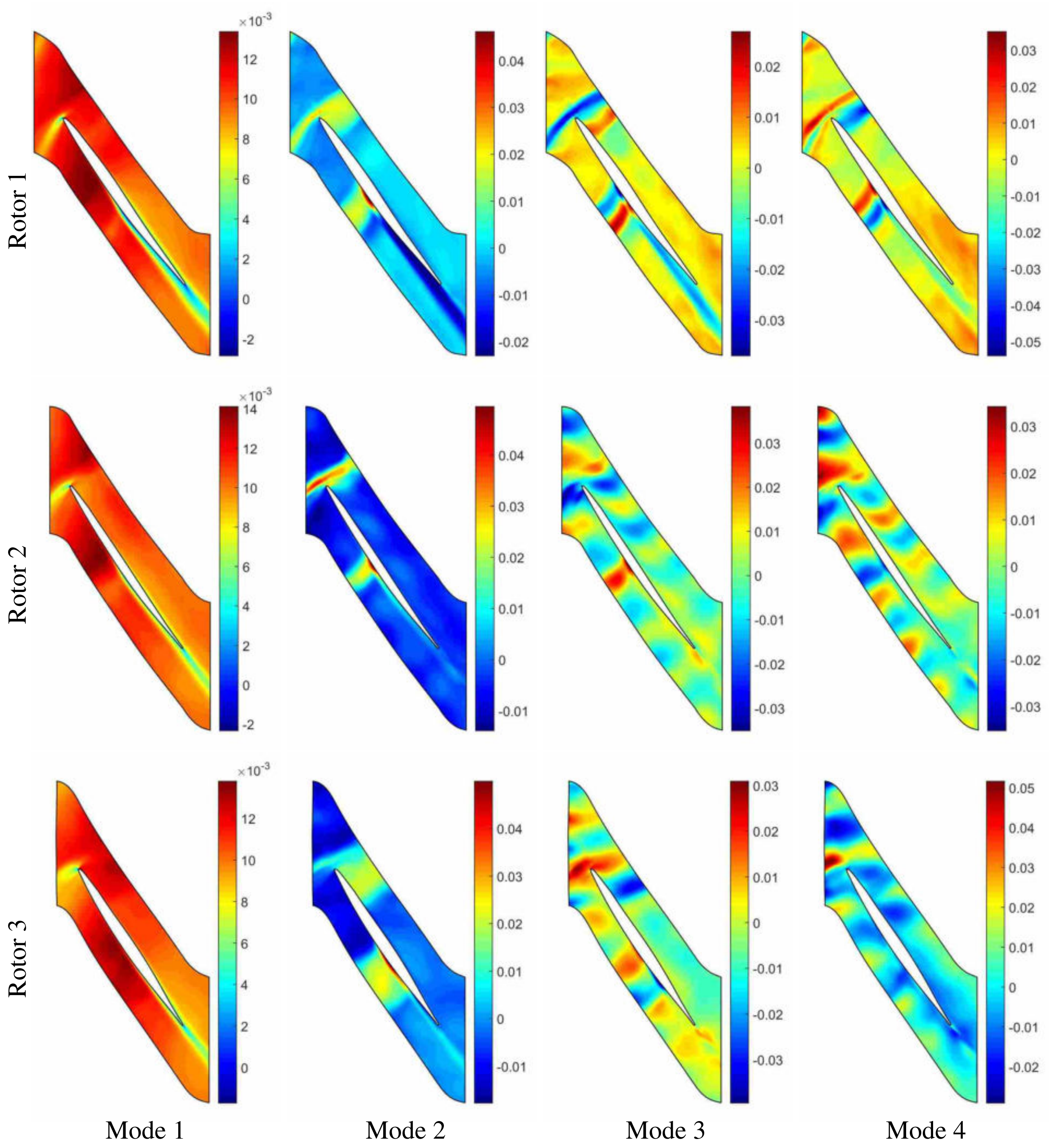

Figure A.13: Axial velocity, design operating condition.

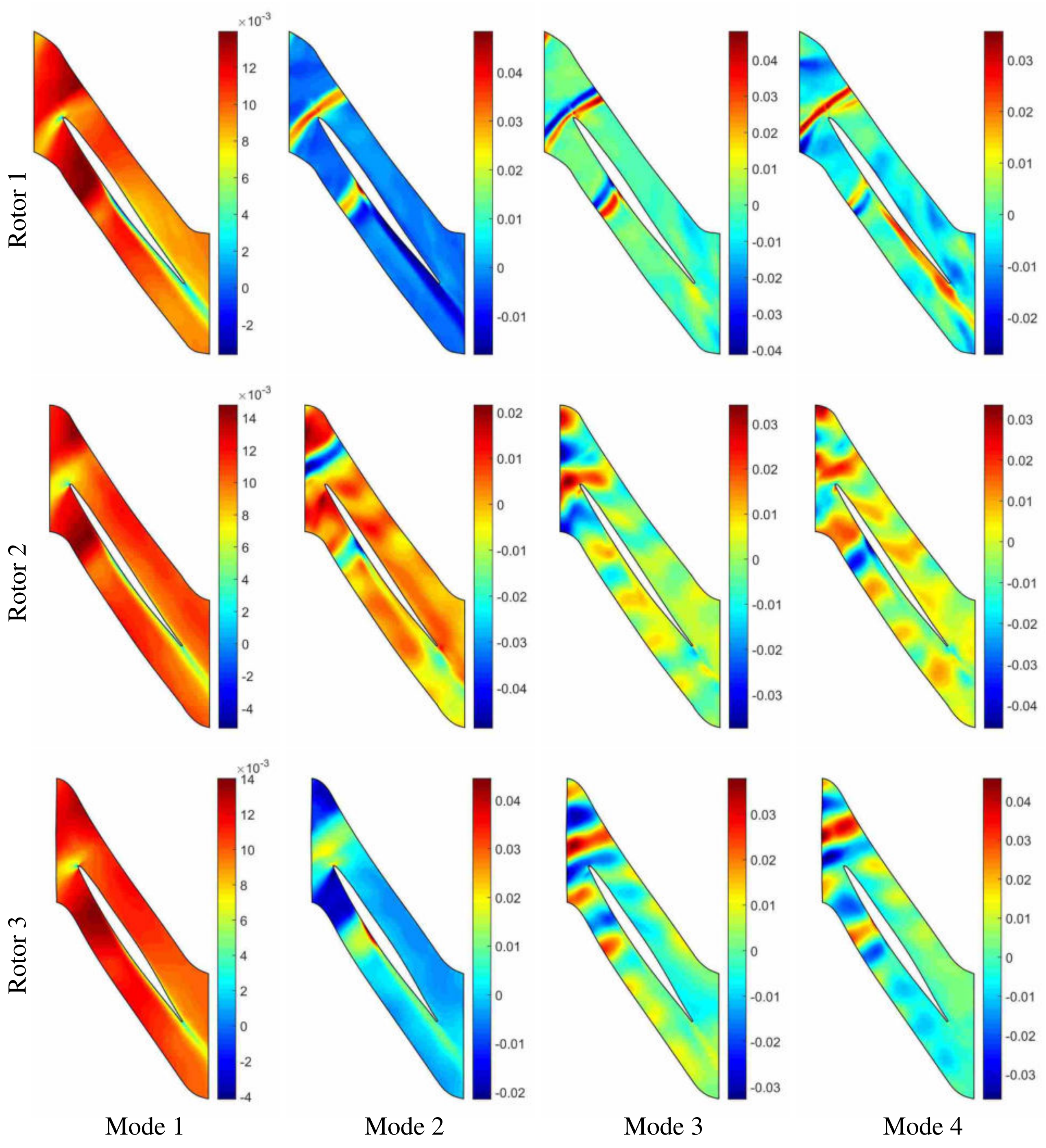

Figure A.14: Axial velocity, near stall operating condition.

APPENDIX B. CODE

This appendix contains two codes created and used in the analysis process. Much of the POD functionally was written by Blanc and is included in his thesis [4]. Several codes were written using his functions to calculate the POD and generate some of the plots. His codes were sometimes adapted. These codes are not included. The included codes are the implimentation of DMD and the FieldView data extraction code.

B.1 Implimentation of DMD

```
%this function implements the dynamic mode decomposition as outlined by
%Schmid 2010. The calculation of the matrix S and the DMD modes are based
%on the POD modes.

%Written:  March 2015 by Ron Spencer

%inputs:   D_s              data matrix which each column
%          delta_t          time step between each column

%outputs:  phi              scaled dynamic modes
%          phi1             unscaled dynamic modes
%          eigarray         eigenvalues
%          logeigarray      scaled eigenvalues
%          amplitude        dynamic mode amplitudes
%          coherance_norm   measure of coherence of each mode with POD modes

function [phi,phi1,eigarray,logeigarray,amplitude,coherance_norm]...
    = DMD(D_s,delta_t)
%define dimensions of the snapshot basis
```

```
m = size(D_s,1);
n = size(D_s,2);

%define threshold value for singular values to keep
soll = 1e-8;

%use the snapshot basis to form the D_{1}^{N-1} matrix
D1 = D_s(:,1:n-1);

%use the snapshot basis to form the D_{2}^{N} matrix
D2 = D_s(:,2:n);

%execute economy size SVD of D_{1}^{N-1}
[U,S,V] = svd(D1,0);
Sval = diag(S);

%compute the singular values above the threshold
r = 0;
for i=1:n-1
    if Sval(i) > soll
        r = r+1;
    end
end

Smax = max(Sval);
Smin = min(Sval);

%discarded percentage of total variance
discarded = 100-(norm(Sval(1:r))^2*100/norm(Sval)^2);

%extract portion of matrices corresponding to nondiscarded singular values
Up = U(:,1:r);
Sp = S(1:r,1:r);
Vp = V(:,1:r);
Vt = V';
Vtp = Vt(1:r,:);
```

```
%Compute the inverse of the singular values diagonal matrix S
Spinv = inv(Sp);

%Compute the matrix L1 = U^{H}*D_{2}^{N}
S1 = Up'*D2;

%Compute matrix L2 = V*S^{-1};
S2 = Vp*Spinv;

%compute matrix L = L1*L2;
S = S1*S2;

%Compute eigenvalues and eigenvectors of the L matrix
[eigVec, eigVal] = eig(S);
eigarray = diag(eigVal);
logeigarray = log(eigarray)/delta_t;

%unscaled dynamic modes
phi1 = Up*eigVec;

%Dynamic mode amplitudes
d = phi1\D1(:,1);
amplitude = abs(d);

%Scaled dynamic modes
phi = phi1*diag(d);

%coherance measure
coherance = U(:,2:4)'*phi1;
coherance_mag = abs(coherance);

coherance_norm = diag(sqrt(coherance_mag'*coherance_mag));
```

B.2 Data Extraction in FieldView Extension Language

```
file_path = "C:/Users/rspen_000/Documents/Ron/Distortion/distorted/...
```

```
near_stall/rotor_1/density/"             --string variable

--properties = "Stagnation press. [OVERFLOW]" --total
--properties = "Pressure [OVERFLOW]"          --static
--properties = "Stag. temperature [OVERFLOW]" --total
--properties = "Temperature [OVERFLOW]"         --static
--properties = "Entropy [OVERFLOW]"
--properties = "u-velocity [PLOT3D]"
--properties = "w-velocity [PLOT3D]"
properties = "Density (Q1)"
--properties = "Velocity Magnitude [PLOT3D]"
--properties = "x-momentum (Q2)"

for j=1, 28 do --loop over the blade rows
local comp_table = {
grid = j,
axis = "K",

I_axis = {
--min = 3,
--current = 1,
--max = 166,
},

K_axis = {
min = 1,
current = 70,
max = 135,
},
scalar_func = properties, --select scalar function for computation
```

```
}

local comp = create_comp(comp_table) --create computational surface
file_name = file_path.."blade"..j..".csv"
fv_script("EXPORT COMP "..file_name)
print("blade"..j)

end

print("done")
```